

(NASA-CR-165590) DEVELOPMENT OF ELECTRICAL
TEST PROCEDURES FOR QUALIFICATION OF
SPACECRAFT AGAINST EID. VOLUME 1: THE CAN
TEST AND OTHER RELEVANT DATA Progress
Report, Mar. - Sep. 1981 (IRT Contr., San

N83-12136

Unclas

G3/18 01171

1. Report No. NASA CR-165590		2. Government Accession No.		3. Recipient's Catalog No.	
4. Title and Subtitle Development of Electrical Test Procedures for Qualification of Spacecraft Against EID Volume I: The CAN Test and Other Relevant Data				5. Report Date April 1982	
				6. Performing Organization Code	
7. Author(s) J.M. Wilkenfeld, R.J.R. Judge and B.L. Harlacher				8. Performing Organization Report No. 8195-018	
9. Performing Organization Name and Address IRT Corporation P. O. Box 80817 San Diego, California 92138				10. Work Unit No.	
				11. Contract or Grant No. NAS 3-21967	
12. Sponsoring Agency Name and Address National Aeronautics and Space Administration Lewis Research Center 21000 Brookpark Road, Cleveland, Ohio 44135				13. Type of Report and Period Covered 3/81 - 9/81	
				14. Sponsoring Agency Code 5532	
15. Supplementary Notes Project Manager, John V. Staskus NASA - Lewis Research Center Cleveland, Ohio 44135					
16. Abstract This two-volume report describes a combined experimental and analytical program to develop system electrical test procedures for the qualification of spacecraft against damage produced by space-electron-induced discharges (EID) occurring on spacecraft dielectric outer surfaces to be incorporated into a proposed EID MIL-STD (or into a modified MIL-STD 1541). Volume I presents the data on the response of a simple satellite model, called CAN, to electron-induced discharges. The experimental results were compared to predicted behavior and to the response of the CAN to electrical injection techniques simulating blowoff and arc discharges. Also included is a review of significant results from other ground tests and the P78-2 program to form a data base from which is specified those test procedures which optimally simulate the response of spacecraft to EID. The electrical and electron spraying test data were evaluated to provide a first-cut determination of the best methods for performance of electrical excitation qualification tests from the point of view of simulation fidelity. Volume II presents a review and critical evaluation of possible approaches to qualify spacecraft against space electron-induced discharges (EID). A variety of possible schemes to simulate EID electromagnetic effects produced in spacecraft have been studied, and candidate electrical injection techniques for electrically exciting spacecraft have been developed. These techniques form the principal element of a provisional, recommended set of test procedures for the EID qualification spacecraft. The report also identifies significant gaps in our knowledge about EID which impact the final specification of an electrical test to qualify spacecraft against EID.					
17. Key Words (Suggested by Author(s)) Spacecraft Charging, SCATHA, Electron-Induced Discharges, Electrical Testing, Qualification Testing, Spacecraft				18. Distribution Statement Publicly Available	
19. Security Classif. (of this report) UNCLASSIFIED		20. Security Classif. (of this page) UNCLASSIFIED		21. No. of Pages	
				22. Price*	

For sale by the National Technical Information Service Springfield Virginia 22161

TABLE OF CONTENTS

ACKNOWLEDGEMENTS	xii
1. OVERVIEW	1
1.1 Introduction	1
1.2 Test Objective and Approach	3
1.3 Summary	5
2. BACKGROUND	11
2.1 Geospace Environments	11
2.2 Prior Knowledge	16
2.2.1 Theoretical Investigations	16
2.2.2 Spacecraft Observations	17
2.2.3 Ground Test Measurements	21
3. EXPERIMENTAL	23
3.1 Test Object	23
3.2 CAN Mounting and External Measurements	29
3.3 Environmental Simulation	33
3.4 Tank Operation	42
4. PRESENTATION OF DATA	45
4.1 Introduction	45
4.2 Kapton	47
4.3 Teflon	57
4.4 Solar Array Mockup	70
4.5 Electrical Test Data	87
4.5.1 Introduction	87
4.5.2 Arc Discharge Experiment	88
4.5.3 CDI Tests	91
5. DATA EVALUATION	97
5.1 Introduction	97
5.2 Discharge Coupling	98
5.3 Data Comparison	101
5.3.1 Kapton	101
5.3.2 Teflon	105
5.3.3 Solar Array Mockup	109
5.4 Comparison of Electrical Excitation with EID	111

PRECEDING PAGE BLANK NOT FILMED

6.	DEVELOPMENT OF AN ELECTRICAL TEST PROCEDURE	117
6.1	Implications of the CAN Tests for the Present MIL-STD 1541 Test Procedure	117
6.2	Environment Effects	120
6.3	Scaling	129
	REFERENCES	135
	DISTRIBUTION LIST	141

LIST OF FIGURES

Figure

1	The solar spectrum	12
2	Magnetosphere (after DeForest)	13
3	ATS 5 particle spectrograms (parallel detectors), keograms, ATS 5 energy fluxes and average energies, precipitated energy fluxes and average energies, and AE indices for day 032, 1970	14
4	Histograms of the occurrence frequencies of the electron and ion temperatures and current at geosynchronous orbit as measured by ATS-5 and ATS-6	15
5	Spectrogram of Day 59, 1976, from ATS-6	18
6	Local time dependence of circuit upsets for several DoD and commercial satellites	20
7	Daily average discharge rate as a function of daily average a_p	20
8	Kapton sample	24
9	Teflon sample	24
10	Solar array mockup	24
11	Simulated solar panel (front)	25
12	Simulated solar panel (rear)	26
13	External sensor location on the CAN	27
14	IRT analog fiber optic data system	28
15	Resistor patch panel	30
16	CAN and source locations in Tank 5	31
17	CAN and source locations in Tank 5	32
18	Top view of CAN	33
19	Front of test object showing probe arm	34
20	Internal electronics	35
21	Solar UV spectrum	38
22	Differential flux of photoelectrons from aluminum due to solar irradiation	39

Figure

23	Photoelectric efficiency of aluminum	40
24	Measured angular variation of VUV source	41
25	Variation of electron beam current density with pressure	42
26.	Path of TREK probes across the CAN front face	48
27	Discharges in Kapton sample	48
28	Surface potential map of Kapton, grounded configuration, $E_i = 10 \text{ keV}$, $J_i = 2 \text{ na/cm}^2$	49
29	Surface potential map of Kapton, grounded configuration, $E_i = 15 \text{ keV}$, $J_i = 2 \text{ na/cm}^2$	49
30	Kapton, low impedance configuration, B sensor data	52
31	Kapton, grounded configuration, photographs of sensor data	53
32	Digitized blowoff current response for Kapton, grounded configuration	54
33	Digitized B sensor response for Kapton, grounded configuration	55
34	Kapton sensor response	56
35	Sensor data, Kapton, high impedance configuration	56
36	Discharges in the Teflon tape sample	58
37	Surface potential map of FEP Teflon, grounded configuration, $E_i = 10 \text{ keV}$, $J_i = 2 \text{ na/cm}^2$	59
38	Surface potential map of FEP Teflon, grounded configuration, $E_i = 15 \text{ keV}$, $J_i = 2 \text{ na/cm}^2$	59
39	Surface potential scan, FEP Teflon, $E_i = 20 \text{ keV}$, $J_i = 2.5 \text{ na/cm}^2$	60
40	Surface potential scan, FEP Teflon, high impedance configuration, $E_i = 20 \text{ keV}$, $J_i = 2.5 \text{ na/cm}^2$	60
41	Surface potential map of Teflon, $E_i = 20 \text{ keV}$, before discharge	61
42	Surface potential map of Teflon, $E_i = 20 \text{ keV}$, after discharge	61

Figure

43	FEP Teflon, sensor output, grounded configuration	63
44	FEP Teflon, sensor data, grounded configuration	64
45	FEP Teflon response, grounded configuration	65
46	Typical digitized blowoff and return currents, FEP Teflon, grounded configuration	66
47	Digitized response of \dot{B} Sensor 4	67
48	Digitized response of \dot{B} Sensor 11	68
49	Estimated peak surface currents, Teflon	69
50	Peak \dot{B} sensor responses, Teflon	69
51	Sensor photos, Teflon, high impedance configuration	71
52	Sensor responses, FEP Teflon, high impedance configuration	73
53	Discharges in the solar array mockup	74
54	Surface potential scan of the solar array mockup, grounded configuration	75
55	Surface potential scan of the solar array mockup, grounded configuration	75
56	Photographs of sensor of solar array mockup, grounded configuration	77
57	Digitized return and blowoff currents, grounded solar array mockup	79
58	Digitized response of \dot{B} Sensor 8, solar array mockup, grounded configuration	80
59	Normalized peak \dot{B} sensor response solar array mockup, grounded configuration	81
60	Photographs of sensor responses solar array, high impedance configuration	82
61	Digitized return and blowoff currents, solar array mockup, high impedance configuration	84
62	Digitized \dot{B} sensor data, solar array mockup, high impedance configuration	85

Figure

63	Peak \dot{B} sensor and backplane wire currents for the solar array mockup, high-impedance configuration	86
64	Relative timing of blowoff and return current signals for solar array mockup	87
65	Arc discharge test configuration	89
66	Arc discharge current waveform, hardwired configuration	90
67	Response measured by CML3 sensor at position 1	90
68	Representative \dot{B} data set for CDI excitation of the CAN	92
69	Solid cylinder - current drive H-fields for 0.3 m plate height	94
70	Surface potential scan of Kapton, grounded configuration, $E_i = 20$ keV showing an edge discharge along the seam joining the two pieces of tape	102
71	MIL-STD 1541 arc injection	118
72	Arc current	118
73	Discharge peak current versus area for Kapton	131
74	Peak discharge current versus area for fused quartz	132

LIST OF TABLES

Table

1	Mean Values of Electron and Ion Current Densities and Characteristic Energies Inferred Using a Double Maxwellian Velocity Distribution	16
2	CAN Response Measurements	36
3	Photoelectric Current Densities for Irradiation by the Krypton Resonance Lines	40
4	Charging Behavior of Dielectric Samples	50
5	Data Set for Arc Discharge	91
6	Data Set for CDI and Blowoff	95
7	Summary of Kapton Surface Current Data	103
8	Summary of Teflon Response Data	106
9	Solar Array Mockup Response Data	110
10	Normalized B Data	113
11	Normalized Experimental H Data	113
12	Components of Space Radiation Environment	122
13	Estimated Discharge Voltages and Discharge Times	124
14	Conductivity of Representative Spacecraft Insulators	126
15	Second Surface Mirror Discharge Characteristics for Simultaneous Low and High Energy Electron Exposures	127

ACKNOWLEDGEMENTS

The authors wish to thank the following individuals and organizations for their assistance.

NASA LeRC. John V. Staskus, the NASA Program Manager, N. John Stevens and N. Grier for program support; R. Vetrone, E. Theman, D. Thoennes, R. Sprankle, D. Hoffman, E. Smith, C. Ollick, J. Malinkey, and R. Nagy for their assistance in designing, constructing and performing the tests.

USAF Space Division. MJR G. Kuck, Lt. R. Weidenheimer and Lt. W. Ameling for providing project funding and program support.

Aerospace Corporation. L. Weeks for program support and R. Broussard for his critical comments.

AFWL. CPT G. Kuller and Dr. C. Aeby for the loan of data links.

DNA. CPT T. Chapman and MJR R. Gullickson for the loan of data links and sensors.

SAI. Dr. E. O'Donnell and Dr. A. Holman for valuable comments about the experiments.

IRT Corporation. J. Gallacher, A. deKerguelen, A. Weiman and L. Longden for experimental support; A. Smith and G. Hall for their help in producing the final report.

PRECEDING PAGE BLANK NOT FILMED

1. OVERVIEW

1.1 INTRODUCTION

This document describes the testing and data analysis for the exposure of a right-circular cylinder (called the "CAN") covered with dielectrics on one end to a simulation of the charged particle environment responsible for charging of spacecraft dielectrics in geosynchronous orbit. The tests were performed in Tank 5 of the Electropulsion Laboratory at the NASA-Lewis Research Center (LeRC) during March 1980. The electrical response of the CAN produced by discharges in a series of dielectrics used on the P78-2 (SC ATHA) spacecraft was studied.

This test report represents one of the two major deliverables for the present program, entitled "SCATHA Model Tests" (Contract NAS3-21967) jointly sponsored by NASA-LeRC and the USAF-Space Division (SD). This work is a continuation of a program begun under joint SD and Defense Nuclear Agency (DNA) sponsorship entitled "Electrostatic Discharge Modeling, Testing, and Analysis for SCATHA," under Contract DNA001-77-C-0180.

The major objective of this combined experimental and analytical program has been the development of validated system electrical test procedures for the qualification of spacecraft against damage produced by space-electron-produced discharges occurring on outer dielectric surfaces (EID) to be incorporated into the proposed EID Mil-Standard (or into a modified Mil-Standard 1541).

This work performed in this program is described in two reports.

1. This report presents the data on the response of the CAN to electron-induced discharges. The experimental results are compared to predicted behavior and to the response of the CAN to electrical injection techniques simulating blowoff and arc discharges. Also reviewed and included are significant results from other ground tests and the P78-2 program to form part of the data base for specifying those test procedures which optimally simulate the response of spacecraft to EID. The electrical and electron spraying test data

have been evaluated to provide a first-cut determination of the best methods for performance of electrical excitation qualification tests from the point of view of simulation fidelity.

2. A second report whose major content is the specification of an experimentally validated set of test procedures to qualify spacecraft for reliable performance when subjected to a charged particle environment conducive to producing discharges. These specifications are in a form appropriate to the proposed EID appendix to MIL-STD 1541 (USAF), Electromagnetic Compatibility Requirements for Space Systems. This report includes a description of the tradeoff analyses by which they were selected, the recommended sources, measurement techniques, sensors, data to be recorded and data analyses to be employed.

The first part of this program, described in References 1 and 2, combined both electrical testing of the two test objects, the CAN and a two-thirds scale model of the P78-2 spacecraft called the SCATSAT, as well as an adaptation and application of the SABER and ABORC SGEMP codes to perform EID coupling analysis. The electrical testing performed was designed to simulate two aspects of space-electron-induced discharges. The first is the punchthrough of charge in which the discharge current travels through the bulk dielectric to the substrate. The second is the outward emission or blowoff of charge which occurs in EID, at least in its ground simulations. A third type of discharge, flashover, also occurs. Here the discharge current travels along the surface of the dielectric to a grounded edge. While these three types of discharge have been distinguished in the literature, experimental evidence implies that they are really complementary aspects of the same general phenomenon. All three types may occur in a single discharge.

Three electrical simulations of the canonical discharge mechanisms were employed to study the structural response of both the CAN and the SCATSAT, and internal wire coupling in the SCATSAT. The CAN is a geometrically simple body whose behavior is easy to analyze. The SCATSAT was designed to simulate features of the P78-2 important to its electromagnetic response. In our first round of testing, the punchthrough mechanism was simulated by discharging a large capacitor mounted on the top surface of the CAN through a spark gap. The blowoff mechanism was simulated by capacitive direct injection (CDI) in which current is driven down a wire connecting a drive plate and the object under test and allowed to return via the capacitive coupling

between plate and object. These experimental data were compared to numerical studies in which punchthrough and its simulation, blowoff, and the capacitive direct drive (CDI) simulations of blowoff were modeled and incorporated as source terms into the SABER and ABORC codes and body currents computed. The criteria for comparing responses was chosen to be the surface currents which circulate around the outer surface of the CAN consequent to a discharge.

The results of this test and analysis program demonstrated that if the different discharge drivers were properly normalized (same pulse shape), blowoff and its simulation produce much larger body currents per ampere of drive current than does punchthrough or arc discharge. Thus, to the extent that a significant fraction of the charge involved in an EID is blown off the spacecraft, this mechanism produces the worst-case response as measured by the above criteria. This conclusion has been substantiated by the electron spray tests described in this report.

A parallel series of tests was performed on the SCATSAT in which two electrical simulations of discharge mechanisms, CDI or blowoff and a MIL-STD 1541 arc for punchthrough/flashover, were the exciting sources. Responses were measured on internal wiring which simulates those monitored in the P78-2 engineering experiments, SCI-8B and the TPM, as well as two critical circuit lines. Again, the principal conclusion derived from these tests is that in most instances, CDI produces a larger response per ampere of drive current than the MIL-STD 1541 arc for discharge pulses of similar shape and width measured in terms of internal wire currents. The exception to the general pattern was for coupling to the solar array wiring. In this case arc discharge produced the larger response. Since solar arrays represent the major dielectric surface on a spacecraft where discharges can occur, these observations need to be pursued.

The results of the first round of testing and analysis substantiated by the electron spraying tests imply that the commonly employed technique using a MIL-STD 1541 type arc discharge to simulate surface EID does not reproduce its worst aspects, namely to produce the correct magnitude of body currents generated by blowoff. Blowoff is better simulated by CDI.

1.2 TEST OBJECTIVE AND APPROACH

The test described was performed for two principal reasons. First, to provide charging and discharge data on a relatively simple object which can be compared to the parallel electrical test results. Second, to try out some of the test, measurement,

analysis, and material simulation techniques which were to be utilized in the following, more complicated SCATSAT experiments. There were several secondary objectives to be achieved. These include: providing additional data for discharge characterization; verification of the predictive accuracy of NASCAP and SGEMP codes in analyzing charging and EID coupling, respectively; and providing data on the charging and discharge behavior of the insulating materials contained on the surfaces of the P78-2.

The approach being taken to develop validated electrical test techniques is to reproduce the important features of the electromagnetic responses evoked by EID in spacecraft. Even if it were technically and economically feasible to provide a reproduction of the space environment, full system satellite testing in such an environment would be difficult to perform and costly in terms of money and time. It is much more reasonable to provide electrical test techniques to simulate EID which can be included with other electrical testing for EMC and EMI routinely performed by manufacturers for satellite qualification.

The problem to be solved is twofold. The first part is to relate discharge characteristics, such as amplitude, pulsewidth, mode of propagation to the charging environment, material properties, and geometric configuration of the components in which the discharge occurs. Experimental programs addressing this question are being pursued elsewhere. While not a primary objective, additional data on discharge characterization was obtained during these experiments.

The second aspect of the problem is to relate these discharge characteristics to the electrical response of coupling produced in the spacecraft. This response depends on specific characteristics of a given satellite, including structure, location and types of insulating and conducting surfaces, types of penetrations, location, type and shielding of cables, the nature of the shielding offered by the structure and electronic boxes, and the characteristics of interface circuits. Since there are many system parameters which affect coupling, it was felt that the problem must first be studied with relatively simple systems so that the effect of each one of these factors can be isolated.

In these experiments, one component of the total system response was focused upon: the surface currents and fields generated as a consequence of the surface discharges which are known to occur in the natural substorm environment. Such currents and fields represent the source of electromagnetic energy which couple into interior spacecraft cabling and electronics through aperture penetration and diffusion. The quantitative EID response data were then compared to Phase I electrical test data to determine which electrical test techniques best simulate the observed responses.

The data generated in these experiments have provided baseline information on effects to be simulated by the electrical test techniques to be given to manufacturers, to qualify spacecraft against EID. In developing such techniques one attempts to provide one, or at most a few, electrical injection schemes which will simulate the most severe effects produced by EID. It is apparent that no single drive scheme is applicable in all cases. For example, if one is interested in internal discharging effects which may be produced by high-energy electrons penetrating cable or printed circuit dielectrics, then an approach different from that described here would have to be taken, using, for example a direct cable injection scheme similar to that developed for SGEMP testing.

It is likely that the planned program of ground testing, modeling, correlation with P78-2 data will not be completed before the issuance of the MIL-STD-1541 revision. Therefore, it was felt by all concerned with the generation of the EID MIL-STD, that it was important to summarize and evaluate the existing data base relevant to developing a valid simulation of the electrical effects of EID on spacecraft. Therefore, the scope of this volume was expanded to include a review of relevant EID ground testing and analyses. A review of relevant electrical test procedures developed to simulate related radiation-induced electromagnetic effects in spacecraft such as SGEMP will be presented in the second volume of this study.

A limited amount of ground test data and flight experience indicates that the more energetic components of the trapped electron population may penetrate the spacecraft skin and cause discharges in internal dielectrics such as cables and printed circuit boards. This phenomenon, called the electron caused electromagnetic pulse (ECEMP) effect, has not been addressed in the SCATHA program.

1.3 SUMMARY

The primary objective of the study was to provide an experimental data base characterizing the response of a simple, highly symmetric object to EID. These data are to be used to develop validated system electrical test procedures for the qualification of spacecraft against the potentially harmful coupling of discharge-created electromagnetic energy into electronics. Secondary objectives were to provide data for discharge characterization, coupling model validation and NASCAP tank model validation.

The scope of the study, included:

1. Electron spray testing of the CAN test object covered with a set of dielectric samples made from materials employed in the P78-2.

2. A comparative analysis of the electron spraying data, earlier electrical testing of the same object excited by two discharge simulation schemes and computer modeling of the discharge coupling process.
3. A critical review of the existing relevant literature related to EID coupling.
4. A discussion of the implications of the existing data base for development of validated EID electrical qualification techniques.

The electron spraying testing was performed with the CAN covered with:

1. 1 mil Kapton tape, 1.5 mil acrylic adhesive, 75 cm diameter circle.
2. 5 mil Teflon OSR, silver backed, 75 cm diameter circle.
3. A mock solar array panel with 6 mil fused quartz coverslips and simulated solar array circuit wiring; 50 cm x 50 cm.

The exciting sources were monoenergetic beams of electrons, $10 < E < 20$ keV, $1 \text{ na/cm}^2 < J < 5 \text{ na/cm}^2$. Measurements included surface potential scans before and after discharges, the return current flowing through a ground strap connecting the CAN to the tank, time rate of change of surface magnetic field (\dot{H}_θ) and collection of a fraction of the charge blown off the discharging dielectric surface.

Significant experimental results include the following:

1. The predominant source of excitation of the CAN is the blowoff of electrons from the dielectric surface and their subsequent motion in the fields created by charge embedded in the dielectric, charge induced on the conducting substrate, and other ejected charge.
2. Discharges of all magnitudes were observed up to a maximum dependent on material and exposure conditions for each of the three dielectrics examined.
3. The surface potential scans and photographs indicate that the relatively high lateral electric fields associated with dielectric edges, seams, and regions of overlap are discharge foci. The observed discharge patterns were, for the most part, asymmetric. The observed maximum fraction of stored charge removed in discharges were ~ 0.33 for Kapton, 0.8 for FEP Teflon, and 0.2 for the fused quartz coverslips. The corresponding blowoff fractions were 0.2 for Kapton, 0.2 for Teflon and 0.1 for fused quartz.

4. The return currents observed for the CAN grounded to the tank were positive (electrons flowing from tank to CAN), with rise times and half widths typically greater than $1 \mu\text{s}$. The maximum amplitudes observed were 126 A (Kapton), 150 A (Teflon), 50 A (fused quartz). According to the discharge model presented in Section 5, these are also typical of the blowoff currents which drive the response of the CAN.
5. The discharge process causes body replacement currents to flow on the sides of the CAN whose amplitudes and pulse widths are comparable to the return currents described in 4 above. Superimposed on the primary response which more or less followed the exciting pulse, were two higher frequency components. One with a characteristic frequency of 6 MHz (CAN grounded) or 12 to 13 MHz ($1 \text{ M}\Omega$ in series with ground strap) was attributed to the ringing of the combined CAN, ground strap tank system, and is believed to be an experimental artifact. The second had a primary frequency in excess of 50 MHz and is most likely due to the excitation of the lowest circumferential mode of the CAN (70 MHz). These higher frequency components enlarge the observed \dot{B} signals by as much as a factor of ten above that expected by differentiating the surface currents. However, the high frequency components carry relatively little energy as their amplitude is only a few percent or less than that of the predominant surface current component.

These data were compared to previously conducted electrical excitation experiments. The exciting sources were:

1. An arc discharge source of ca. 750 A peak, 40 ns half width.
2. A capacitive direct injection (CDI) of ca. 1 A peak, 10 ns half width for different drive plate spacings between 0.1 to 1.0 M.

In both cases, comparisons were made for the end of the CAN excited, corresponding to the electron spraying test configuration.

Analysis revealed that it was proper to compare the H_ϕ or surface current responses under the different exciting conditions if the drive pulses (electrical or blowoff) were normalized to the same peak current, while the \dot{H}_ϕ comparisons were made by normalizing the test data to the same rate of rise of the exciting current.

Significant findings include:

1. The arc discharge yielded a poor simulation of the surface current response produced by EID. Except near the discharge, the surface currents were two orders of magnitude too low, and the relative falloff of H_ϕ with distance from the arc was much too rapid.
2. CDI gives a relatively good simulation of the amplitude and spatial distribution of H_ϕ if compared to that produced by EID except as one approaches the drive wire. Here one sees an increase in H_ϕ as the axis of symmetry of the CAN is reached rather than the anticipated decrease expected for uniform EID blowoff excitation of the end of the CAN. The response pattern away from the drive wire can be fine tuned by adjusting the plate to CAN separation.

The major implications of the existing data base for the development of a valid system test procedure are the following:

1. The present MIL-STD 1541 arc is a poor simulation of the effects produced by blowoff as measured by the surface replacement current. The pulse width is much too narrow (10 to 20 ns versus 0.1 to 5 μ s) and the amplitude of the replacement currents are too low except possibly near the exciting arc.
2. In principle, CDI provides a better simulation of the surface current patterns produced by a blowoff discharge in a simple symmetric object. However, there may be practical limitations in developing a hardware implementation of the CDI technique which gives proper pulse widths and current amplitudes.
3. There are significant gaps in the data base needed to develop a validated system qualification test procedure for arbitrary satellite configurations.
4. There has not been a systematic effort made to correlate the ground test data here with P78-2 coupling measurements. This has been made more difficult because the P78-2 is not well instrumented to relate the limited data available from the engineering experiments (SCI-8B, TPM, SCI-7) to the discharge data base. For this reason, it would be valuable to complete the P78-2 coupling model begun under this program.
5. The limited amount of evidence available implies that the space environment may be more benign than can be inferred from the ground test discharge and coupling data. The latter has been based, for the most part, on exposure of dielectrics to monoenergetic electron beams (typically 10 to 30 keV) at fluxes

much higher than are typical for substorm conditions. A possible reason for the difference is that components of the space environment such as high-energy electrons (hundreds of keV to MeV), ions and UV typically not included in ground simulations, tend to reduce or eliminate discharging in spacecraft surface dielectrics.

6. In order to specify drive levels for conducting threat level system tests, the magnitude of the exciting discharge must be predictable for representative spacecraft dielectric materials and configurations and for realistic charging conditions. The most complete available set of scaling laws as a function of area were derived from measurements on uniform, circular, edge grounded samples irradiated with monoenergetic electrons. Examination of the data base for one material, Kapton, show variations about the mean of an order of magnitude for different measurements on samples with about the same dielectric area. The experiments described in this report highlight the importance of configuration effects such as edges, seams, regions of overlap in triggering discharges. In addition, the discharge patterns tend to be nonuniform. Thus, area scaling may be of limited value in predicting the behavior of large-area spacecraft dielectric structures. Not taken into account in the specification of these scaling laws are environmental effects of the type described in 5 above. Thus, care must be taken in using the scaling rules to predict the response for an arbitrary case. However, the existing evidence indicates that such rules provide a useful upper bound for area scaling.
7. There are significant gaps in our knowledge of details of the discharge emission process such as emission energy distribution, spatial distribution, plasma effects, which make it difficult to predict the response of typical spacecraft configuration to EID. Most of the existing ground test data is for either planar samples or for the response of a simple right-circular cylinder. Attempts to reproduce the observed response of more complicated spacecraft simulations containing reentrant geometries such as antennae have not been successful. However, the ground test data base is extremely limited. The electrical testing performed on the SCATSAT during Phase I of this program demonstrate in a quantitative manner how the addition of booms alters the basic body response. It would be valuable to complete the SCATSAT electron

spraying tests to enlarge the data base on the EID response of a satellite-like model and to provide a quantitative basis for evaluating the P78-2 coupling measurements, both to better understand what is happening to that spacecraft and also to provide a needed correlation between ground testing and the space environment.

2. BACKGROUND

2.1 GEOSPACE ENVIRONMENTS

Geospace is the term given to that region of solar influenced space into which the effects of the earth's presence are inserted. The physical properties of our planetary system are dominated by the sun through its gravitational influence, its charged particle output and the cyclic nature of its emissions.

The photon output as measured at the top of our atmosphere is shown in Figure 1. It is approximately a blackbody output with temperatures between 4,000 and 6,000°K on which is superimposed some strong spectral lines, especially below 1500 Å. These emissions, arising mainly from H and He transitions, vary considerably with the 11-year and shorter cycles. The average total photon energy flux is about 1400 watts/m². Any vehicle operating outside the atmosphere encounters the full photon environment. The consequent photoelectric inducement serves to maintain the craft in potential equilibrium with its immediate surroundings. Abrupt eclipse by the solid earth and local shadowing can stimulate transient behavior by elimination of photoelectron emission.

The major effect in the geospace cavity concerns the particle flux and magnetic field anomalies caused by the earth's presence. Figure 2 shows the results of the interaction of solar wind particles with the substantial geomagnetic field. The dipole field lines are swept into a roughly paraboloidal shape with the upstream magnetopause boundary lying between 5 and 10 earth radii (R_E), depending on the solar condition. The plasma conditions within the magnetosphere vary markedly from region to region. In general, low altitudes (plasmasphere) particles may be characterized as having high densities (10 to 1000 cm⁻³) and temperatures of a few eV. At higher altitudes, in the plasmasheet, the densities are ~ 1 cm⁻³ and the mean energies are several keV. The environment at stationary orbit is governed by the interplay of these regions, which is, in turn, determined by solar activity. At a high level it is possible for such a satellite near local noon to pass through the bowshock, created by the interaction of the supersonic particles and the geomagnetic field, and out into the solar wind.

ORIGINAL PAGE IS
OF POOR QUALITY

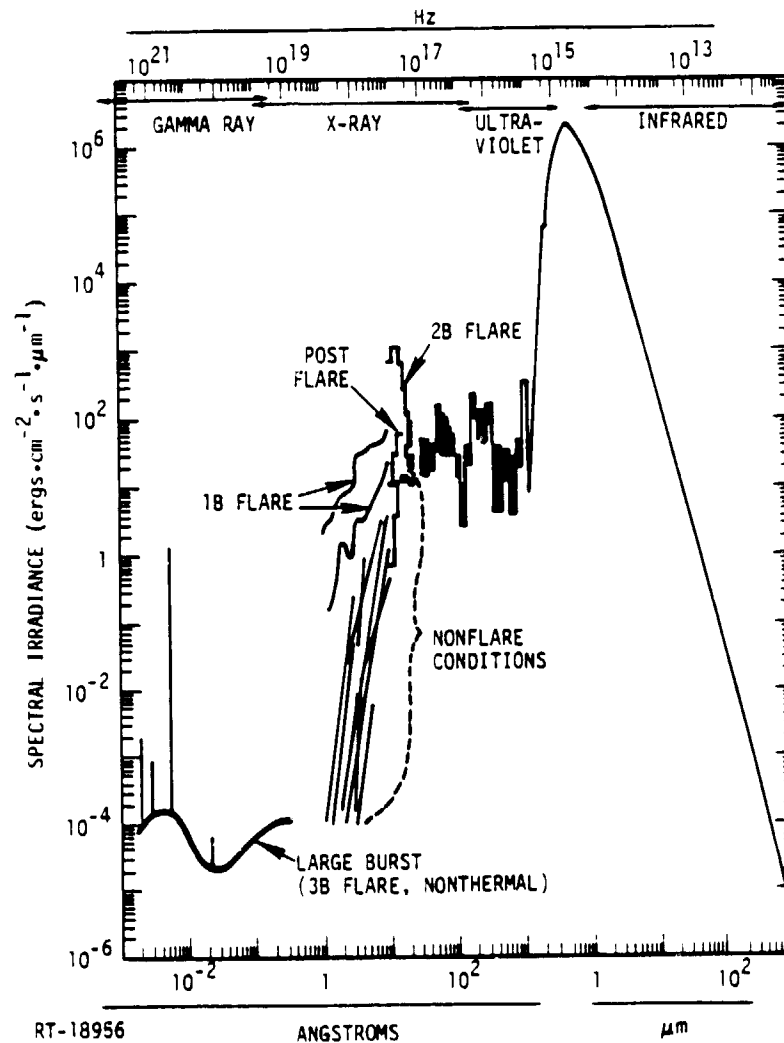
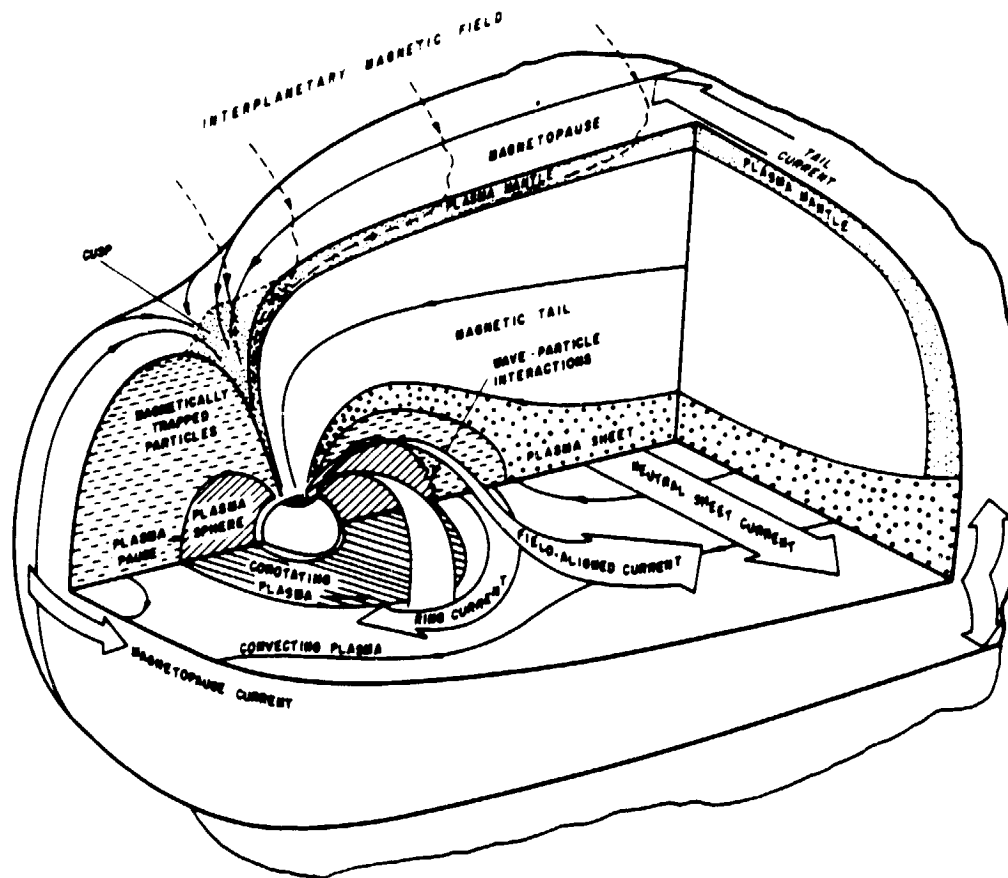


Figure 1. The solar spectrum

Solar particles enter at irregularities in the magnetosheath. The magnetosphere is further supplied from the ionosphere and stores the particles and hence their energy; in its tail, and in the plasma sheet and ring current. Flow and release of the energy, and coupling among the regions influence, for instance, the behavior of the ionosphere, and produce such familiar effects as magnetospheric substance and auroral displays (Refs 2-7). The variability of conditions during a 12-hour period may be seen in Figure 3 taken from Reference 7. This is a representation of simultaneous particle flux observations at the ATS-5 satellite and ionospheric emissions near the same magnetic field line. Plots b and c are grey scale records of UT-energy-intensity variations of electrons and protons, while h shows their characteristic energies and energy fluxes.



RT-20704

Figure 2. Magnetosphere (after DeForest)

These particles stimulate photon emission in the upper atmospheric species O (e and i) and $N_2^+(j)$. H_β radiation from charge-exchanged precipitating protons is shown in f. Plots d through k are grey scale representations on UT-latitude-intensity axes.

It can be seen that the differential fluxes, temperatures and energy fluxes vary significantly even in this relatively quiet period. Characterization of any geospace location depends on many parameters, and must be made either with accurate knowledge of magnetospheric conditions or as average or worst-case situations. Garrett (e.g., Refs 8,9) has reviewed observations at stationary altitudes. Normal or mean conditions may be inferred from his data.

Figure 4 shows frequencies of occurrence of current densities and characteristic temperatures of electrons and ions as measured by ATS-5 and ATS-6. The first of these vehicles operated near solar maximum, the second during minimum. Particle velocity distributions at synchronous orbit are of neither Maxwellian nor isotropic.

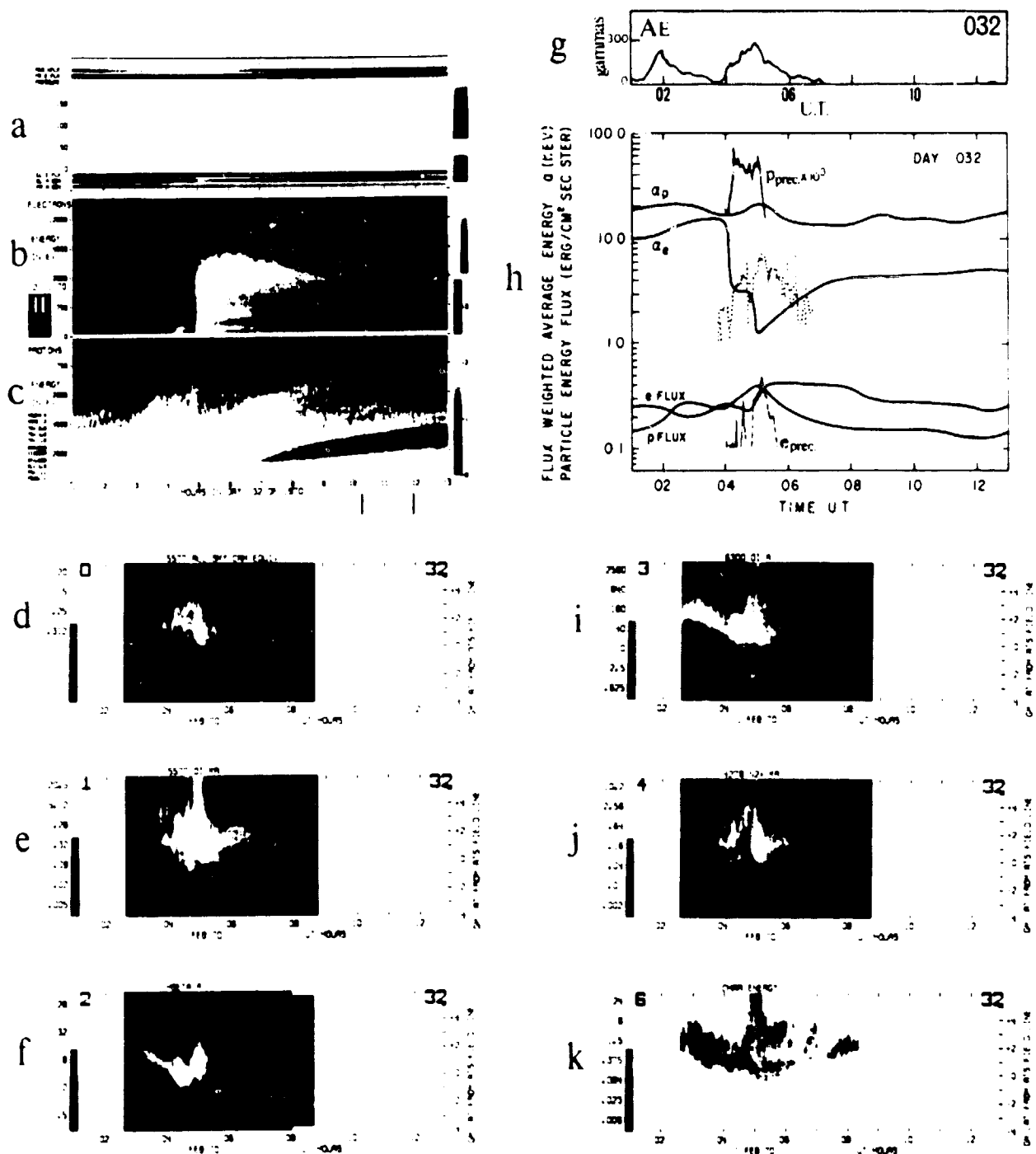


Figure 3. ATS 5 particle spectrograms (parallel detectors), keograms, ATS 5 energy fluxes and average energies, precipitated energy fluxes and average energies, and AE indices for day 032, 1970. Left column, from top to bottom: (a) Top line plot is the H component of the magnetic field at ATS 5 (in gammas), and bottom line plot is detector pitch angle (in degrees); (b) Electron spectrogram; (c) Proton spectrogram; (d) All-sky camera equivalent keogram; (e) 5577 O I keogram; (f) $H\beta$ keogram. Right column, from top to bottom: (g) AE plot; (h) ATS electron and proton energy fluxes and electron and proton average energies (flux weighted). Also shown are precipitated proton and electron fluxes derived from photometric data at the predicted ATS 5 field line position, and the average energy of precipitated electrons (plotted in crosses); (i) 6300 O I keogram; (j) 4278 N_2^+ keogram; (k) Characteristic energy keogram.

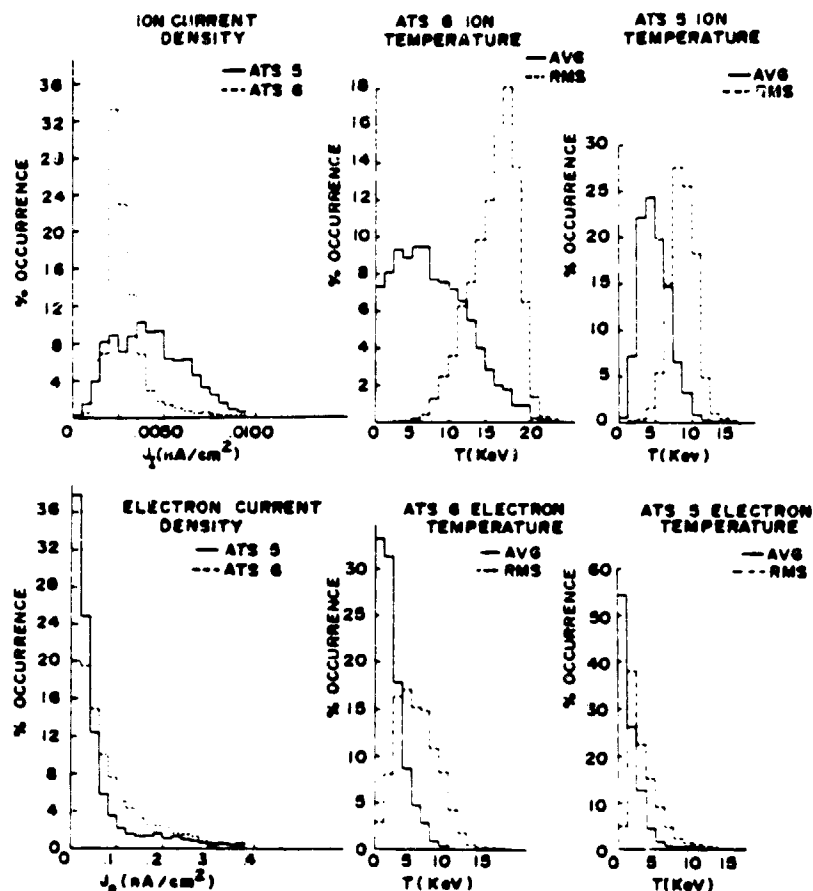


Figure 4. Histograms of the occurrence frequencies of the electron and ion temperatures and current at geosynchronous orbit as measured by ATS-5 and ATS-6. $T(\text{AVG})$ is $2/3$'s the ratio of energy density to number density; $T(\text{RMS})$ is one-half the ratio of particle energy flux to number flux.

Fair representations may be made by assuming the distributions to be composed of the sum of two or more Maxwellians (Refs 10,11). By assuming a double structure average values of electron and ion currents and temperatures were derived from the ATS data and are given in Table 1.

In examining the figures for mean currents and energies, and assuming a neutral bulk plasma, we have

$$\frac{J_d}{J_i} \sqrt{\frac{T_{li}}{T_{le}}} = 40.6 \approx \sqrt{\frac{m_p}{m_e}} = 42.3, \quad (1)$$

which satisfies the simple physical principles.

Table 1. Mean Values of Electron and Ion Current Densities and Characteristic Energies Inferred Using a Double Maxwellian Velocity Distribution

	Weighted Averages from		Mean	Mean Worst
	ATS-5	ATS-6	of Two	Case (10%)
			Averages	Occurrence)
Electrons				
J_e pa/cm ²	63.0	87.0	75.0	275.0
T_{1e} keV	1.8	2.3	2.1	
T_{2e} keV	3.3	5.8	4.6	
Ions				
J_i pa/cm ²	4.1	2.3	3.2	7.6
T_{1i} keV	4.6	7.9	6.3	
T_{2i} keV	8.7	16.3	12.5	

The higher speeds of the electrons in an isotropic plasma causes the spacecraft to become charged negative with respect to its surroundings. This has become a familiar observation since its early measurement (Ref 12). Of prime concern to the present effort is that the net negative bombardment induces differential potentials among various materials of the satellite surface. The time-dependent nature of the charging profiles depends not only on the plasma characteristics but also on such material parameters as size, thickness, boundaries, photoelectric response, photoconduction, secondary emission, stopping power, and bulk dark conductivity.

2.2 PRIOR KNOWLEDGE

2.2.1 Theoretical Investigations

The idea that a spacecraft would react electrically to varying plasma conditions developed concurrently with knowledge of the geospace characteristics. Theoretical considerations (Refs 13-17) surmised that the predominance of electron fluxes would lead to spacecraft attaining negative potentials with respect to their surroundings until the difference became great enough to exclude most of the bombardment. It was recognized that solar ultraviolet illumination would stimulate a photoelectric response that would tend to reduce the negative potential. Of less theoretical concern were the magnitude of possible potential differences among different portions of the spacecraft, and the methods by which such differences might be induced. Little considered were the consequences of rapid potential equalization induced by discharge between adjacent areas. The resultant transients induced in spacecraft wiring was of potentially sufficient magnitude to interfere with the spacecraft systems.

At the same time interest was growing in the electromagnetic effects of nuclear weapons on military space systems. For satellites outside the atmosphere, the most important of these is the system-generated electromagnetic pulse (SGEMP) is created by the interaction of weapon-produced x-radiation with the spacecraft structure and components. The resultant currents induced in cabling can cause circuit upset or burnout. This necessitates the protection of sensitive circuitry and the sealing of possible entries for electromagnetic energy. The technology of dealing with these phenomena, both theoretical and practical, is relatively advanced. Techniques for testing the responses of large systems are available, and the treatment of their effects by computer modeling has been successful.

The related investigation of electrostatic effects on space systems, had been relatively neglected until the advent of the SCATHA program. The heavy use of sensitive, low-power integrated circuit technology has prompted their consideration in spacecraft design due to the high susceptibility of such sensitive devices to transient disturbances. The success of EMP and SGEMP analysis and hardening techniques suggested that related methods be used to address and solve the electrostatic discharging problem. Thus, the modeling of discharge coupling was achieved by adaptation of SGEMP codes through the inclusion of source terms appropriate to the phenomenon. The relevant electrical test techniques have been copied from those developed to simulate SGEMP effects. The adaptation of SGEMP analysis codes to model EID coupling was discussed in Reference 1. The adaptation of SGEMP electrical simulation techniques to reproduce the EID response was also discussed in References 1 and 2 and will be reviewed in more detail in the second report of the present study.

2.2.2 Spacecraft Observations

In the early years of space flight, little consideration was given to the possible consequences of static charging. There were several reasons for this. First, theoretical work mainly treated the integral behavior of a satellite, with less regard for relationships among different materials. Electronic systems were less sensitive to transient effects by virtue of their required working parameters. Any noticeable consequences, such as logic upsets, were assumed due to other causes or to general lack of reliability.

Particle flux measurements were made at relatively high energies. The analysis and display of such data was driven by interest in energy, spatial and temporal dependences of the population on acceleration processes due to solar wind and

BLACK AND WHITE PHOTOGRAPH

magnetospheric behavior. It was not until detection of low energy particles (<100 eV) and methods for display of flux characteristics over long periods were made (e.g., Ref 3) that an idea of charging morphology could be gained. An integral measurement of the total spacecraft potential was made from the UCSD particle spectrometer on the stationary satellite ATS-5 (Ref 12). The vehicle is bombarded by a net negative flux, but, in sunlight maintains its potential close to that of the surroundings by photoelectron emission. Entry into eclipse results in the collapse of the photoelectron cloud and a rapid rise of the satellite to a negative potential. This could be detected by changes in the characteristics of the detected particle flux. Figure 5 shows an eclipse charging event from ATS-6 where, as the vehicle attains a potential of ~ -10 kV the electron flux disappears and the heavy low energy ion flux is accelerated to give a high differential counting rate near 10 keV. After about 15 minutes emergence from eclipse restores its ability to emit electrons and adjust its potential.

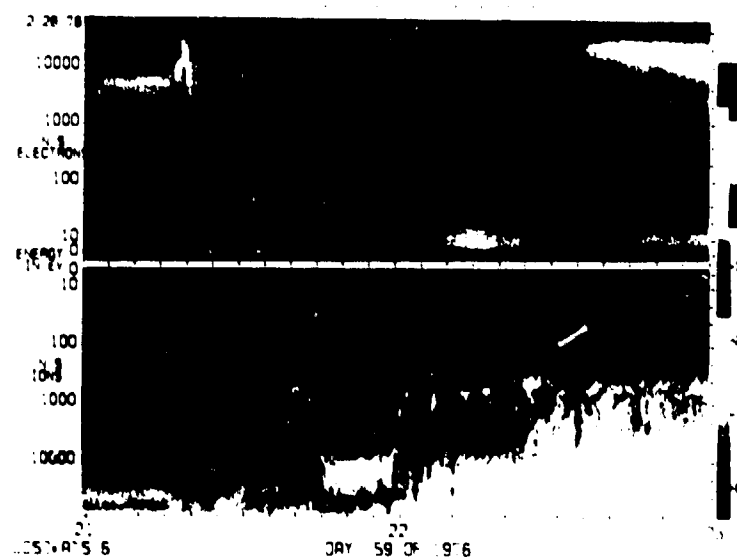


Figure 5. Spectrogram of Day 59, 1976, from ATS-6 (see DeForest and McIlwain, 1971, for explanation of scales). The dropout in the ions between 2145 and 2200 UT occurs simultaneously with satellite entry into eclipse and reflects in eV the negative potential in volts, V, on the satellite as it became charged due to the loss of photoelectrons.

Although integral charging per se is unlikely to cause any system problems, it was recognized that, due to differences in response to various radiation, high differential voltages could appear among surface materials at such a time. Furthermore, it was probably not necessary for the spacecraft to be in eclipse. Differential potentials could

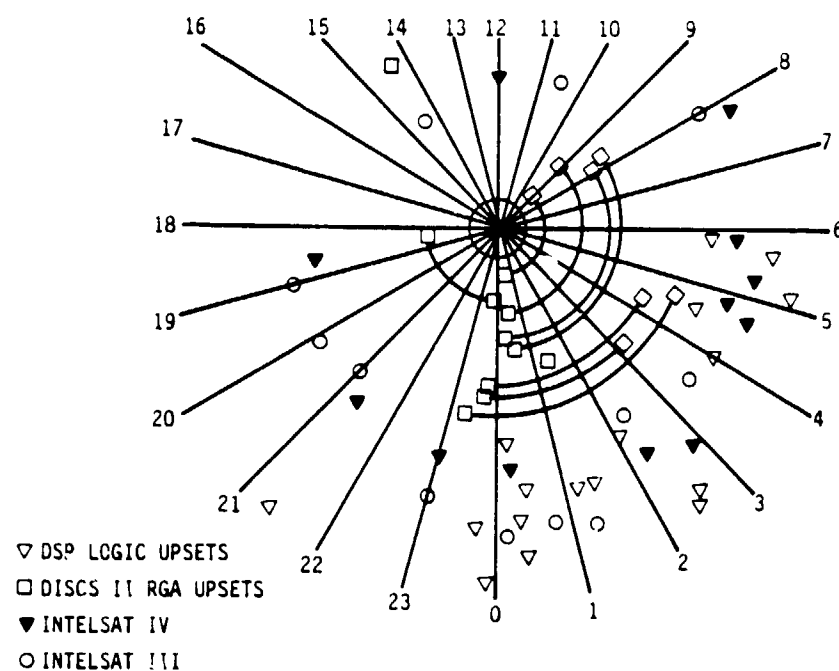
be created on the antisolar surface, especially on a stabilized vehicle, or even on the sunlit side if the incident electron flux were to exceed the secondary and photoelectron emission.

Little design effort was made to avoid these effects, although the phenomenon was easily understood. But, as no spacecraft had been equipped to make an explicit investigation of these effects, past occurrences and their causes had to be inferred in a secondary manner, and the findings presented statistically. Studies were made, for instance, on the dependences of logic upset occurrences, presumed due to discharges, on satellite local times and on geomagnetic conditions (Refs 18-20). Figure 6 shows the times of events observed in the records of four satellites. There appears to be a concentration of discharges between midnight and dawn. This is a period renowned for appearances of enhanced particle fluxes (injection events) due to geomagnetic substorms as can be seen in the spectrogram of Figure 3. This dependence, then, is not surprising. Nor is that of Figure 7, where the discharge rate as a function of the daily average, A_p , of the geomagnetic index a_p . a_p is a linear representation of maximum excursions in a three-hour period of the surface magnetic field at several observing stations around the northern auroral zone. Its unit is approximately 2γ ($1\gamma = 10^{-9} \text{ w/m}^2$) and indicates the degree of disturbance of the earth's field due to solar wind on internal (substorm) effects in the magnetosphere.

The conclusions, by this time, were quite clear. Sufficiently enhanced fluxes of electrons of energies above a few keV could charge surfaces to differential potentials at which discharges could occur. Photon and ion irradiation could influence the rate and ultimate voltage depending on their characteristics and those of the materials. The attraction in using such sensitive devices as LSI circuitry made their protection and the minimization of the effects of discharge sources necessary. The SCATHA program addresses these subjects by encouraging the study of charging and discharging phenomena, both in space and by simulation, and by the development of appropriate materials. The P78-2 satellite was designed to characterize the geostationary environment, to attempt active potential control by the use of electron and ion emission, and to record discharge EM effects around and within the vehicle.

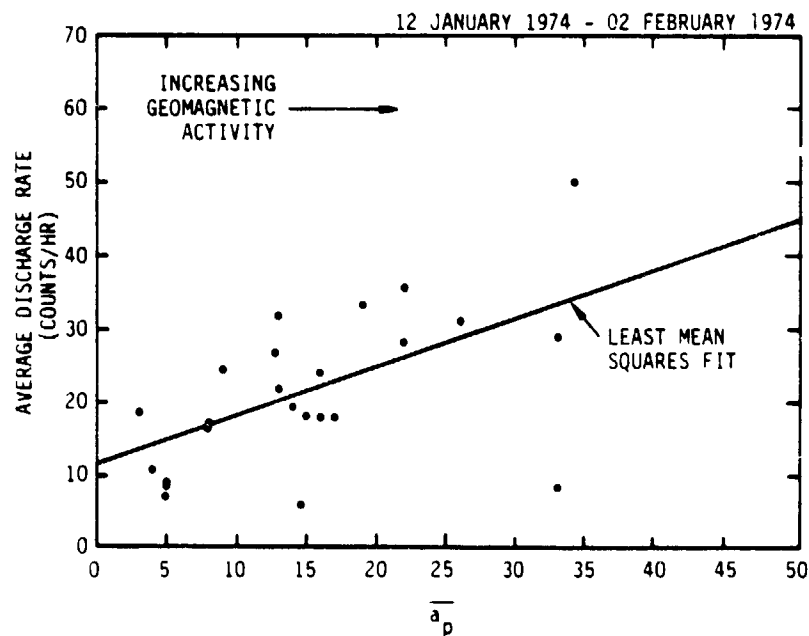
The P78-2 instrumentation allowed accurate determination of particle and magnetic and electric field environments. Unfortunately, there are inadequacies in the measurement of discharge transients because of limited external electromagnetic current and field sensors with proper frequency response detection, and that photon flux

ORIGINAL PAGE IS
OF POOR QUALITY



RT-20706

Figure 6. Local time dependence of circuit upsets for several DoD and commercial satellites (McPherson and Schober, 1976). Radial position has no significance.



RT-20707

Figure 7. Daily average discharge rate as a function of daily average a_p (from Shaw et al., 1976)

properties are not determined. Further, the vehicle is constructed as a double Faraday shield which markedly reduces the magnitude of internal EM fields and currents.

The CAN tests were designed to investigate the nature of charging of common spacecraft dielectrics in a simulated environment, and to determine the responses of a simple object under discharge conditions. The space environment simulation was chosen to simulate the important aspect of space conditions responsible for charging, the measurements were designed to complement the data obtained in situ.

2.2.3 Ground Test Measurements

Although the phenomenon of EID is well understood in principle, there is an absence in some areas of detailed knowledge which is necessary for accurate prediction and control in a space environment. The secondary and photoelectron response of many materials is not well known. Nor are there detailed characterizations of such parameters as charging rates as functions of incident particle flux and energy, breakdown fields for various materials and geometries, and relative amounts of charge transferred. These cause some uncertainties in modeling efforts (see, for example, References 21 and 22). Until these parameters are well defined, analysis and prediction of spacecraft electrical responses will lack the accuracy probably attainable.

Much of the material responses are known for metals (e.g., Refs 23-26), however, those for dielectrics have not received the same attention (Ref 27). Their investigations have been stimulated by the current program (Refs 28-31). Some of the work has been used for recent modeling calculations (e.g., Ref 32) and studies of material discharge (Refs 33-35).

Large-scale simulations of the responses of complex structures to EID are confined to the present series of studies (Refs 1,2,36) attempting to link electrical injection techniques with discharges occurring in laboratory substorm environments (low energy electrons, ions, and VUV photons), and a parallel measurements on an object similar to the CAN (Ref 37). This latter work attempts to explain observations of blowoff and surface currents by a straightforward model of the blowoff mechanism which is an extension of that first proposed in Reference 1. The first-order comparisons between measurements and prediction by the ABORC code (Ref 38) appear to give encouraging results.

PRECEDING PAGE BLANK NOT FILMED

3. EXPERIMENTAL

3.1 TEST OBJECT

The CAN is a hollow aluminum cylinder of 136 cm diameter and 81 cm length. Its attraction as an object for EM analysis is that its symmetry makes for relative ease of modeling. In addition, electrical testing data was performed on this object under Contracts DNA001-78-C-0180 (Electron Induced Discharge Testing, Modeling and Analysis for SCATHA) and AFWL F29601-74-C-0105 (SGEMP Analysis Verification) (Ref 39). An 80-cm diameter removable panel on each face allows access to internal equipment and easy mounting of dielectric samples.

The samples were formed as follows:

1. Kapton. A 75-cm diameter circle was made from 0.001-inch thick Kapton, 18-inch wide tape (Figure 8). There was a 6-cm overlap and fixture to the mounting panel was made by its 0.0015-inch acrylic adhesive.
2. FEP Teflon. A 75-cm diameter circle was formed from 0.005-inch thick, 4 inch wide tape (Sheldahl 401900). The top four joints had a 2-cm overlap, the lower three were butted (Figure 9). Attachment was made with the tapes 0.002-inch conductively loaded acrylic adhesive. The back of the tape was silvered, backed by Inconel.
3. Simulated Solar Panel (see Figures 10 through 12). The base was a 0.011-inch fiberglass sheet epoxied to a 1/8-inch aluminum back panel. Strips of 2-inch copper tape were laid on the fiberglass and 2 x 4 cm fused silica (Corning 7940) cover slides (0.006-inch thick) were attached in pairs to the tape with Sylgard 184. The slides have a quarter wave magnesium fluoride antireflection coating. The lower half of the array was laid with MgF, the upper half with SiO₂ faces exposed. Realistic backplane wiring and blocking diodes copied from the P78-2 Solar Array were included.

With the CAN suspended, the dielectric samples were vertical and faced toward the radiation sources. The transient surface currents created by discharges were



Figure 8. Kapton sample

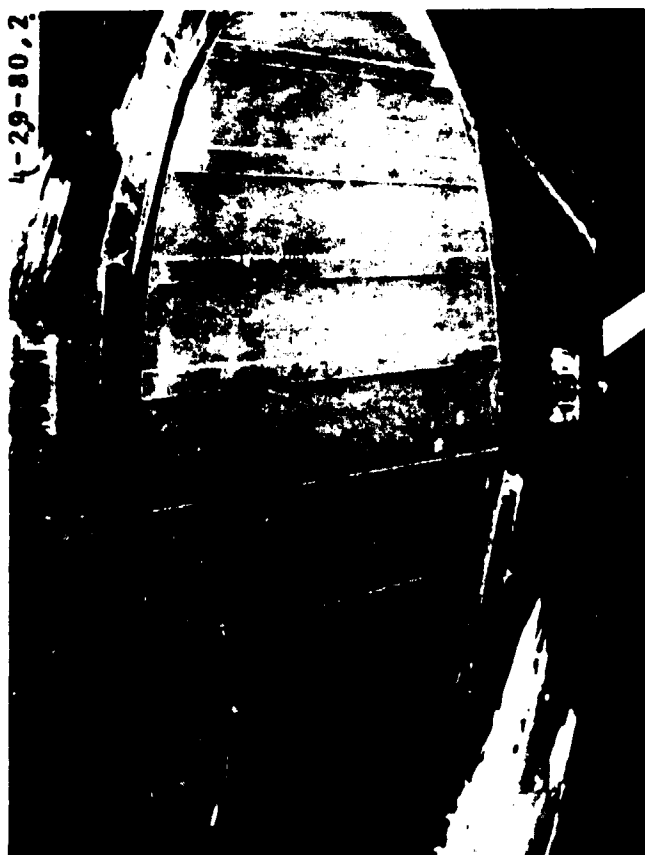


Figure 9. Teflon sample

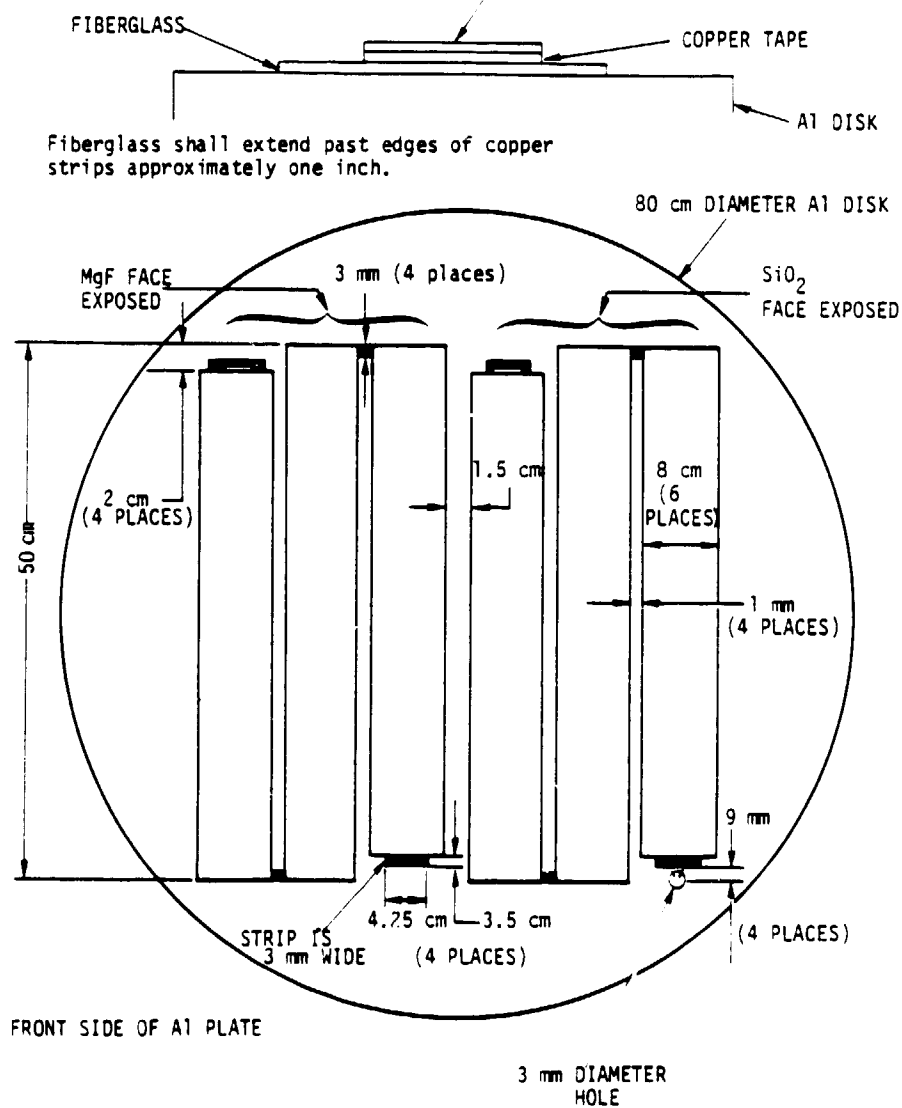


Figure 10. Solar array mockup

ORIGINAL PAGE 03
OF POOR QUALITY

MgF₂ face up on 3 copper strips on left.
MgF₂ face down on 3 copper strips on right.
Dark areas are copper strips soldered to larger copper strips.

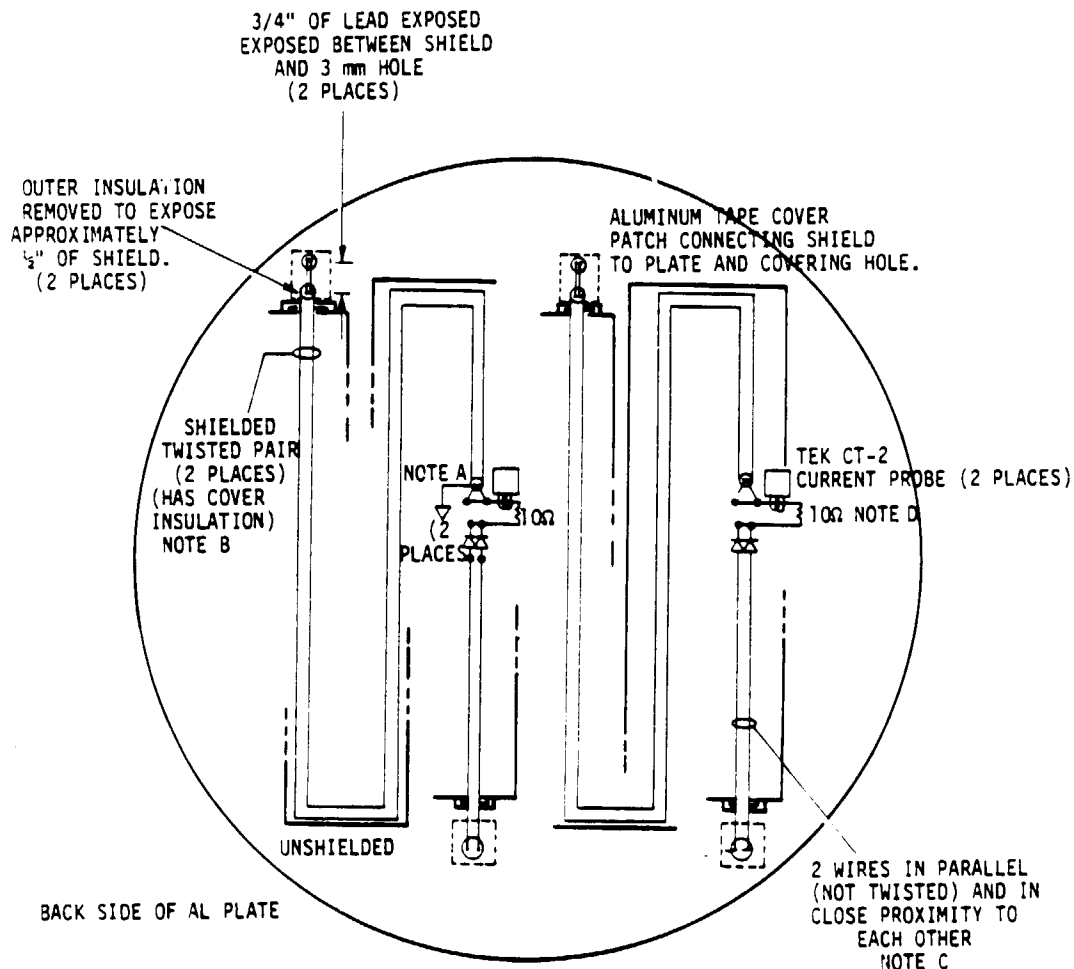
MgF₂ (2 cm x 4 cm x 6 mil)
COVERING ALL COPPER TAPE
EXCEPT DARK AREAS



RT-19143

Figure 11. Simulated solar panel (front)

ORIGINAL PAGE 16
OF POOR QUALITY



SHIELD CONNECTED TO ALUMINUM PLATE USING A GROUND STRAP AND SCREW-DOWN TERMINAL. STRAP LESS THAN 1 INCH LONG. EXPOSES TWISTED PAIR LENGTH LESS THAN 1 INCH.

INSULATED SHIELDED TWISTED PAIR NO. 26 AWG CORE WIRE

LEADS CONNECTED TO NOMINAL 1/2 INCH SOLDER LUGS MOUNTED ON PC BOARD MATERIAL
DIODES ARE SILICON

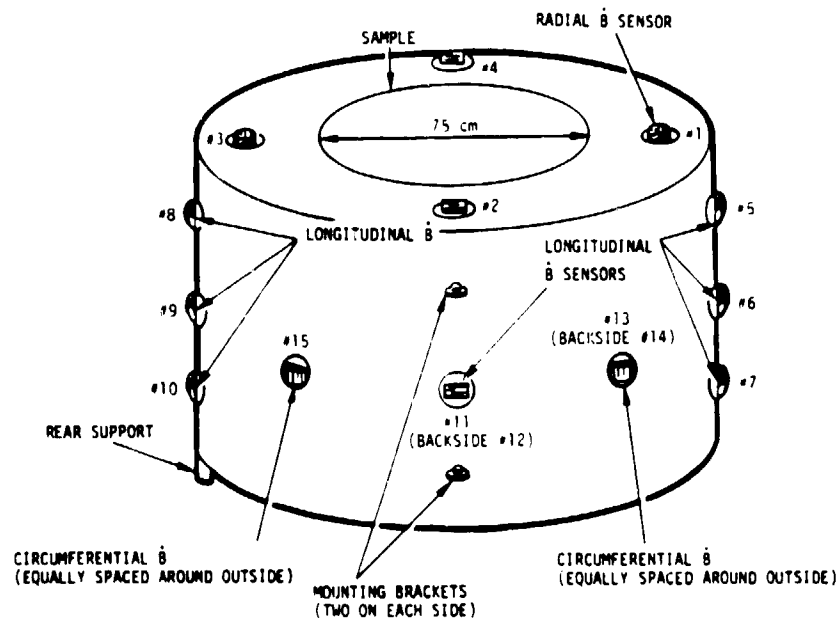
WIRES LIE FLAT ON AL PLATE SECURED WITH POTTING COMPOUND

RT-19144

Figure 12. Simulated solar panel (rear)

ORIGINAL PAGE
OF POOR QUALITY

measured by \dot{B} sensors, EG&G models CMLX3B and CMLX6 mounted on the external surface in the locations shown in Figure 13. Sensors 1 through 4 detected radial currents on the front face. Numbers 5, 6, 8, 9, 11 and 12 measured longitudinal, and 13, 14 and 15 circumferential transients on the curved surface. Assuming $|\dot{B}|$ to be proportional to $|\dot{j}|$ these provided determinations of surface currents by integration. Outputs from the sensors were taken by balanced line to baluns manufactured by IRT. These contain Z match high frequency balanced/unbalanced transformers rated for use between 100 kHz and 1 GHz. A diagram of the instrumentation system is shown in Figure 14. Connections internal to the CAN other than fiber optic cables were made by semi-rigid cable with SMA terminations to ensure EM shielding.



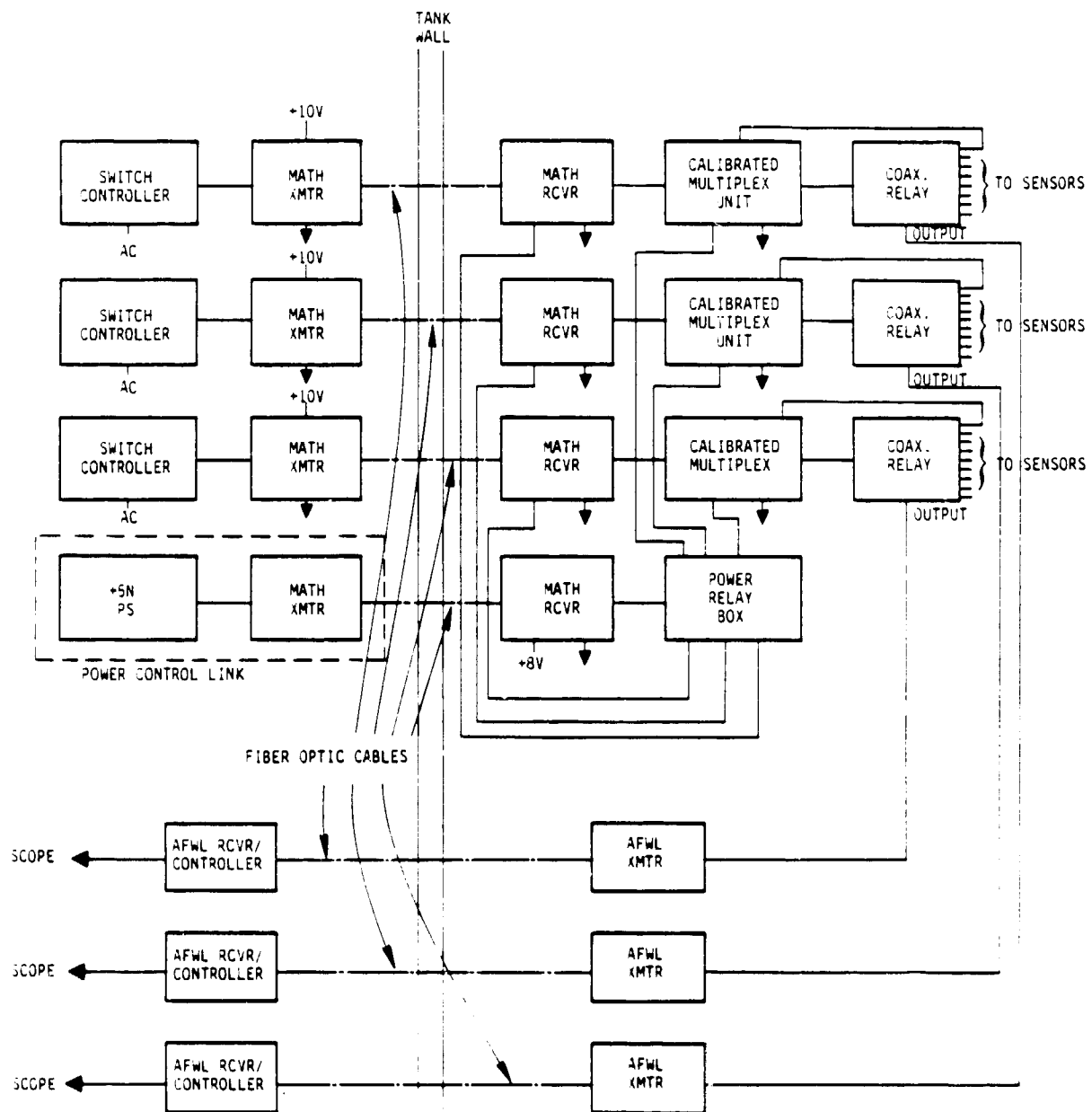
VG-22

RT-18970

Figure 13. External sensor location on the CAN. Not shown are internal cabling, fiber optic transmitters, coaxial switches, fiber optic cables and external grounding strap. Sensors 1-4 are CMLX3B, 5,6,8,11,13 are CMLX6 and 7,9,12,14,15 are CML3. The line of sensors defined by 8,9 and the rear support faced the bottom of the tank. The arrows show the direction in which an increase in \dot{B} produces a positive sensor output.

The basic analog data system shown in Figure 14 was designed and constructed by IRT. At the heart of each system was a programmable coaxial switch which had eight input channels and one output channel. Switch bandwidth was 0-300 MHz (upper 3 dB point). Each switch had a calibration/multiplex unit which provided the matching logic and a square wave calibration system signal. The relay unit also contained Ni CAD

ORIGINAL PAGE IS
OF POOR QUALITY



RT-00705

Figure 14. IRT analog fiber optic data system

batteries to operate the switching logic (+6V) and the relays (+26.4V). The switch control circuitry was driven by a controller outside the tank. Control signals were sent over a MATH type digital fiber optic link. The analog signal output through the Matix switch was input to the transmitter of a 250 MHz AFWL fiber optic link built by Lockheed. These units had their individual controls, including a calibration and attenuation capability. The electrical signal output from the AFWL receivers was recorded on either a Tektronix Series 7000 scope or Biomation Type 6500 or 8100 transient digitizers. Recording devices were matched to sensor channels to provide a bandwidth adequate to monitor each sensor. Because the scopes had bandwidths of 400 MHz to 500 MHz, the upper frequency signal monitoring limit was determined by the bandwidth of the AFWL/Lockheed link.

A total of three such coaxial switch and fiber optic systems enabled simultaneous monitoring of currents at three separate points on the surface. Power for all systems was controlled from outside the tank by a separate fiber optic link which operated a set of relays in series with the batteries for the MATH receivers and switch controllers inside the tank. This was important to maximize useful battery life.

3.2 CAN MOUNTING AND EXTERNAL MEASUREMENTS

The test object was mounted and tested in Tank 5 of the Electrical Propulsion Laboratory at the NASA Lewis Research Center. The tank is a 15-foot diameter by 63-foot long cylindrical steel tank, with a 9/16-inch thick milled steel outer shell and 1/8-inch thick Type 304 stainless steel liner. The tank also contains blackened LN₂ baffles that can be used to simulate the cold background of deep space at an inner diameter of 13 feet, 6 inches.

The object was connected to tank ground by a low impedance braided ground strap. The resistance of this connection was arranged at various times to be 0, 10^5 or $1\text{ M}\Omega$, the last being chosen so that the CAN was electrically decoupled from the tank during the discharge, as shown in Figure 15. This high resistance kept the conducting spacecraft frame at the same potential as the tank while the dielectric surfaces are charged to high negative potentials. The time constant of the grounding resistor and stray capacitance between test object and tank ($C \approx 10^{-10}\text{ F}$) is $\approx 100\text{ }\mu\text{s}$; long compared to discharge pulsewidths (ca. $1\text{ }\mu\text{s}$). However, some of the high impedance data indicates that there were additional inadvertent coupling paths between the CAN and tank which reduced the RC time constant (q.v. Section 5.3).

ORIGINAL PAGE
BLACK AND WHITE PHOTOGRAPH

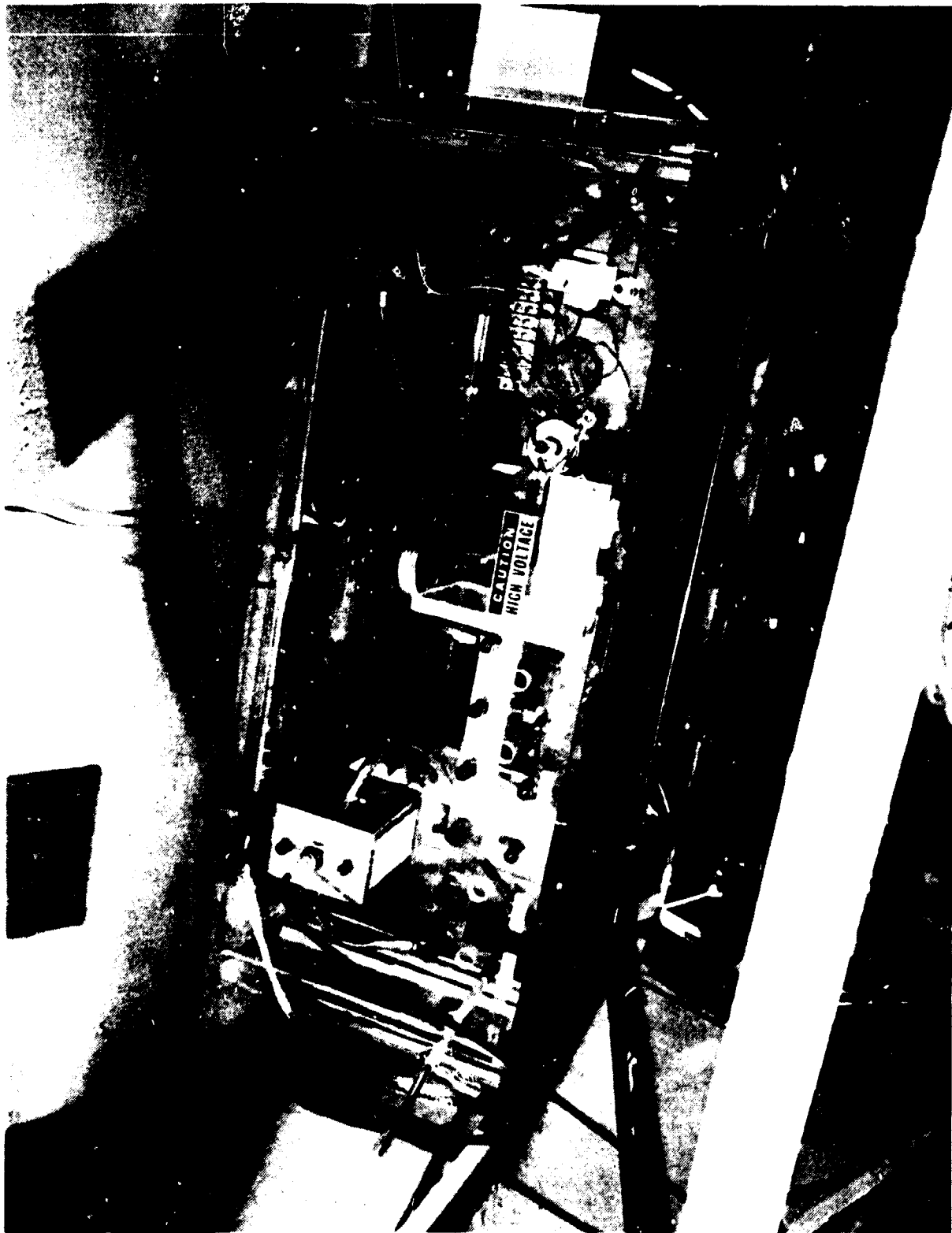


Figure 15. Resistor patch panel

ORIGINAL PAGE IS
OF POOR QUALITY

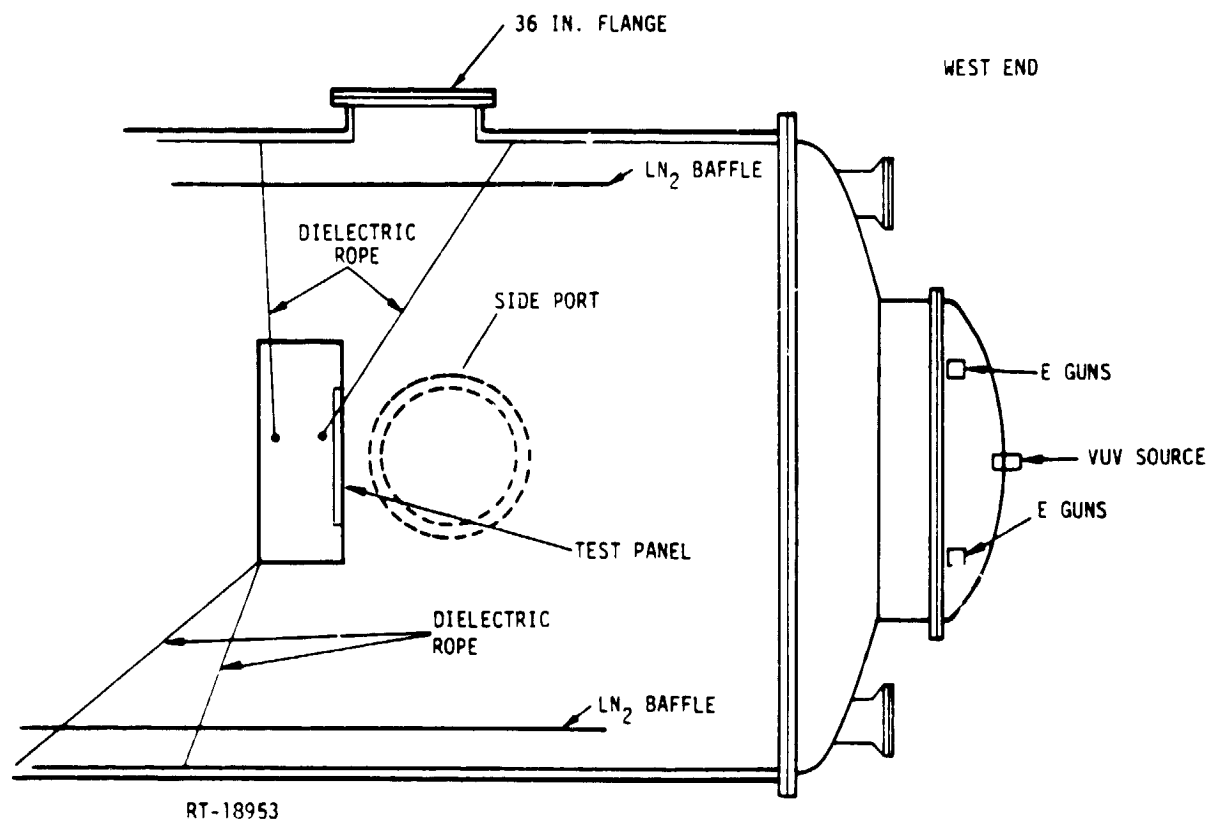


Figure 16. CAN and source locations in Tank 5

Mounting of the object within the tank is shown in Figures 16, 17 and 18. The CAN was suspended with five dielectric straps so that its flat faces were vertical and its axis of symmetry coincided with the center line of the chamber. A viewing port on each side of the tank allowed visual time-lapse photographs of the discharges to be taken.

Four NASA electron guns were mounted in the end cap of the tank. Their energies were variable up to 20 keV and could deliver a total of about 5 na/cm^2 to the front face of the CAN. A low pressure Krypton VUV source was located in the center of the end cap mounted in a 1-1/8 inch vacuum fitting. Its tuning and output was controlled from outside the tank.

Source flux and surface potential measurements were made by detectors carried on the probe arm whose position could be varied as shown in Figure 19. In practice the probe arm was swept across the front face of the CAN at a uniform angular rate by a motor controlled from outside the tank. Four TREK electrostatic potential probes

ORIGINAL PAGE 13
OF POOR QUALITY

scanned the front face. Four Faraday cups mounted opposite to the TREK probes monitored the charging current density. The output of the VUV lamp was determined with a Scientific Services Model 203F photodiode with a KBr photocathode mounted so that it crossed the center line of the sample.

Figure 20 is a double exposure in which the dielectric containing panels is removed to show some of the internal instrumentation. A large Faraday cup (shown in Figure 19) was mounted in front of and below the CAN to detect blowoff charge. The CAN grounding strap was attached to the center of the rear face to preserve symmetry of response. Determination of current trickling from the CAN during charging was made by an electrometer across a voltage divider at the ground end of the strap. Replacement current flowing back to the object after a blowoff was measured by a Singer 91550-2 current probe around the ground line.

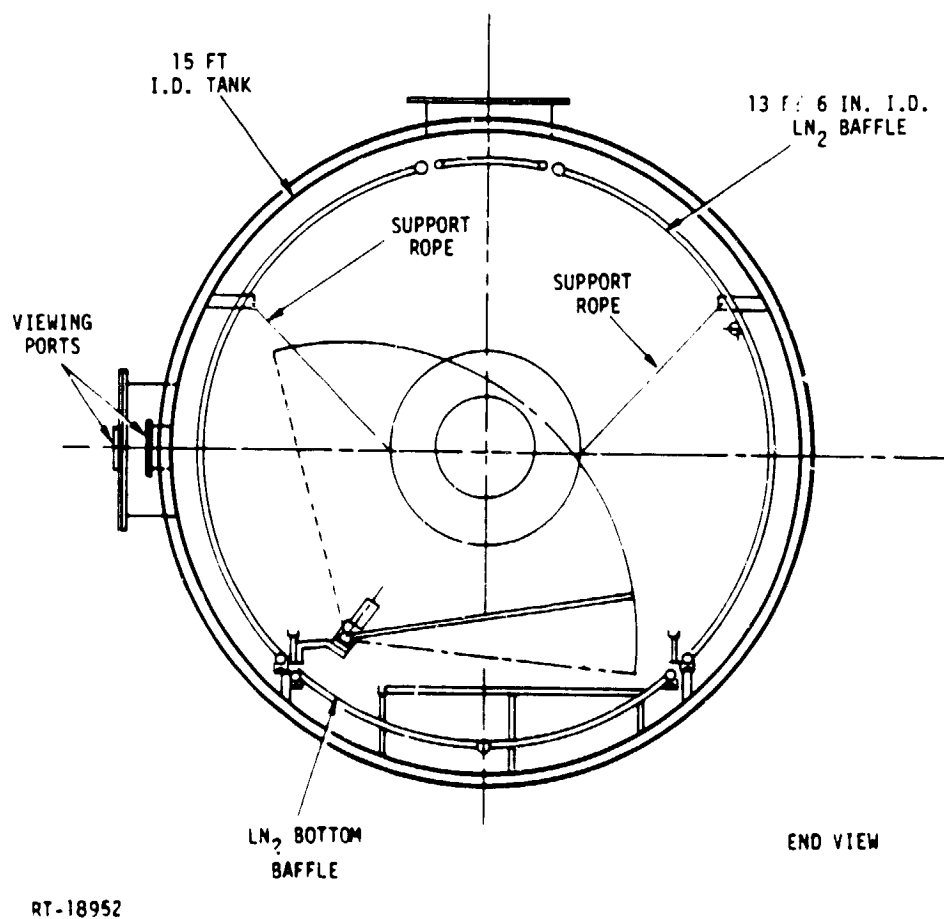
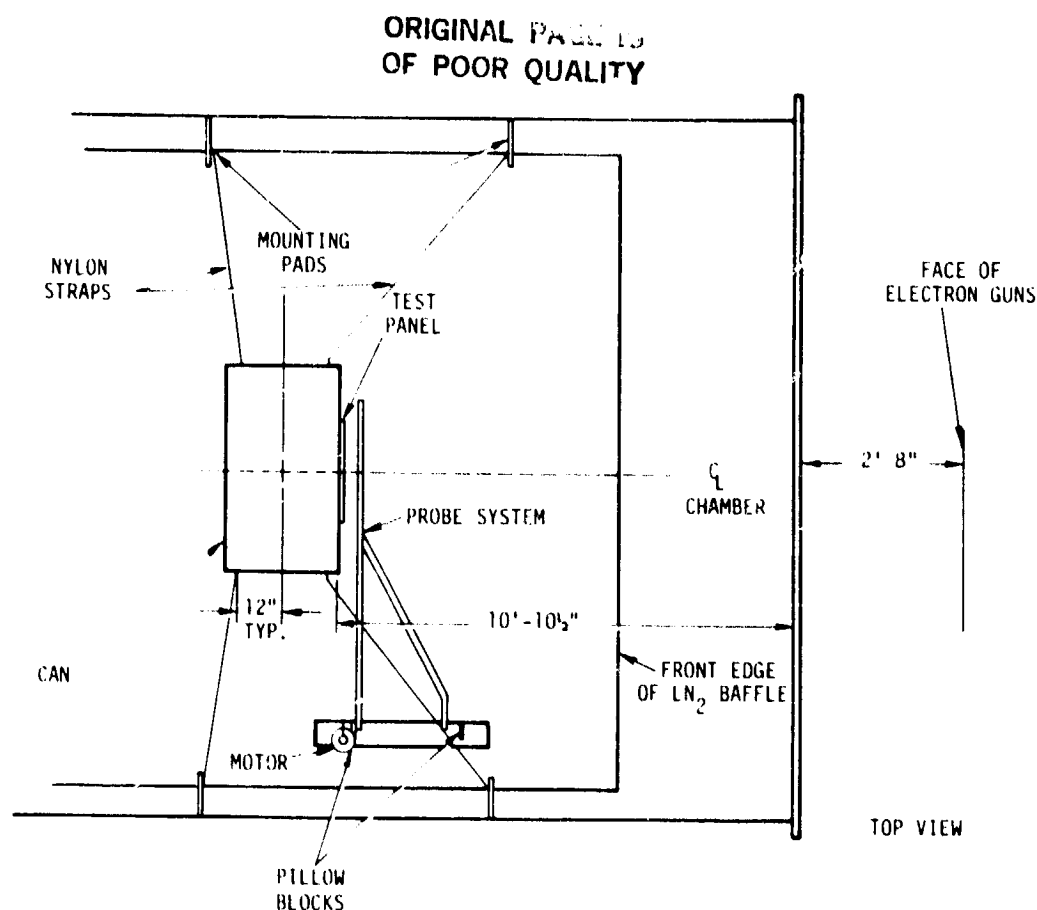


Figure 17. CAN and source locations in Tank 5



RI-18954

Figure 18. Top view of CAN

All instruments in the tank, but outside the CAN, were connected to their monitoring displays by shielded cable. Connections between the CAN sensors and the operator were made by fiber optic link, with the exception of the grounding strap.

A summary of sensors, connections and displays are given in Table 2.

The only measurement not common to the three dielectric samples was that of two Tektronix CT-2 current probes that monitored the charge flow from the back plane of the simulated solar array as shown in Figure 12.

3.3 ENVIRONMENTAL SIMULATION

One objective of this investigation was to determine the response of a simple conducting object to the effects of electron-induced discharge. This could be achieved by illuminating the model with electrons of sufficient energy. A secondary aim, in studying some of the charging conduct of dielectric samples, and the desire to more closely reproduce geospace charging conditions, suggested the inclusion of other

ORIGINAL PAGE
BLACK AND WHITE PHOTOGRAPH

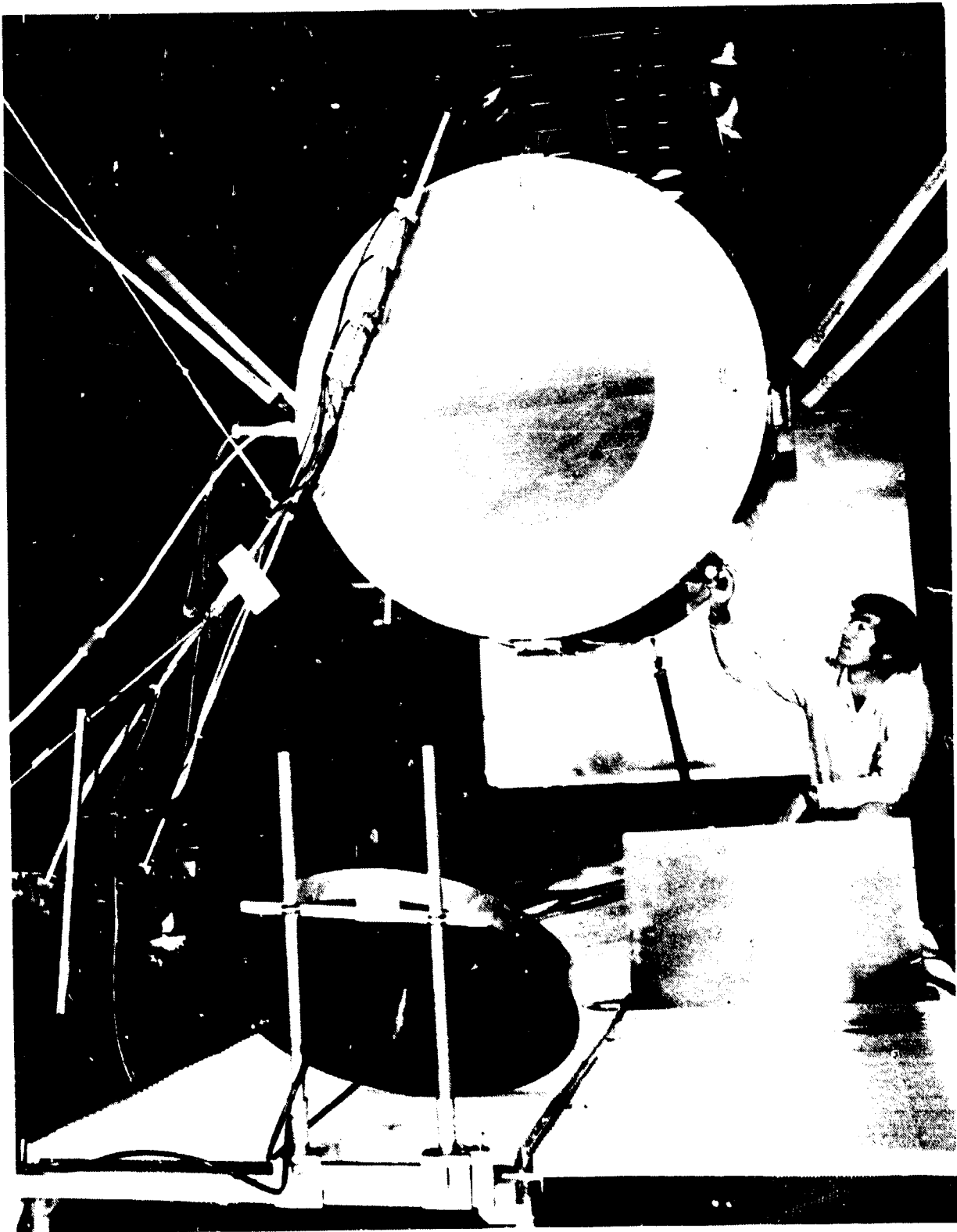


Figure 19. Front of test object showing probe arm

ORIGINAL PAGE
BLACK AND WHITE PHOTOGRAPH

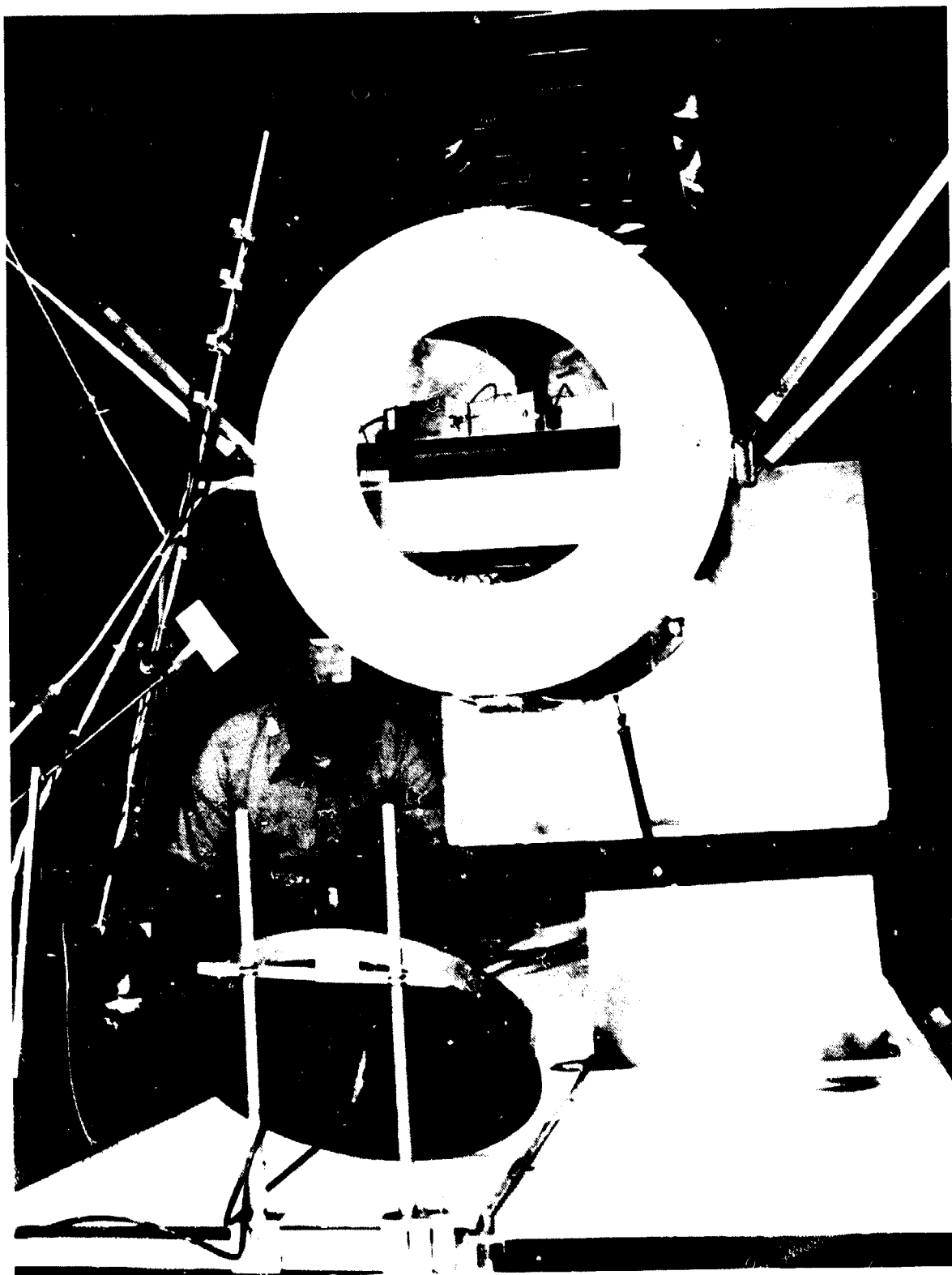


Figure 20. Internal electronics

Table 2. CAN Response Measurements

Sensor	Measurement	Connection	Display	No. of Simultaneous Measurements Possible
TREK Probe	Front surface potential map	Shielded cable	Strip chart	4
EG&G B sensor CMLX3B	Front surface currents	Fiber optic	Tektronix 7844 Oscilloscope	3 of 4
EG&G B sensor CMLX6, CMLX3	Side body currents	Fiber optic	Tektronix 7904, 7844 Oscilloscopes	3
Singer 91550-2 current probe	Ground strap discharge return current	Shielded cable	Tektronix 7834 Oscilloscope, Biomation 6500	1
Electrometer	Charging current in ground strap	Shielded cable	Strip chart, electrometer ammeter	1
Staring Camera	Sample discharge behavior		Film	1
Faraday Cup	Blowoff charge	Shielded cable	Biomation 8100, 6500, Tektronix 7704	1
CT-2 Current	Solar array back plane current	Fiber optic	Tektronix 7000 Series Oscilloscopes	2
203F VUV Photodiode	UV irradiation	Insulated wire	Electrometer-Voltmeter	1
Faraday Cups	Charging current density	Insulated wire	Strip chart, Electrometer-Voltmeter	4

radiation sources. Therefore, some effort was made to provide a more realistic simulation of the charging environment.

Four NASA/LeRC electron guns were mounted in the west end-cap of Tank 5, sufficiently distant from the front face that their relatively narrow beams ($\leq 12^\circ$) could deliver a uniform flux up to 5 na/cm^2 . This is at least an order of magnitude greater than the current densities encountered in the most severe substorm environment.

Excess negative charge is normally relieved on a satellite by UV stimulated photoemission and photoconduction. This is usually simulated in the laboratory by sources that seek to reproduce the quasi-blackbody emission of the sun. This has two drawbacks. Most of the spectral output is at photon energies less than the work

functions of the materials so that this radiation merely serves to heat the models. Second, such sources do not reproduce the solar vacuum ultra-violet line emissions which are responsible for much of the surface photoelectron emission from spacecraft. In fact, unless the chamber port and source window materials are suitably chosen, their short wavelength cutoffs will prevent the most effective part of the spectrum from being used.

Figure 1 shows the solar differential spectral irradiance at the earth. Radiation in different regions of the spectrum is dominated by emission at various depths in the sun. Although the continuum is normally represented as blackbody radiation, its characteristic temperature (T_b) is dependent on the wavelength range of the measurements. The net effect of radial thermal gradients in the sun and the increase of absorption cross section with frequency is that the brightness temperature increases with wavelength from the VUV to the near IR. In our range of interest (1000 to 3000 Å) T_b varies from ~5000 to 6000 K with a minimum value of ~4200 K at 1600 Å.

The emission intensities vary slowly during the eleven-year period and undergo rapid fluctuation near solar maximum. It is especially noticeable at energies above the continuum where H Ly α (1216 Å) can vary by at least a factor of three. At times of flare activity orders-of-magnitude variations occur in the EUV and soft x-ray regions of the spectrum.

Radiation below 3000 Å is that responsible for photoelectric and photoconductive effects. Detail of the range 1000 to 3000 Å is shown in Figure 21. It can be seen that line emissions are imposed on the smooth continuum, and that the first dominant line occurs at Ly α whose intensity is not matched by the blackbody radiation until the wavelength exceeds about 1800 Å.

The work functions of spacecraft conducting and semiconducting materials lie in the range 4 to 5 eV. Frictional charging measurements on the common organic dielectrics indicate that they can have similar values. Common satellite inorganic insulators have higher work functions in the range 8 to 12 eV. Solar array materials such as fused silica and magnesium fluoride are transparent in the middle UV and will not begin to respond until the photon wavelength is less than their absorption edges. The insert of Figure 21 shows their transmissivity dependences.

The interplay of variable solar photon output and different material photoelectric and photoconductive properties makes response prediction difficult. Lack of knowledge about some germane material parameters makes it worse. To complicate the problem further there are variations in the photoelectric response efficiencies with

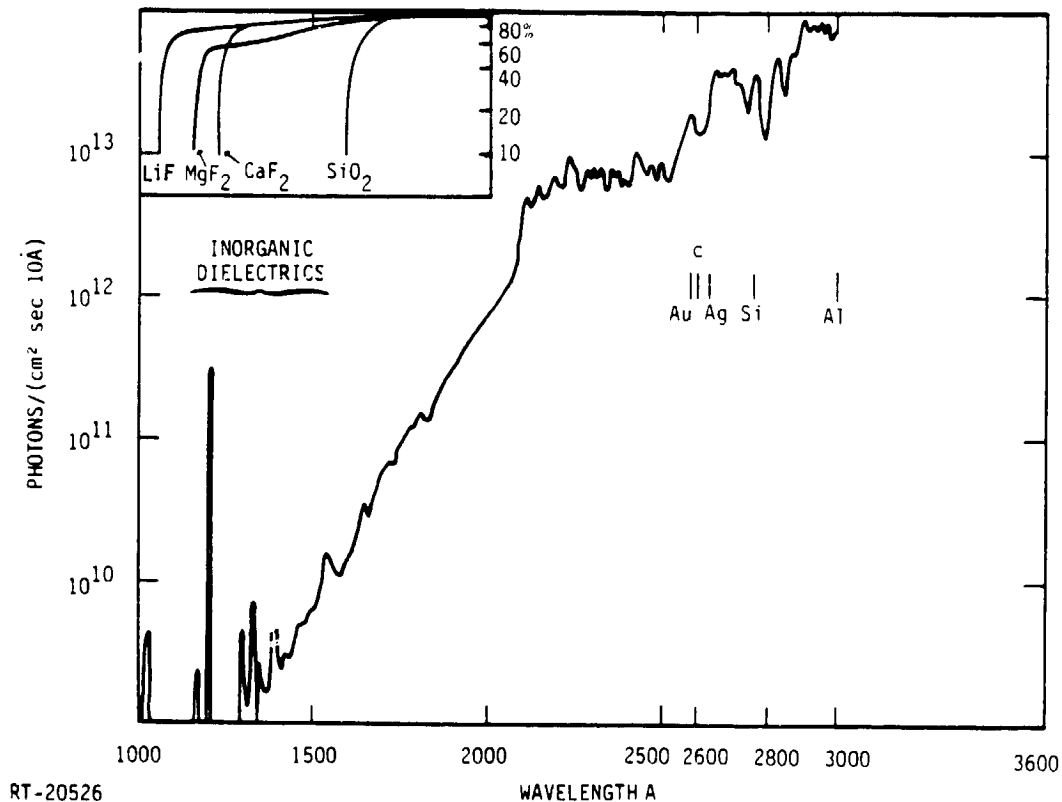


Figure 21. Solar UV spectrum

photon wavelength. In Reference 40 the matter was investigated for some normal spacecraft substances. Figure 22 reproduces, as an example, the dependence of the response of aluminum on photon energy. There is an extremely steep variation of efficiency at wavelengths greater than 1000 Å. At 1800 Å the efficiency is only 0.003 percent despite the fact that the 6.9 eV photon is well above the 4 eV work function.

Estimated flux under mean solar irradiation, ignoring line emissions at stationary orbit for aluminum, is shown in Figure 23. Major stimulation occurs in the solar output regions around 3000 Å and 2000 Å (continuum plus resonance lines), 1200 Å (structure other than Ly α) and 700 Å (maximum plus photoelectric efficiency). Simulation with a continuum source has some disadvantages. It produces some unwanted side effects such as heating of the test object. It has no emission below 1600 Å and therefore cannot stimulate photoelectron emission in inorganic dielectrics. Calculations involving flux integration are not possible unless its differential intensity is well known, and even then

ORIGINAL PAGE IS
OF POOR QUALITY

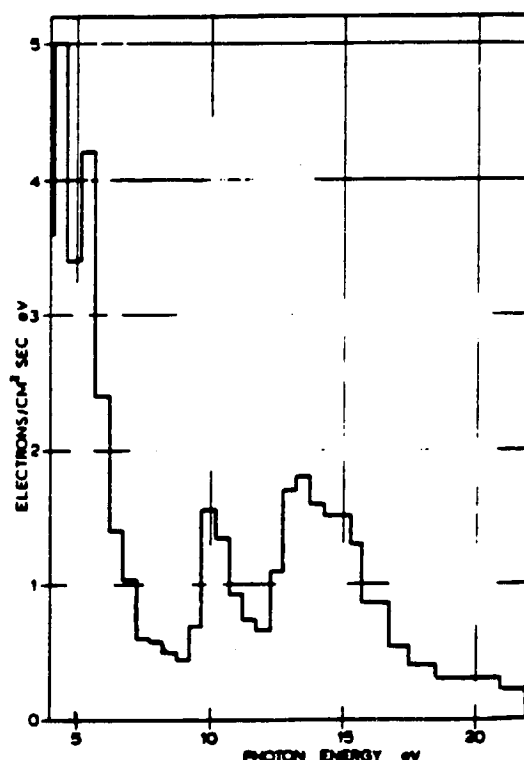


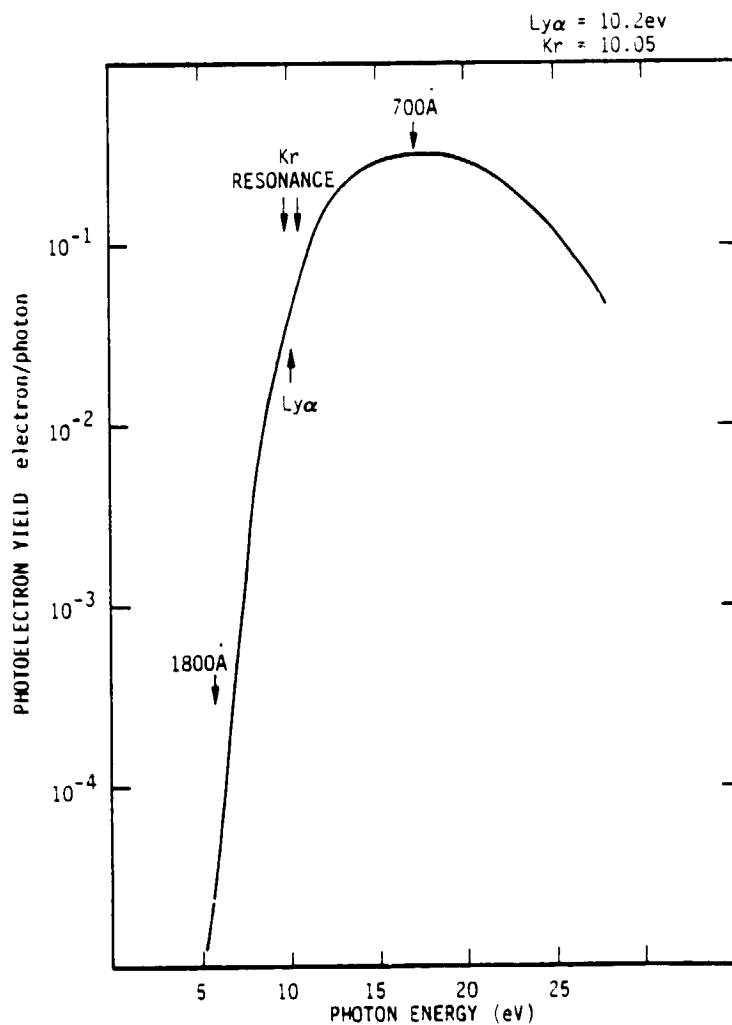
Figure 22. Differential flux of photoelectrons from aluminum due to solar irradiation

is very tedious. Reproduction of the short wavelength region below 1000 \AA is extremely difficult, especially for illumination of an object as large as the CAN.

Hence it was decided to attempt photon stimulation with low pressure Krypton vacuum UV sources. These emit the two resonance lines at 1165 \AA and 1236 \AA with a reputed maximum output of 3×10^{15} photons/s for the lamp chosen. At these wavelengths the photoelectric efficiency of aluminum is 6 percent. Table 3 summarizes the predicted responses of the CAN assuming that all photons fall on the front face of the sample and that the emission efficiencies for Kapton and Teflon are also 6 percent. However, good photoemission data at these wavelengths is required for accurate charging predictions.

Integration of Figure 23 and addition of the response to H Ly α yields a photoelectric current density for aluminum of 4.8 na/cm^2 of which 29 percent is due to Ly α . Considering these values and the previous arguments it is felt that irradiation with a vacuum ultra-violet source of sufficient intensity alone is convenient and adequate.

ORIGINAL PROFILE
OF POOR QUALITY



RT-20525

Figure 23. Photoelectric efficiency of aluminum

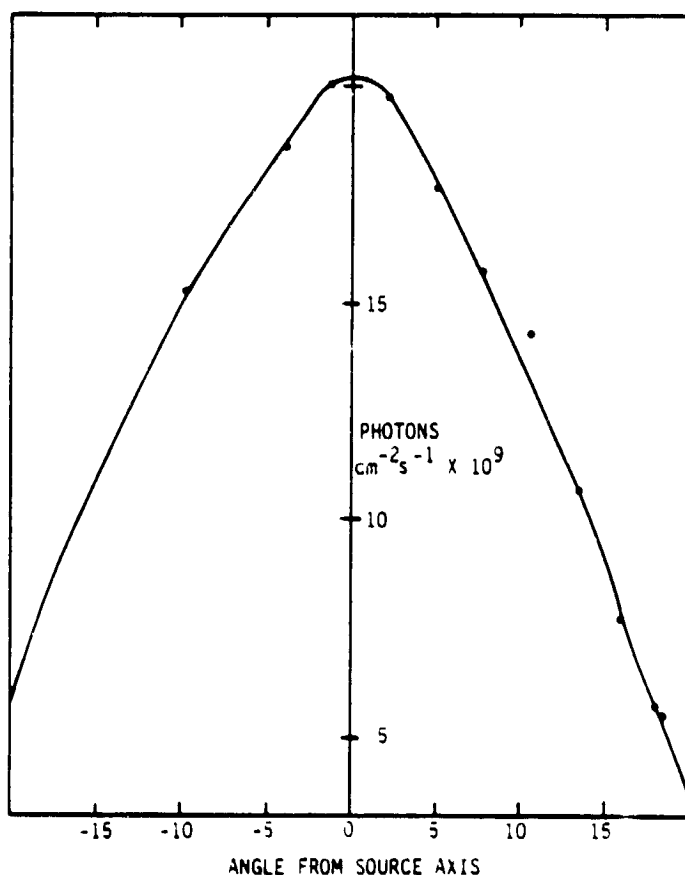
Table 3. Photoelectric Current Densities for Irradiation by the Krypton Resonance Lines

Illuminated Region Receiving 3×10^{15} photons/s	Area cm^2	Photoelectric Current at 6% Efficiency
		na/cm^2
CAN front face	14,500	2
Teflon or Kapton sample	4,400	6.5
Solar array (no response from MgF_2 surfaces)	1,250	~1.1

ORIGINAL PAGE IS
OF POOR QUALITY

A 13 mm and a 22 mm diameter MgF_2 output window low pressure Krypton source were obtained from Opthos Instrument Company. Their respective nominal outputs are 10^{15} and 3×10^{15} photons/s. Either could be mounted through the center of the end-cap and driven with a tunable Evensen cavity excited at 2.45 GHz.

The necessity of mounting the lamp 470 cm away from the front face resulted in a subtention by the CAN of only ± 8 degrees. Figure 24 shows a mapping of the UV flux by the photodiode on the probe arm which has a FWHM of ± 14 degrees. The result was that with the 13 mm lamp the total photon flux on the face was only $2.4 \times 10^{14} \text{ s}^{-1}$ yielding an average response current density of 0.16 na/cm^2 . Use of this lamp enabled relief only of low charging current fluxes. The larger lamp was unfortunately cracked during checkout and is not usable.



RT20699

Figure 24. Measured angular variation of VUV source

3.4 TANK OPERATION

It is wise that experiments of this nature be conducted at the lowest attainable pressures. The electron, ion and VUV photon flux intensities are very sensitive to variations in pressure even under common vacuum conditions. For example, Figure 25 shows a measurement of the dependence of electron current density from one of the NASA guns with pressure. It can be seen that, especially below $P = 10^{-5}$ torr, the efficiency of illumination increases rapidly with evacuation.

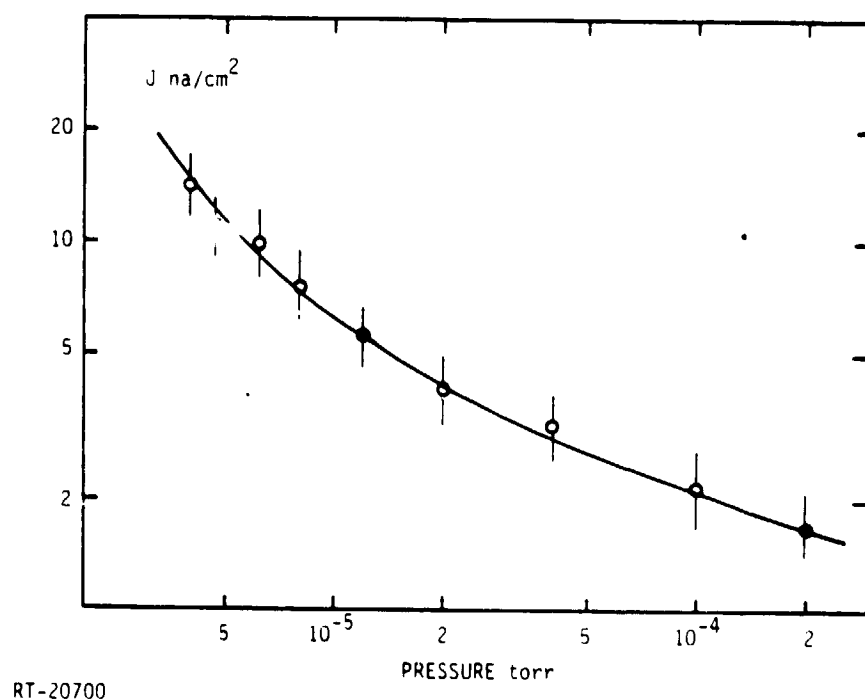


Figure 25. Variation of electron beam current density with pressure

Another observation, made in a very empirical manner, concerned the nature of the discharge data obtainable. The samples relieved their charged condition by both blowoff and flashover types of discharge. Kapton, which attained the highest potentials, was a rich source of blowoff data. However, at pressures above about 5×10^{-6} torr, it became very difficult to attain sample potentials resulting in such discharges. The flashover transients, moreover, decreased significantly in magnitude. It was not a result of lower electron flux densities because these could be adjusted to give constant currents at the sample. It appeared that the accumulating charge on the dielectrics was being bled away, in all likelihood, by increased surface interaction with the ambient chamber gas.

A first-order consideration indicates that this explanation is reasonable. Assuming the air to have a mean molecular mass of 28.8 and a constant RMS particle velocity (rather than a Maxwellian distribution), then at 0°C, the collision rate of molecules with a flat surface, dN/dt , is given approximately by

$$\frac{dN}{dt} = 3.2 \times 10^{20} P \text{ cm}^{-2} \text{ s}^{-1} \quad (2)$$

where P = pressure in torr.

At $P = 5 \times 10^{-6}$ torr a rate of 1.6×10^{15} collision/cm² s may be expected. A charging current density of 10 na/cm² is an electron flux density of about 6×10^{10} cm⁻² s⁻¹. Even assuming fully efficient attachment to the sample, the air molecule bombardment far exceeds the electron build-up rate.

Discharging by this means is probably due mostly to dislodging of electrons embedded in the surface layers, which then may be expelled by the negative potential. The mean energy of the molecules is about 0.04 eV which is probably not enough to free many surface electrons. The high velocity tail of the distribution may have sufficient population to affect the observed behavior.

The formation of negative ions of the atmospheric species could play a small part. The electron affinity of N₂ is very low (Ref 41). N₂⁻ has a short lifetime which is of the order of a few vibration periods. O₂, however, has an affinity of 0.45 eV and thus may play a role through capture of loosely attached electrons.

The attainment of sufficiently low pressures in Tank 5 is strongly dependent on the degree of liquid nitrogen flow and equilibrium temperatures of the two baffles. The necessity of CAN electrical isolation required the power for internal systems to be supplied by rechargeable nickel-cadmium batteries. These and certain electronic devices used could suffer performance degradation at temperatures below -10°C and it was necessary to maintain the test object above this value. This was achieved by using the lower nitrogen baffle only and controlling flow by means of thermostats on this cold wall. It was possible to keep the CAN warm and pressures sufficiently low by this procedure. For the SCATSAT testing it was decided to diminish the sensitivity of the data system electronics inside the tank by using only MIL STD components capable of operating at temperatures as low as -50°C.

PRECEDING PAGE BLANK NOT FILMED

4. PRESENTATION OF DATA

4.1 INTRODUCTION

In this section we present a qualitative review of representative discharge data which characterized the response of the CAN to discharges occurring in the three dielectrics, Kapton, FEP Teflon and the fused silica coverslips mounted on the solar array mockup. Sample configurations are described in Section 3.1, and measurement techniques in Section 3.2. The data selected for discussion represents a small fraction of all events recorded, being those with the largest amplitude. In fact, discharge pulses and corresponding responses of up to the largest reported were observed. However, in deriving a worst case for simulation, it is the largest discharges which are significant, as they will couple the most energy into internal cabling.

For each discharge, we attempted to simultaneously record the return current signal, a portion of blown-off charge collected by the large Faraday cup facing the front of the sample, and up to three \dot{B} sensor responses. The limiting factor in recording fast transient data was the number of working fiber optic links. No more than three were operational at any one time. In addition, several TREK probe sweeps were made for each sample and charging condition to obtain dielectric potential distributions before and after discharges to estimate the total amount of charge involved in representative discharges.

The \dot{B} sensors were used to determine the rate of change of surface replacement currents induced by a discharge. If one assumes that the aluminum surface of the CAN is a nearly perfect conductor, then the rate of change of the tangential magnetic induction field \dot{B}_t is related to surface current J_s in A/m by the relationship

$$\dot{B}_t = \mu_0 \dot{H}_t = \mu_0 \dot{J}_s, \quad (3)$$

where $\mu_0 = (4\pi \cdot 10^{-7})$. Note that B_t and J_s must be perpendicular to each other, i.e., B_θ on the top of the CAN measures J_r , while B_θ on the sides measures J_z in cylindrical

coordinates. The placement type and number of the \dot{B} sensors are shown in Figure 13. The CAN was hung so that Sensor 1 and Sensors 5, 6, and 7 were on the top of the CAN. Sensor output in volts was converted to an equivalent \dot{B} using the relationship

$$V_{OUT} = \dot{B} A_{eq} \quad (4)$$

where A_{eq} is the equivalent area of the sensor, which is basically a half cylinder. $A_{eq} = 5 \times 10^{-4} \text{ m}^2$ for the CML X3 and CML 3 sensors and $5 \times 10^{-3} \text{ m}^2$ for the CML X6 sensors. A more detailed discussion of the \dot{B} sensors can be found in References 42 and 43. In converting the raw data shown in the photos, correction was made for signal amplification produced by the AFWL fiber optic links (approximately 26 dB), inserted attenuation (0-24 dB) to limit the amplitude of the signals input to the fiber optic links to <13 mV, and the attenuation of the baluns which converted the differential \dot{B} output into a single-ended signal (approximately 10 dB).

Several of the scope photo data sets for each discharge were digitized, Fourier transformed, and for the \dot{B} data, numerically integrated. This effort was not as successful as we had hoped as the contribution of the higher frequency components (>20 MHz) which appeared in much of the data was hard to evaluate because of poor definition in the scope photos. However, these analyses did provide confirmation of the hand-integrated \dot{B} data. The problems encountered in digitization underlined the difficulty in recording all of the fine detail of the \dot{B} data. As the experiment progressed, \dot{B} channels were typically recorded on dual beam scopes with one channel set at 500 ns/div to obtain the overall pulse structure, while the second channel displayed an expanded subset of the entire pulse run at 50 to 100 ns/div to show fine structure detail.

The replacement current running through the ground strap was read with a current probe with a sensitivity of 1 A/volt. Measurements were taken for two configurations. In one, the ground strap was connected directly through bus bar to the outside of the tank. The connection from inside to outside the tank was through a heavy duty, high voltage, vacuum feedthrough capable of withstanding >25 kV. In the second configuration, "high impedance," a 1 M Ω resistor was placed in series with the bus bar outside the tank. However, the current flowing through the braid leading to the resistor was often measured to be in excess of 1 A, implying a potential difference of 1 MV--clearly impossible! The resistor was dc tested throughout the measurements and displayed a value close to nominal. The most likely occurrence in retrospect was that a current path parallel to that of the resistor was created during discharge lowering the effective impedance to ground. This was inferred from the fact that the product of the

presumed resistance times current yielded an impossibly large voltage. The maximum possible potential difference between the CAN and ground is the charging voltage, typically 20 keV. For a 1 amp pulse, this implies an effective impedance as low as 20 k Ω . The purpose of the 1 M Ω resistor was to decouple the CAN from the tank during discharge, by providing an RC time constant long compared to pulse widths to simulate space conditions. As the capacitance C of the CAN to the tank is ca. 10^{-10} pF, the minimum RC would be $10^{-10} \cdot 2 \cdot 10^4 = 2 \mu\text{s}$, comparable to the pulse width. Thus, the high-impedance simulation was only partially successful. For the SCATSAT tests, the single 1 M Ω resistor was replaced by two strings of 100 each 20 k Ω resistors.

Repeated surface potential scans were taken with the TREK probe array for each sample and charging configuration to obtain potential maps during charge buildup and after discharge. The difference in average potential before and after a discharge is a measure of the total charge released. Typically, the probe arm would be repeatedly swept back and forth across the face of the sample for a period sufficient to record one or more discharge events. The sweep pattern for the sensors is shown in Figure 26. Barring rapid changes in potential because of discharge, successive profiles were mirror images of each other. As the surface potential data indicates, a profile sweep could be performed in less than 10 seconds. Charging times are greater than or equal to $\bar{V}_{so}/C_s I_i$, where \bar{V}_{so} is the equilibrium discharge potential, C_s sample capacitance and I_i incident current. For representative charging currents, ca. 2 na/cm², the time between major discharges is ~1 minute or more. Thus, the successive potential sweeps over ca. 10 seconds reproduced reasonably well the before and after surface potential maps.

4.2 KAPTON

The Kapton sample is shown in Figure 8. Figure 27 shows a time exposure of the same sample during an irradiation in which it underwent numerous discharges. Discharge foci are seen to be present both in the bulk material as well as along the edges of the region where the Kapton tape overlaps. In all cases examined, such edges were seen to be discharge foci. After prolonged exposure, numerous pinholes could be found in the tape. The charging conditions were $E_i = 20$ kV, $J_i = 2-3$ na/cm².

Figures 28 and 29 show surface potential scans for two charging conditions. The numbers on the side refer to the corresponding TREK probe paths shown in Figure 26. In the figures, one can also see that the region of tape overlap is one of high potential

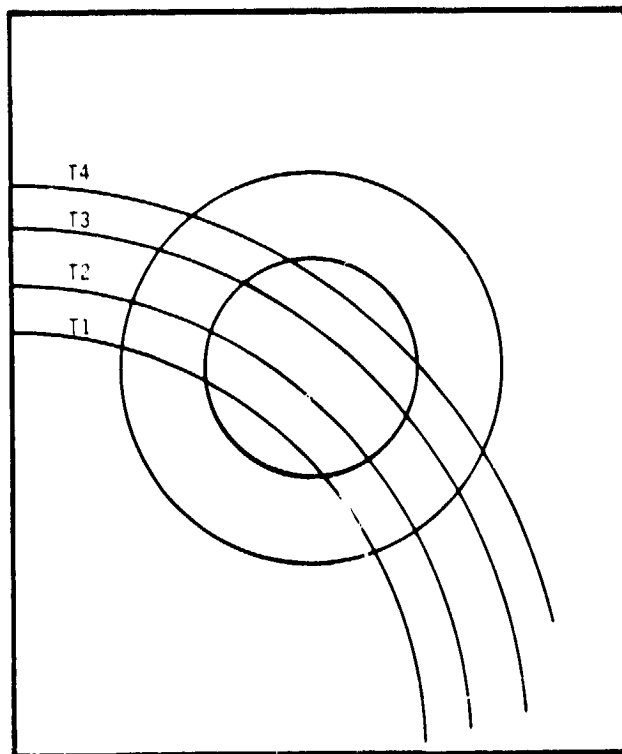


Figure 26. Path of TREK probes across the CAN front face. The inner circle shows the approximate region covered with dielectric during the tests.

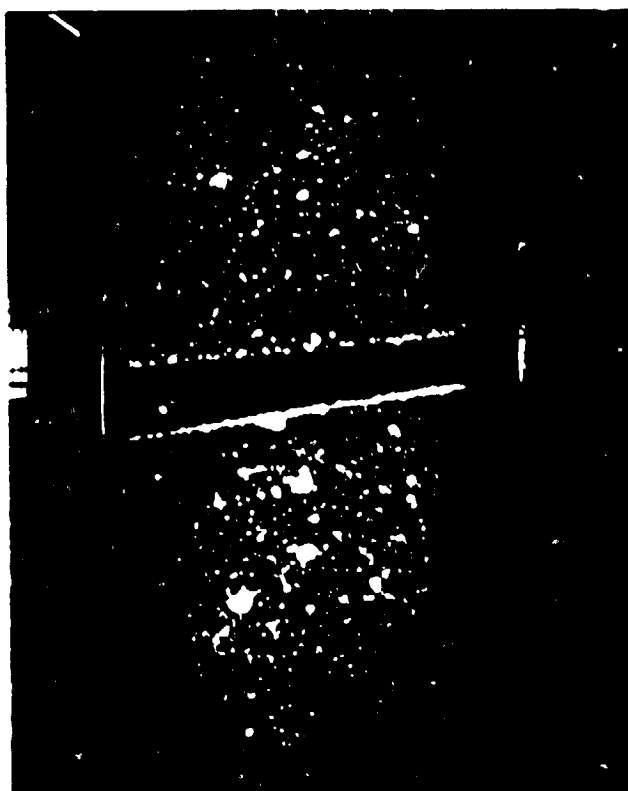
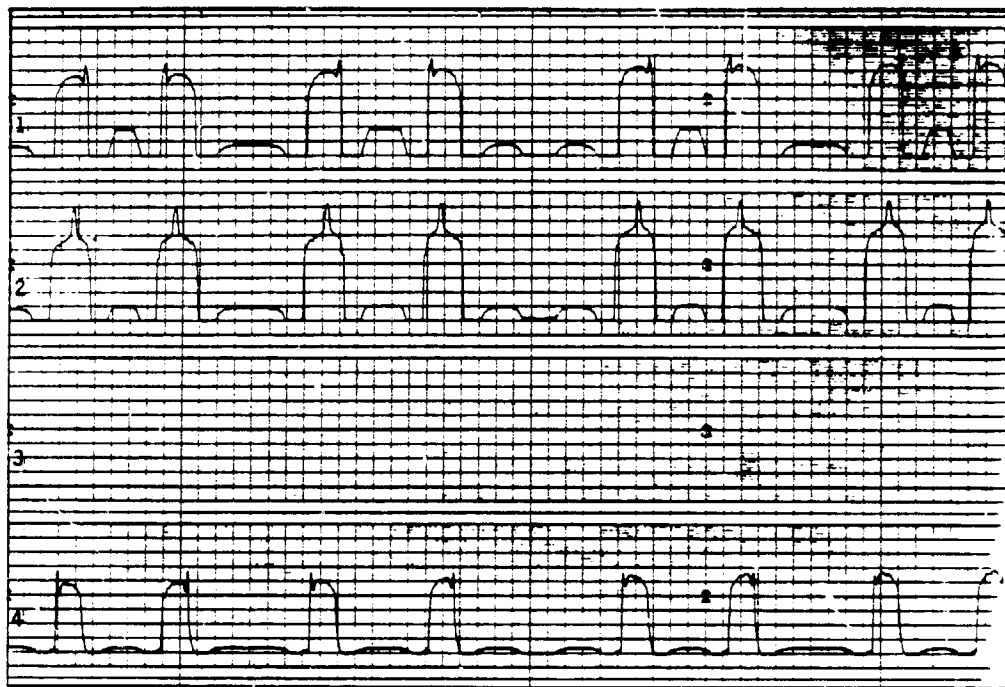
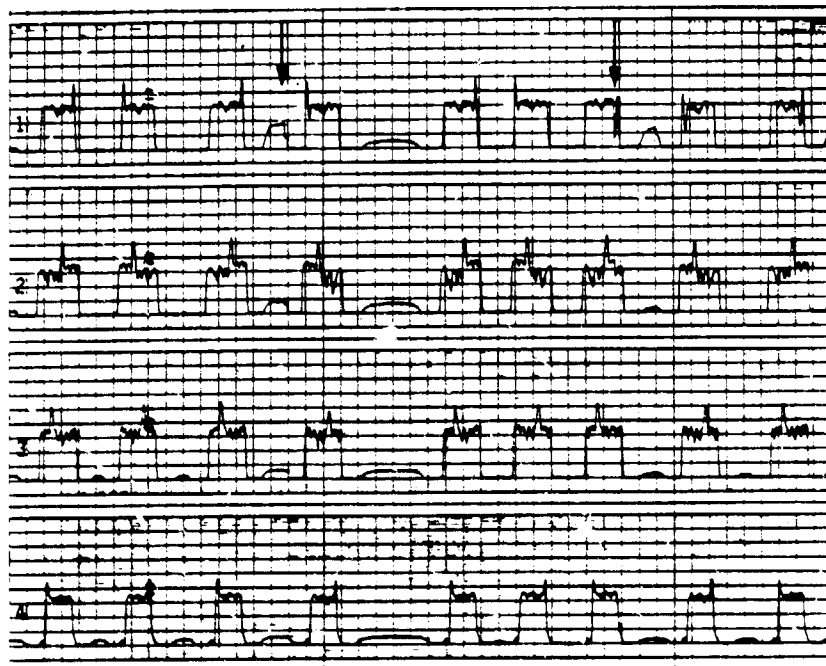


Figure 27. Discharges in Kapton sample



RT-20768

Figure 28. Surface potential map of Kapton, grounded configuration, $E_i = 10$ keV, $J_i = 2$ na/cm². Horizontal: 2.5 sec/div; Vertical: 1.5 kV/div. The spikes correspond to the region of Kapton tape overlap; i.e., double thickness as shown in Figure 27.



RT-20767

Figure 29. Surface potential map of Kapton, grounded configuration, $E_i = 15$ keV, $J_i = 2$ na/cm². Horizontal: 2.5 sec/div; Vertical: 2.5 kV/div. The horizontal arrows indicate the occurrence of discharges.

(relative to the CAN at tank ground) and one where there is a sharp potential gradient. Discharges at $E_i = 15$ keV, indicated by the arrow are relatively localized rather than removing charge from across the sample. This is an important point, namely that configuration effects such as seams or edges in segmented samples may induce discharges at lower average potentials and over a more limited area than might be expected from results based on testing of uniform samples and may limit the applicability of scaling laws.

Table 4 summarizes typical average and peak surface potential and stored charge data for the various samples before and after discharge. \bar{V}_{so} is the average dielectric surface potential before discharge, V_{max} the maximum, and \bar{V}_{sd} the average potential after discharge. The mean surface charge density before discharge $q_0 = C\bar{V}_{so}$. The charge lost in the discharges is Δq . The total fraction of stored charge removed by blowoff, flashover, and punchthrough in the discharge is f . The data indicates that the equilibrium charging potentials are relatively independent of the impedance as expected since charging is effectively a DC process. The ΔQ data, for Teflon at least, indicates that the total amount of charge involved in a discharge is also relatively independent of CAN impedance. This assumption is also implicit in the data and models presented in References 35 and 37. Note that while the relative fraction of stored charge released in a discharge is significant for Teflon and also by inference from the B data for Kapton at $E_i = 20$ keV, it is usually relatively small for discharge of the fused silica coverslips mounted on the solar array mockup.

Table 4. Charging Behavior of Dielectric Samples

Material	Impedance	E_i (keV)	\bar{V}_{so} (kV)	V_{max} (kV)	\bar{V}_{sd} (kV)	q_0 ($\mu C/cm^2$)	ΔQ (μC)	f
Kapton	Low	10	5.4	8.2		0.47		
		15	8.2	13.5		0.72		
		20	9.0	15.0		0.79	467	0.11
FEP	Low	10	6.4	7.0		0.093		
		15	8.5	11.5	6.0	0.12	160	0.30
		20	13.3	16.0	2.7	0.19	678	0.81
	High	20	11.5	15.0	3.7	0.17	500	0.67
Solar Array	Low	20	10.8	12.0	8.3	0.36	129	0.23
	Large	20	10.3	12.0		0.34	22	0.04
	Typical	20	10.3	12.0				
	High	20	10.3	12.5				

Figures 30 and 31 are photographs of \dot{B} and blowoff current waveforms for discharges in Kapton with the CAN grounded. These photos are typical of the larger amplitude pulses created by discharges in this material. Their basic shape is consistent with a monopolar blowoff current source whose width is comparable to the \dot{B} pulse width and whose peak occurs at the crossover point of the B signal; i.e., at 1.3 to 1.8 μ s.

Figure 32 shows the structure of the hand-digitized blowoff pulse and its Fourier transform. Figure 33 shows a digitized \dot{B} sensor output and its integral converted to equivalent surface current using Equation 3. Note that most of the high frequency component evident in Figure 31 is lost in the digitization process. The amplitude of the integrated pulse is about 22 A/m, which corresponds to a net radial current of about 75 amps. The surface current pulses showed comparable amplitudes. If one takes this pulse as a lower bound on the magnitude of the blowoff source term, i.e., no space charge limiting of emission, then in excess of 100 μ C is involved in the blowoff discharge.

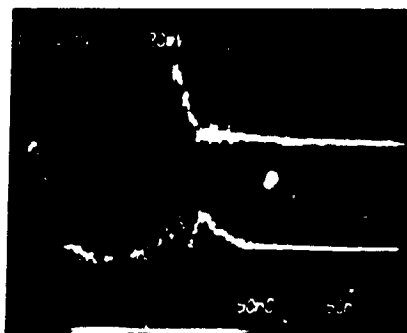
Representative peak \dot{H} amplitudes are plotted in Figure 34. Also plotted is a normalized rate of change of collected blowoff current = $I_B(\text{peak})/\pi D \tau_p$ where I_B is the peak blowoff current collected by the Faraday cup looking at the sample, D is the CAN diameter = 1.36 m, and τ_p is the time at which $I_B(\text{peak})$ is reached, measured from the pulse onset.

The net charge collected by the blowoff detector was about 1.2 μ C. A simple calculation based on the relative sizes and positions of the blowoff collector and CAN indicates that if the blowoff charge is emitted isotropically and travels towards the tank walls, then the Faraday cup should intercept about 1/80th of the total emitted charge. Thus, the blowoff data is consistent with that of the \dot{B} sensors.

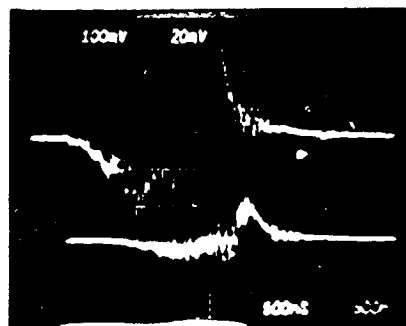
The high frequency component of the \dot{B} data was not resolvable. However, data taken during later runs indicates that this component has a frequency in excess of 50 MHz.

Figure 35 shows representative \dot{B} and blowoff sensor data for the response produced by discharges in Kapton for the high impedance configuration. The pulse shapes and amplitudes of the \dot{B} data are similar to those for the grounded case (see Figure 31). The shape of the observed blowoff pulse is significantly different. In the high impedance case, the observed blowoff pulse shapes were typically bipolar or multipolar (+,-). Integration of representative \dot{B} data yields peak surface currents of ca. 50 A/m on top of the CAN, or about 170 amps peak.

ORIGINAL PAGE IS
OF POOR QUALITY



a. Sensor 3 Upper: 7.0 T/sec/div
Lower: 34.8 T/sec/div
Both 500 ns/div



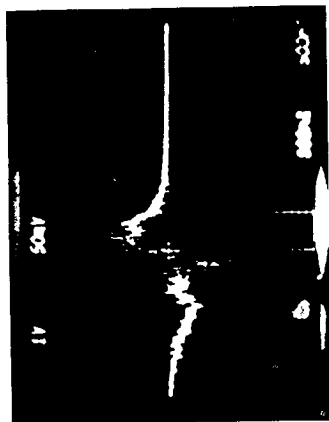
b. Sensor 1 Upper: 19.2 T/sec/div
Lower: 96 T/sec/div
Both 500 ns/div

Figure 30. Kapton, grounded configuration, \dot{B} sensor data

ORIGINAL PAGE IS
OF POOR QUALITY



a. Blowoff current, 0.2 A/div, 500 ns/div



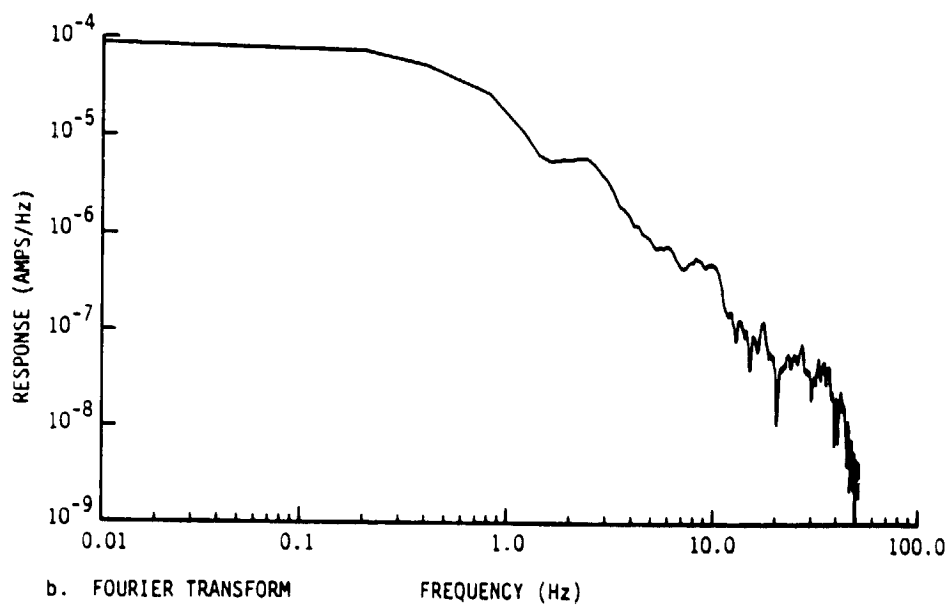
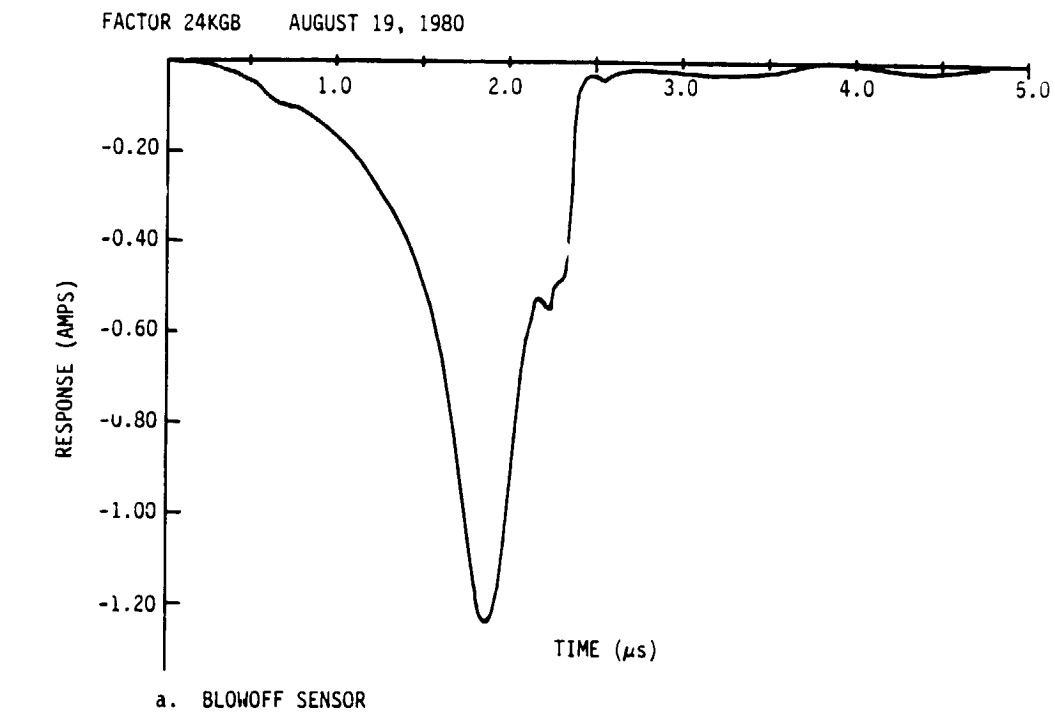
b. Sensor 1, 48 T/sec/div, 500 ns/div



c. Sensor 3, 56 T/sec/div, 500 ns/div

Figure 31. Kapton, grounded configuration, photographs of sensor data

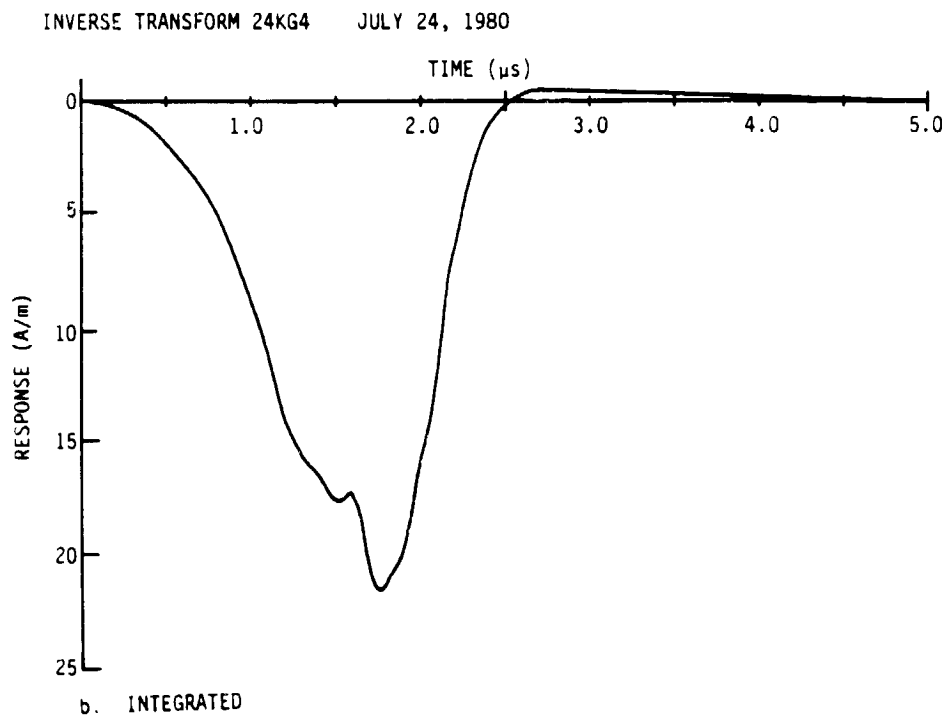
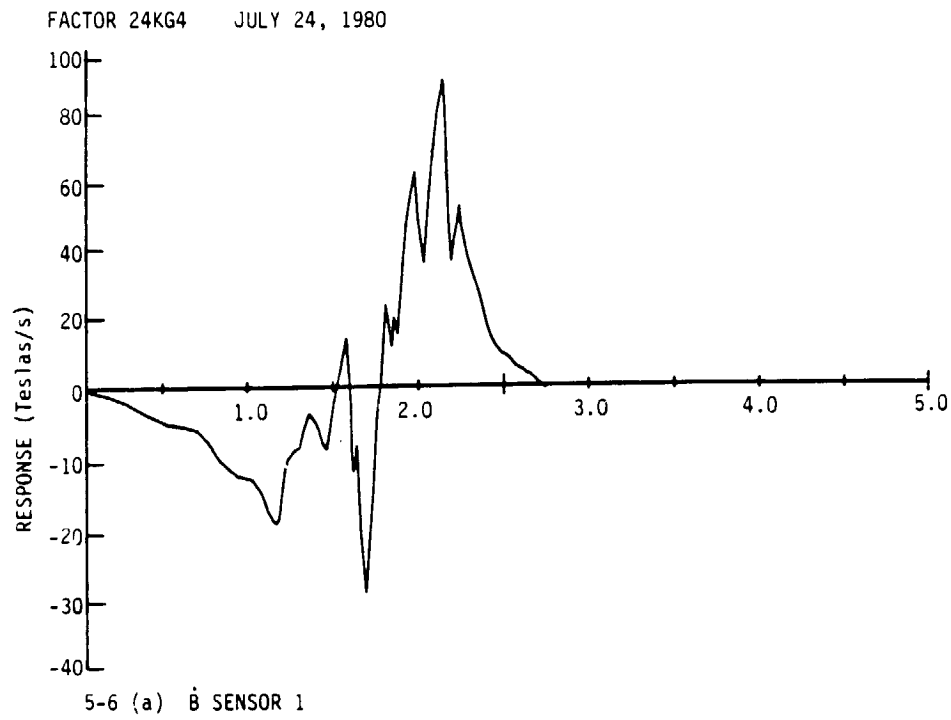
ORIGINAL PAGE IS
OF POOR QUALITY



RT-20752

Figure 32. Digitized blowoff current response for Kapton, grounded configuration

ORIGINAL RECORD
OF POOR QUALITY



RT-20750-A

Figure 33. Digitized \dot{B} sensor response for Kapton, grooved configuration

ORIGINAL PAGE IS
OF POOR QUALITY

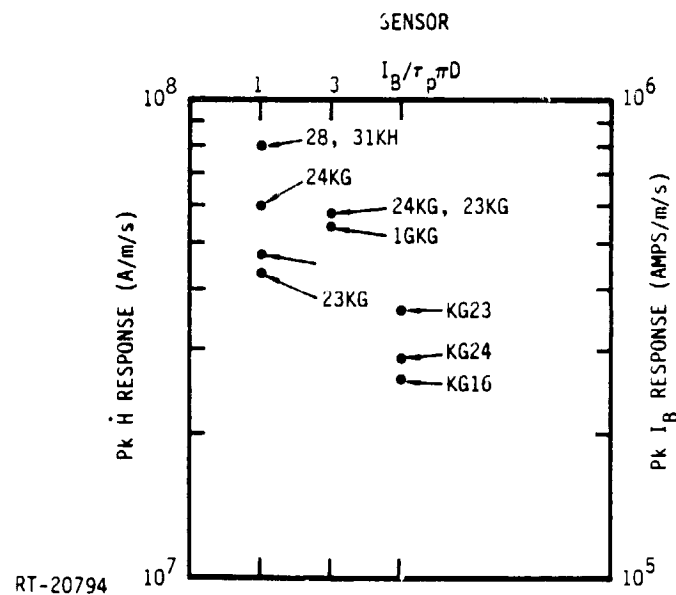
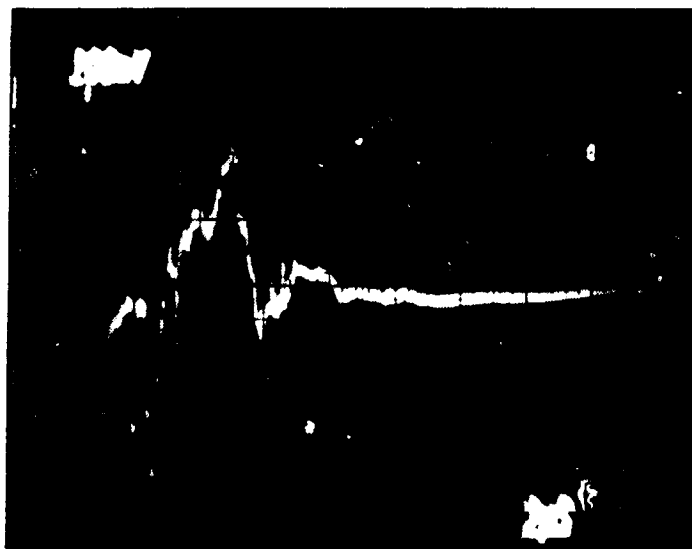
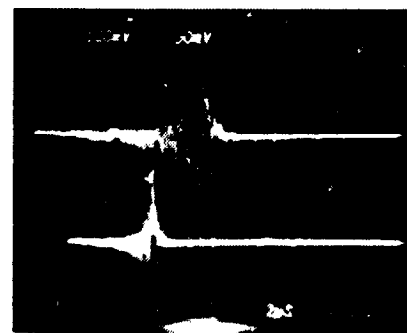


Figure 34. Kapton sensor response



- a. Blowoff
Vert: 20 ma/div
Horiz: 2 μ sec/div



- b. Sensor 1
Upper Vert: 49 T/sec/div;
Lower Vert: 97 T/sec/div
Upper Horiz: 1 μ sec/div;
Lower Horiz: 2 μ sec/div

Figure 35. Sensor data, Kapton, high-impedance configuration

4.3 TEFLON

The configuration of the Teflon sample panel is shown in Figure 9. As there was some question as to the effect of the manner of application of the tape on discharge initiation, the panel was made up with the bottom three seams butted and the top four lapped. The latter procedure was used in mounting this material on the P78-2. Figure 36 is a time exposure of the panel under electron irradiation. It can be seen that the discharge foci lie along the seams of the tape. It is not apparent from the photograph whether discharges are more prevalent along butted or lapped seams. However, there is some evidence to be obtained from the surface potential scans.

Figures 37 through 40 show the surface potential map for several sweeps of the CAN containing the TREK probes for $E_i = 10, 15, 20$ keV, $J_i = 2$ na/cm² for the CAN grounded and for $E_i = 20$ keV for the CAN in the high impedance configuration. Representative average, peak and post-discharge potentials, as well as charge lost in a discharge are shown in Table 4.

For $E_i = 10$ keV, there is little if any discharging of significant magnitude. The dip in potential at the seams is evident. For $E_i = 15$ keV, discharges which remove a significant fraction of the stored charge are evident as is the steeper potential gradients at the tape seams. These trends become more pronounced for $E_i = 20$ keV. The rate of discharge becomes more frequent and involves neutralization of most of the trapped charge. The charging and discharging behavior of the Teflon sample for both the grounded and high impedance configurations are similar.

In order to correlate structural features with discharge foci, the data of Figure 39 were replotted and superimposed on the Teflon surface in Figures 41 and 42. It can be seen that, as expected, the potential is highest on tape surfaces between seams. More charge was lost from the upper half plane of the sample in the discharge plotted. For Teflon irradiated at $E_i = 20$ keV, $J_i = 2.5$ na/cm², major discharges occur every minute or so.

Again, the time lapse photographs and surface potential scans show the fact that steep potential gradients occur at discontinuities in the dielectric, such as at edges or at seams which are regions of high potential gradients and serve as foci for discharge initiation. As many spacecraft insulators are put down in segments (solar arrays, OSR's, etc.) one must be careful about applying scaling laws based on the behavior of uniform seamless laboratory samples to real space hardware.

ORIGINAL PHOTOGRAPH
OF POOR QUALITY

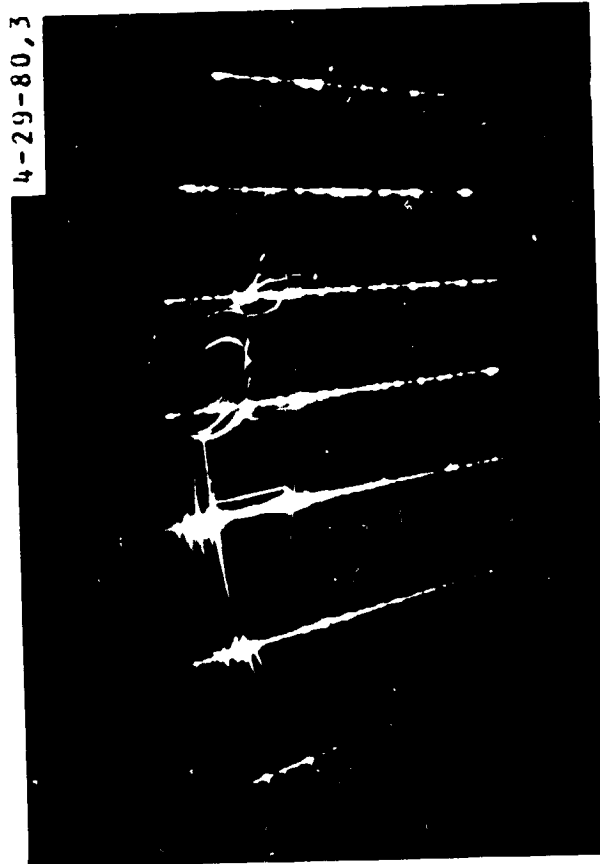
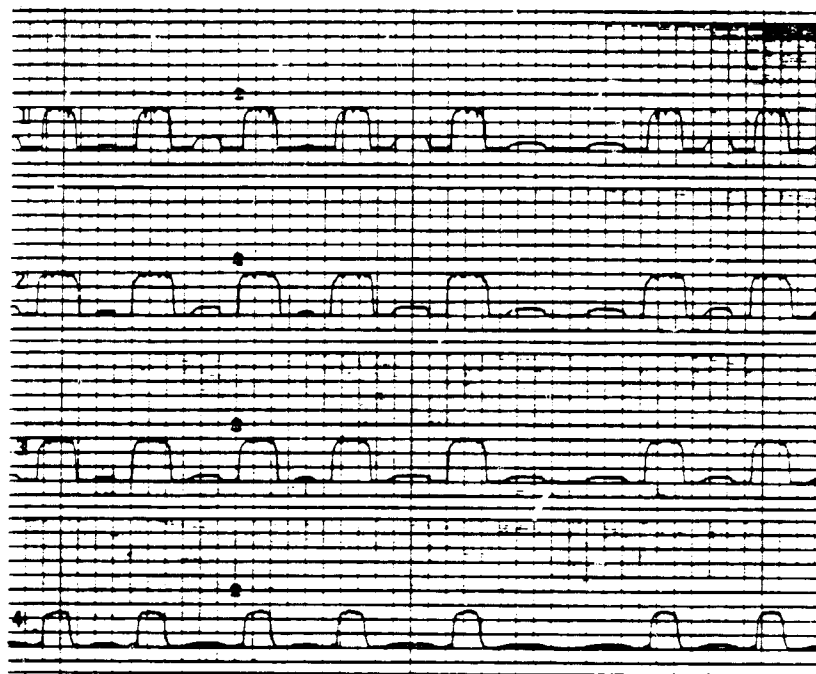
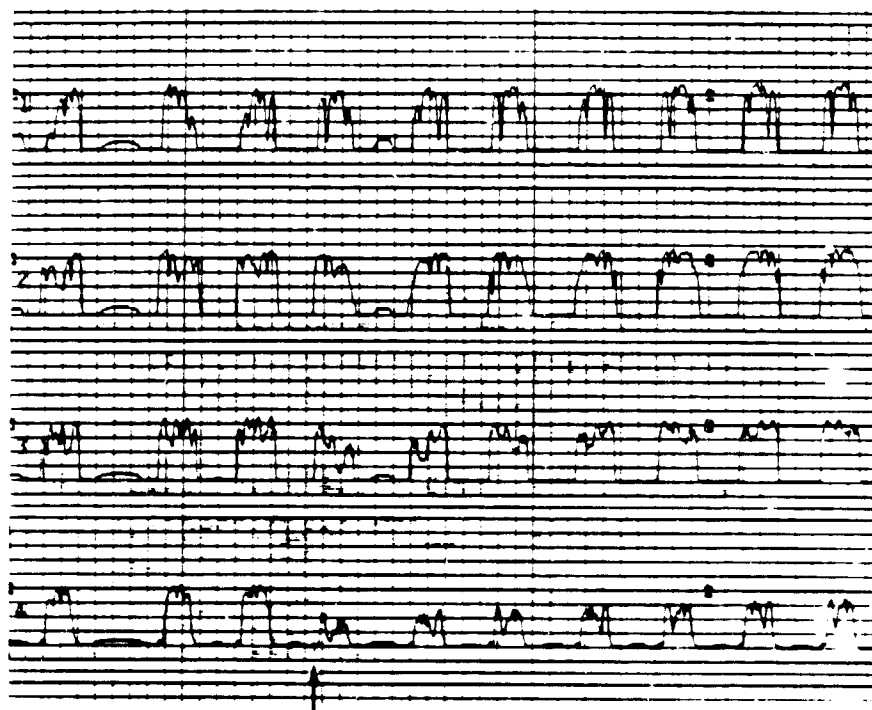


Figure 36. Discharges in the Teflon tape sample



RT-20766

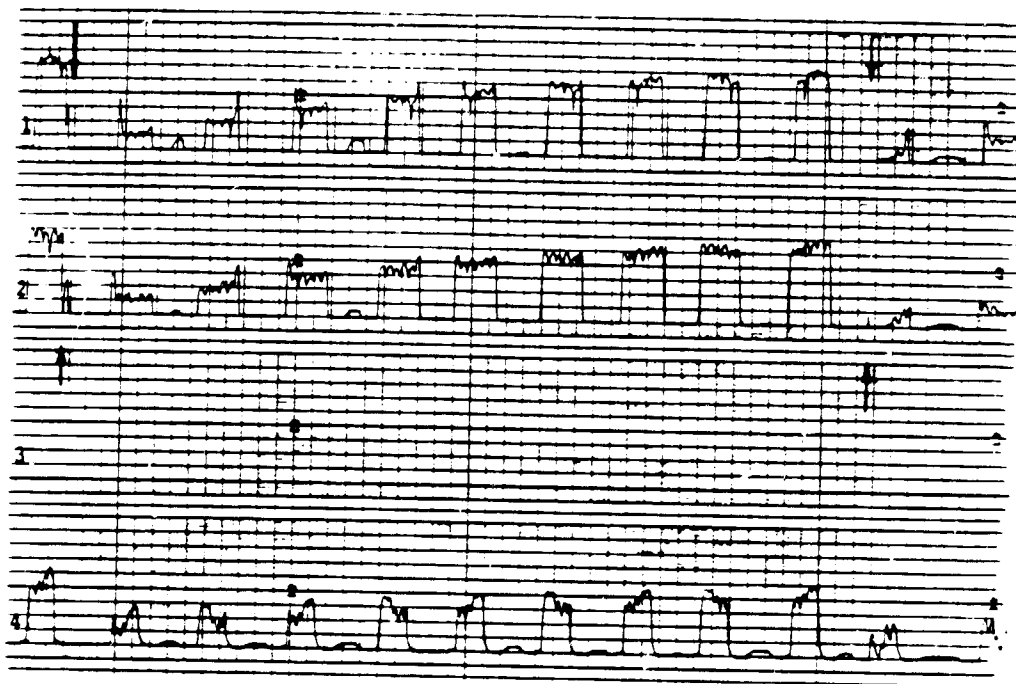
Figure 37. Surface potential map of FEP Teflon, grounded configuration, $E_i = 10$ keV, $J_i = 2$ na/cm². Horizontal: 1 box = 2.5 sec; Vertical: 1 box = 2.5 keV.



RT-20765

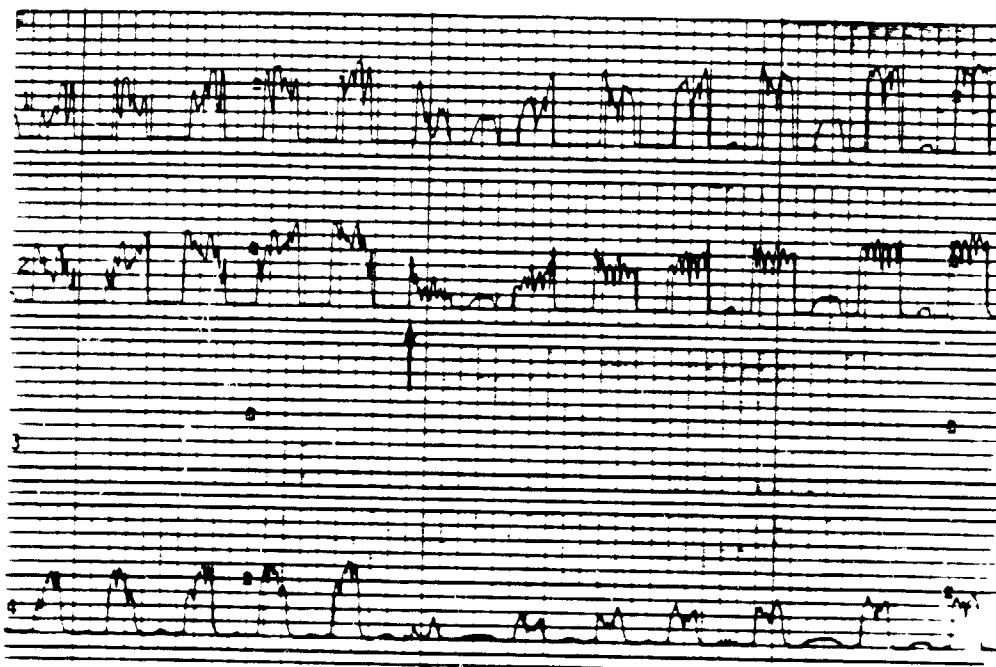
Figure 38. Surface potential map of FEP Teflon, grounded configuration, $E_i = 15$ keV, $J_i = 2$ na/cm². Horizontal: 1 box = 2.5 sec; Vertical: 1 box = 2.5 kV. The arrow indicates the occurrence of a discharge.

ORIGINAL PAGE IS
OF POOR QUALITY



RT-20764

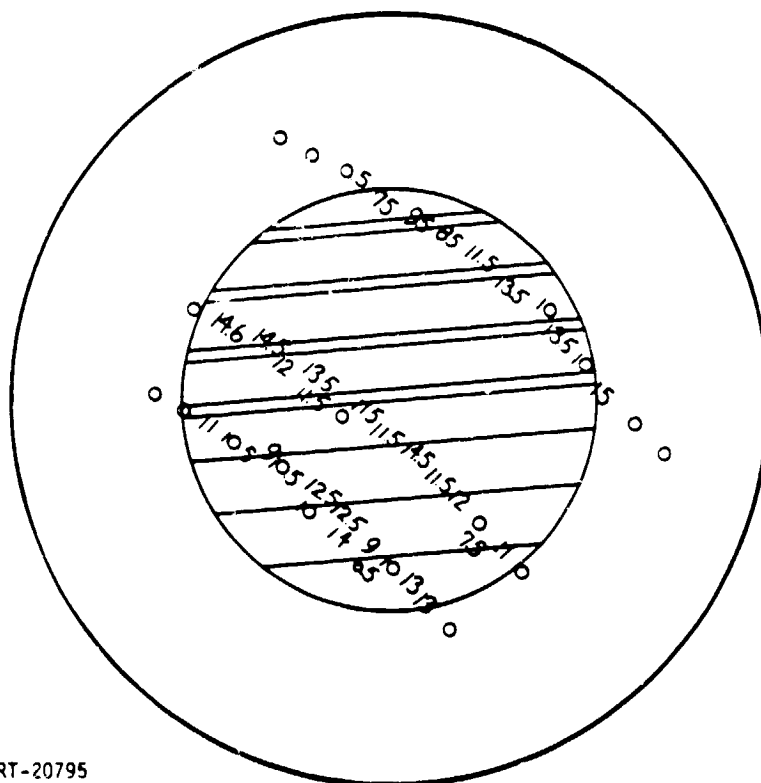
Figure 39. Surface potential scan, FEP Teflon, $E_i = 20$ keV, $J_i = 2.5$ nA/cm². Horizontal: 1 div = 2.5 sec; Vertical: 1 div = 2.5 kV. The arrows indicate the occurrence of discharges.



RT-20763

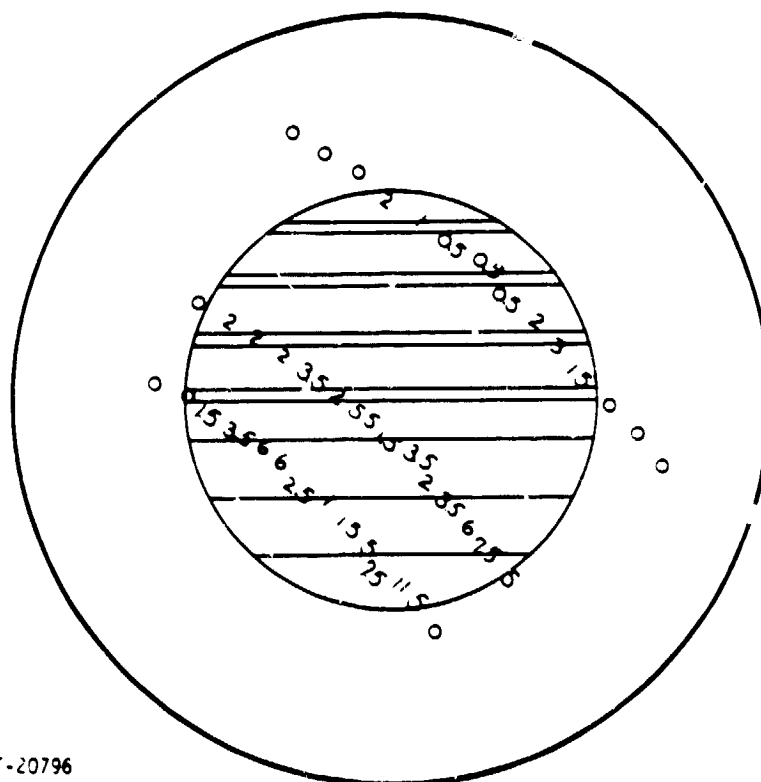
Figure 40. Surface potential scan, FEP Teflon, high impedance configuration, $E_i = 20$ keV, $J_i = 2.5$ nA/cm². Vertical: 1 div = 2.5 kV; Horizontal: 1 div = 2.5 sec. The arrow indicates the presence of a discharge.

ORIGINAL PAGE IS
OF POOR QUALITY



RT-20795

Figure 41. Surface potential map of Teflon, $E_i = 20$ keV, before discharge



RT-20796

Figure 42. Surface potential map of Teflon, $E_i = 20$ keV, after discharge

Figures 43 through 45 show representative photographs of the response produced on the grounded CAN by discharges in the Teflon. The return current photos are inverted as these pulses are actually positive, i.e., electron flow from ground to the CAN during discharge. The amplitude of these pulses ranged as high as 200 A peak. Pulse half maximum widths were 1.0 to 1.8 μ s. The amount of charge lost to blowoff can be bounded by the return current pulses as being at least 150 μ C or about 25 to 35 percent of the total charge removed in large amplitude discharges. The latter represented about 75 percent of the total charge stored for $E_i = 20$ keV, $J_i = 2.5$ na/cm² charging conditions.

The data of Figure 45 was digitized. The blowoff and return signals are shown in Figure 46, and \dot{B} data in Figures 47 and 48. The latter were numerically integrated as shown in the figures. Note that in the digitization process, information about the high frequency component is lost. However, it is clear that the basic pulse is relatively wide, ca. 1 to 2 μ s, much wider than that of the MIL-STD 1541 arc and the CDI pulse used in the CAN and SCATSAT electrical tests discussed in Reference 2.

The magnitude of the surface currents and return currents are comparable. For example, the surface current shown in Figure 48 averages to a net flow on the top of the CA. of 228 A peak. This is about twice as large as the return current. However, the surface potential data indicates that the discharge is asymmetric in that more current will flow on some areas of the CAN than others. In addition, the flow of surface body current and return current will be equal only in the case where all of the blowoff charge escapes to the walls of the tank. In most of the cases analyzed, the magnitude of the surface current at a sensor location was less than that for the return current. Estimated peak surface current data and corresponding return currents are shown in Figure 49. Peak $\dot{H}(= \dot{B}/\mu_0 = \dot{I}_s/\pi D)$ response is plotted in Figure 50.

The notation employed nnTa is nn = shot number, T = Teflon, a = G = grounded, a = H = high impedance configuration. It can be seen that the data for a particular sensor shows considerable fluctuation. This is due to the fluctuation in the pulse shape and amplitude of particular discharges which is magnified by the fact that a \dot{B} sensor produces a derivative of the corresponding current. In addition, the high impedance data as a group shows higher amplitudes than that of the grounded configuration data. This is due, in part, to the enhanced high frequency component in the high impedance discharge data. This can be understood by the following simple argument. The response of the \dot{B} sensor is given by Equation 4. If one has a pulse with several surface current



a. Sensor 1 Vert: 48.6 T/div
 Horiz: 500 ns/div



b. Upper - Blowoff 0.4 A/div
 Lower - Sensor 3 39.4 T/div
 Both 500 ns/div



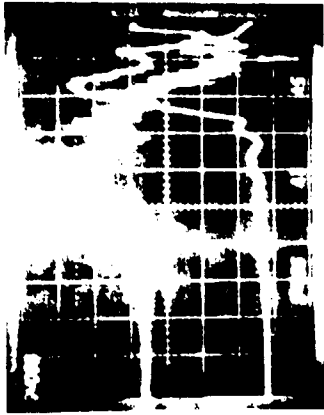
c. Return Vert: 20 A/div
 Horiz: 500 ns/div

Figure 43. FEP Teflon, sensor output, grounded configuration



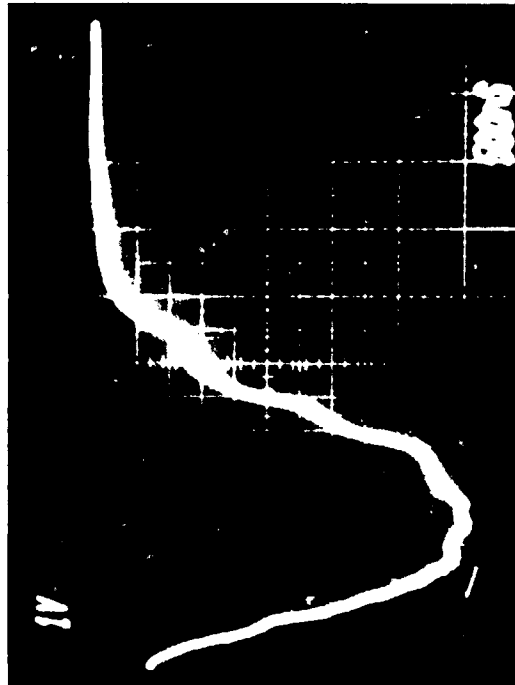
a. Sensor 8

Upper Vert: 38.4 T/sec/div
Lower Vert: 19.3 T/sec/div
Both 500 ns/div



b. Sensor 14

Upper: Blowoff, 0.4 A/div
Lower: Sensor 14, 12.8 T/sec/div
Both 500 ns/div



c. Return Vert: 20 A/div
Horiz: 500 ns/div

Figure 44. FEP Teflon, sensor data, grounded configuration



a. Sensor 4
Upper: 13 T/sec/div
Lower: 68.5 T/sec/div
Both 500 ns/div



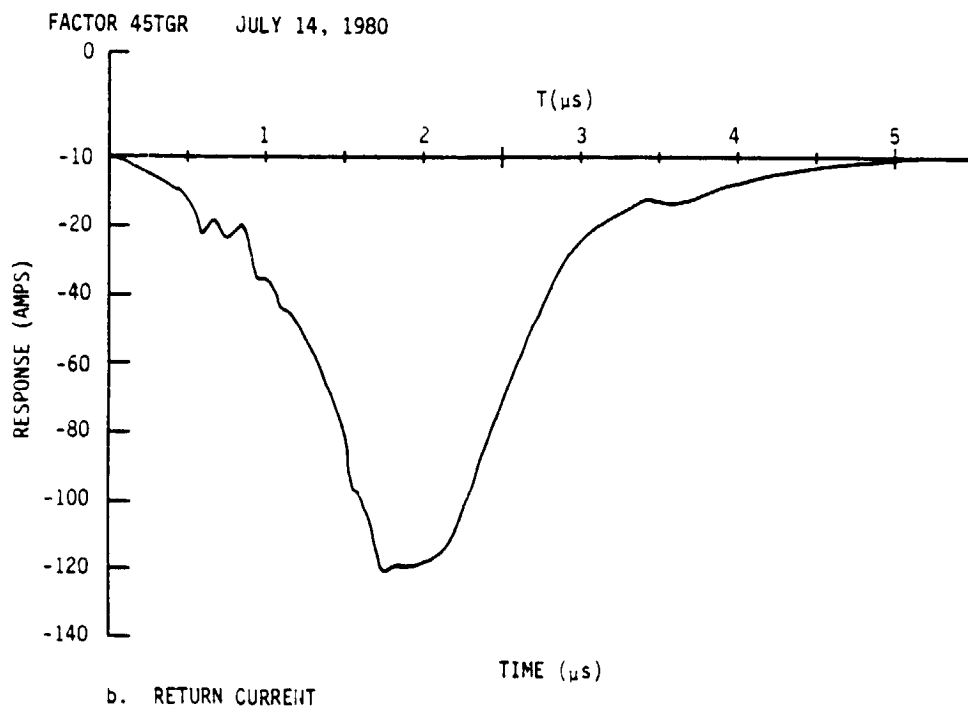
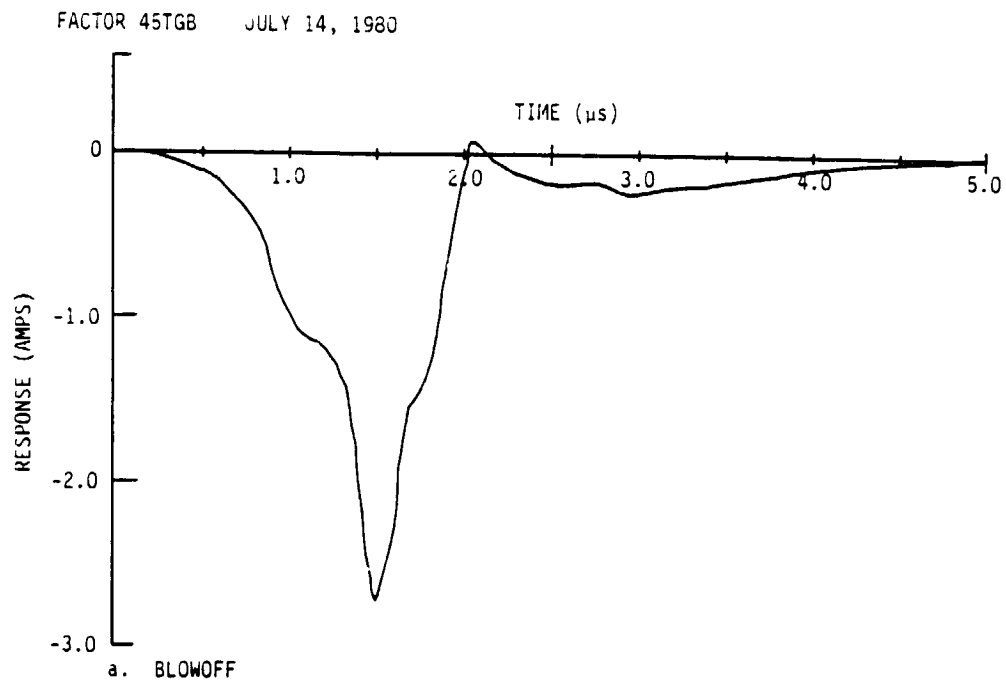
b. Upper: Blowoff, Vert: 0.4 A/div
Lower: Sensor 11, Vert: 22.4 T/sec/div
Both 500 ns/div



c. Return Current Vert: 20 A/div Horiz: 500 ns/div

Figure 45. FEP Teflon response, grounded configuration

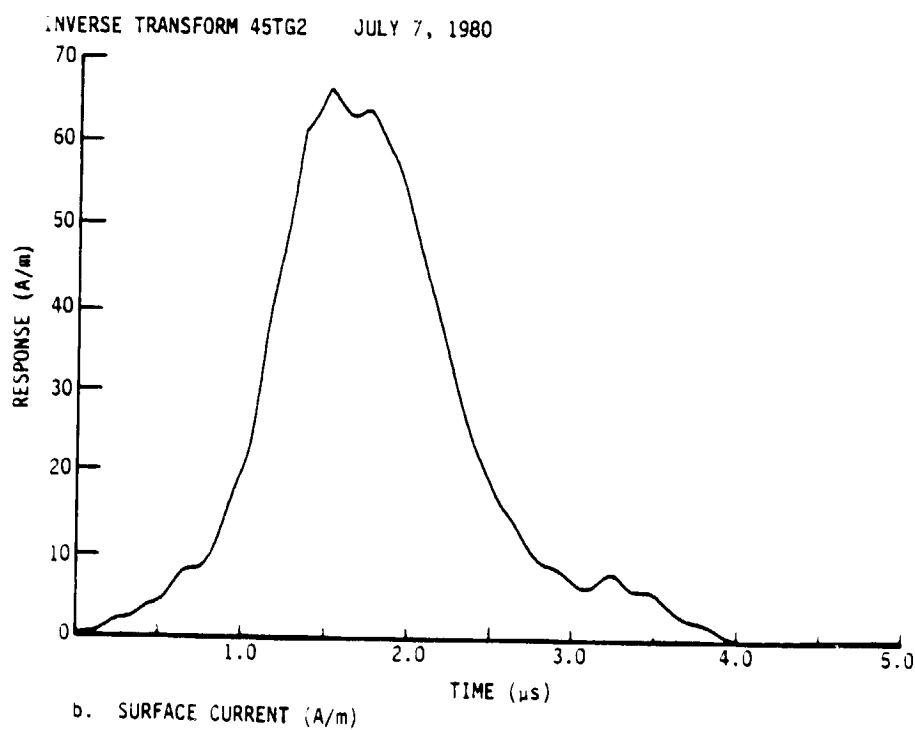
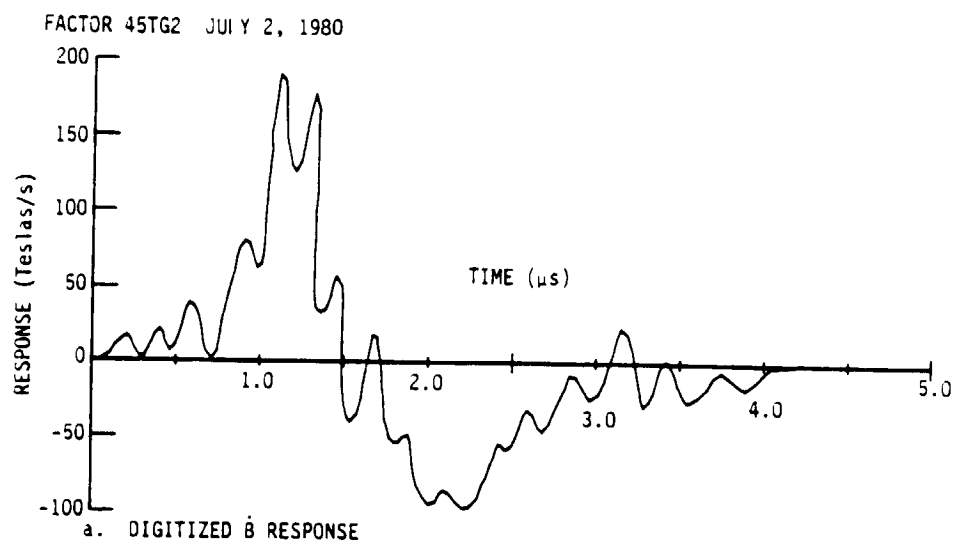
ORIGINAL PAGE IS
OF POOR QUALITY



RT-20734

Figure 46. Typical digitized blowoff and return currents, FEP Teflon, grounded configuration

ORIGINAL FILED IN OF POOR QUALITY

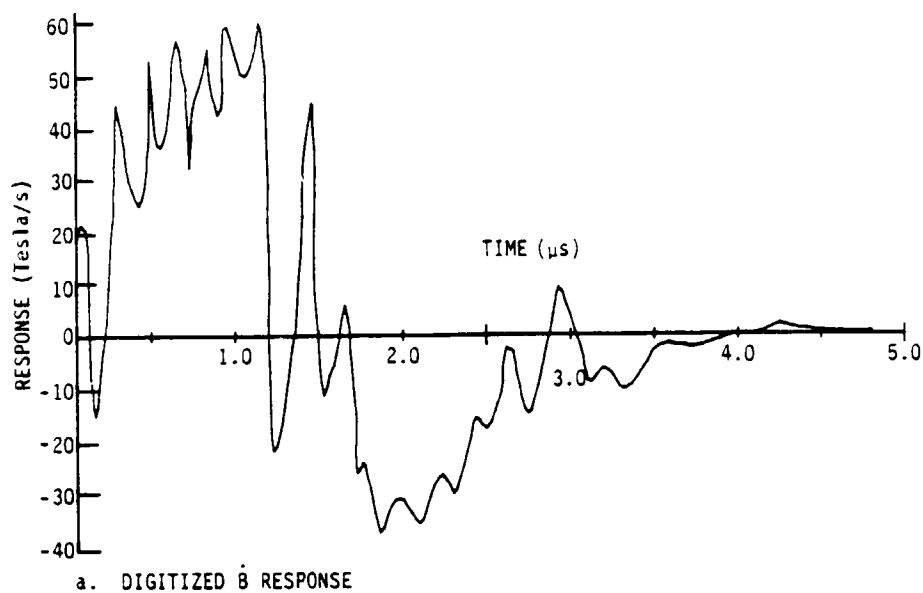


RT-20733

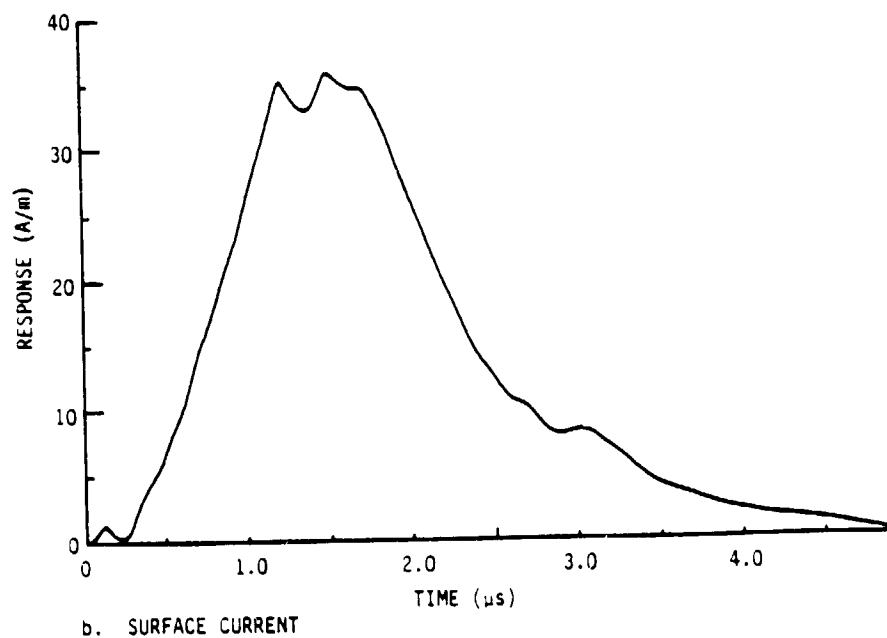
Figure 47. Digitized response of \dot{B} Sensor 4

ORIGINAL PAGE IS
OF POOR QUALITY

FACTOR 45TG3 JULY 7, 1980



INVERSE TRANSFORM 45TG3 JULY 10, 1980



RT-20726

Figure 48. Digitized response of \dot{B} Sensor 11

ORIGINAL RECORD
OF POOR QUALITY

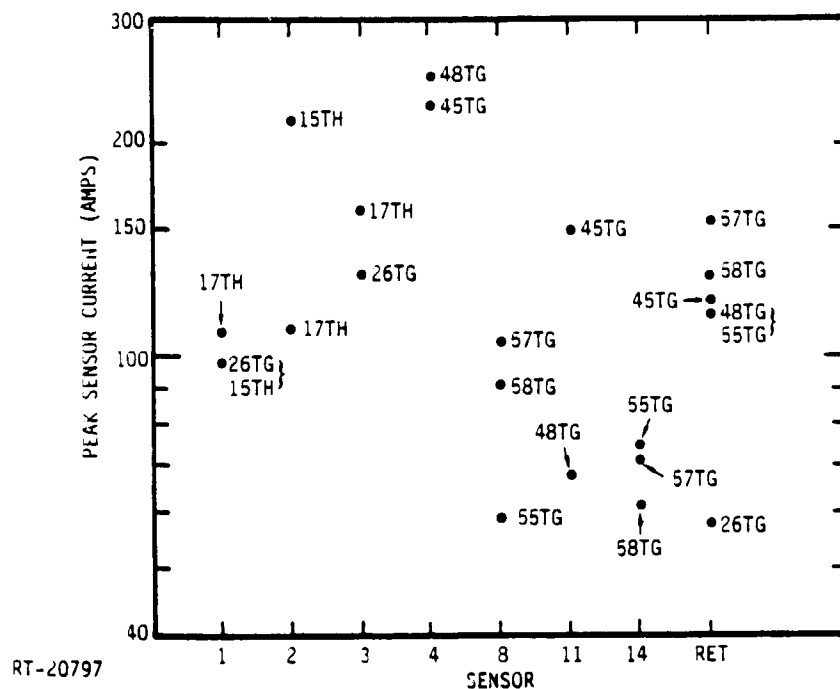


Figure 49. Estimated peak surface currents, Teflon

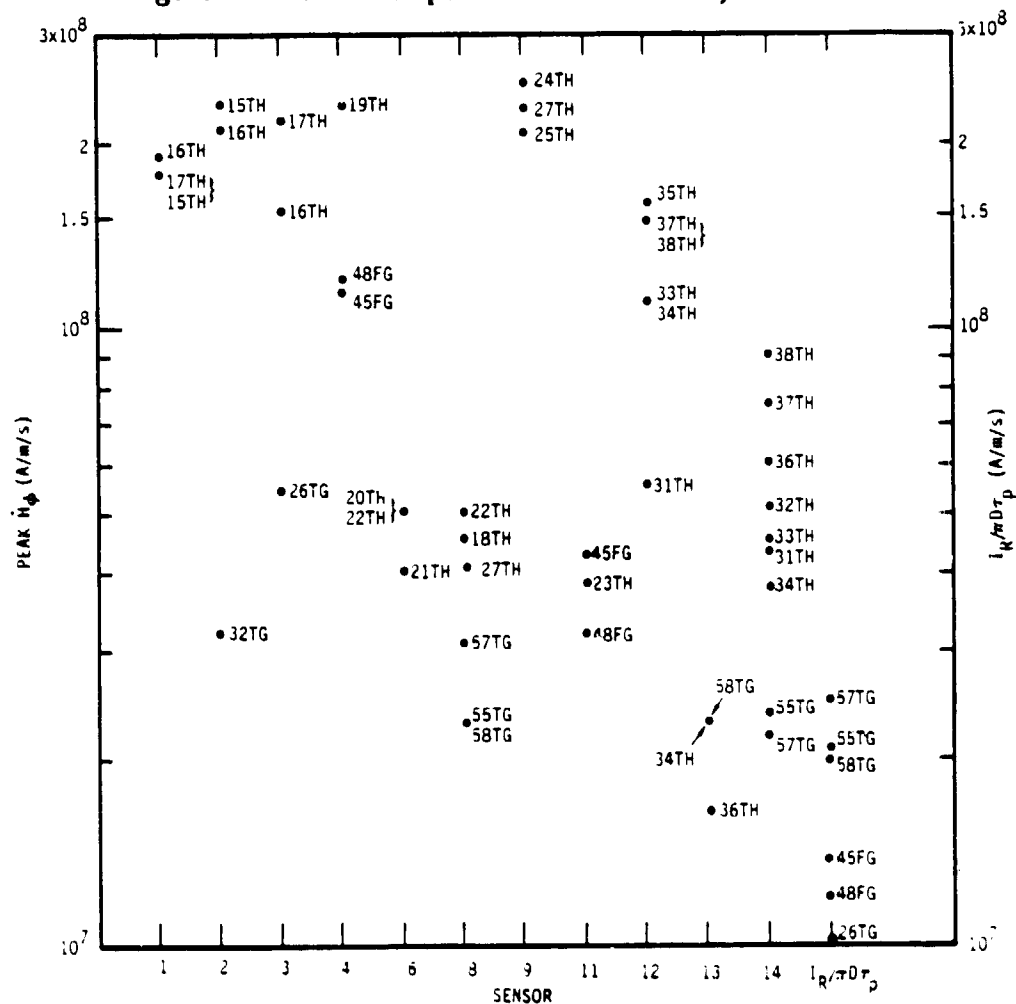


Figure 50. Peak B sensor responses, Teflon

components (I_n), each with a characteristic rise time τ_n , then the net sensor response is approximately

$$V \cong \mu_0 A_{\text{eff}} (I_1/\tau_1 + I_2/\tau_2 \dots) \quad (5)$$

Thus a higher frequency component will produce a larger sensor response per unit surface current. Characteristic ringing frequencies in sensor data for the high impedance configuration were typically clustered around 12 and >50 MHz, high compared to the predominant frequencies of the main pulse centered around 1 MHz.

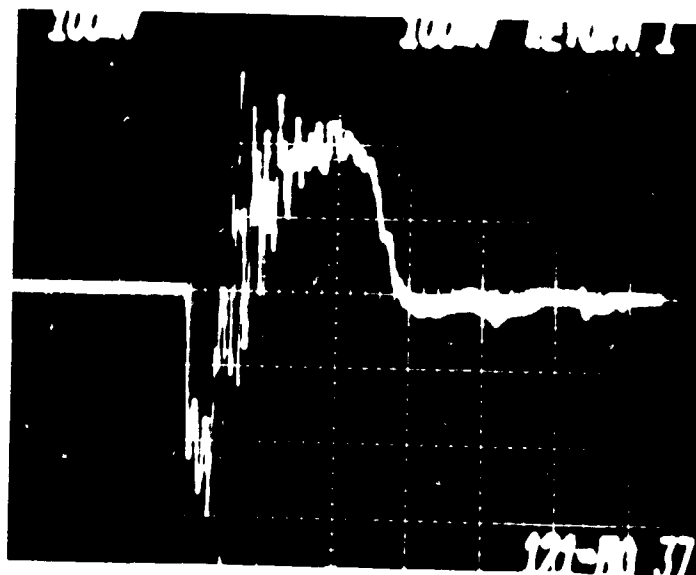
The enhanced high frequency component for the \dot{B} data is evident in the reproduction of sensor data in Figures 51 and 52. Other significant differences are apparent if compared to data recorded with the CAN grounded. First, the charge collected by the blowoff sensor is positive. The amplitude of the blowoff current in this case is comparable to that for the low impedance data. Second, the return current is typically bipolar (+,-). However, the amplitudes typically observed are not compatible with the value of $R = 1 \text{ M}\Omega$. Currents of the order of 1 A would imply voltages across the resistor of ca. 1 MV, clearly impossible, as the highest possible potential is the maximum surface potential of the CAN, <20 kV; relative to tank ground. It is felt that the most likely explanation for this occurrence is surface breakdown along the resistor during discharge. Data taken under similar conditions (Ref 37), indicates that the test object could have risen to voltages in excess of 10 keV for these charging conditions. Feedthrough breakdown is less likely as the vacuum feedthrough employed had a nominal capability of withstanding 25 kV.

Characteristic surface currents ranged up to 65 A/m based on a hand integration of the \dot{B} sensor data.

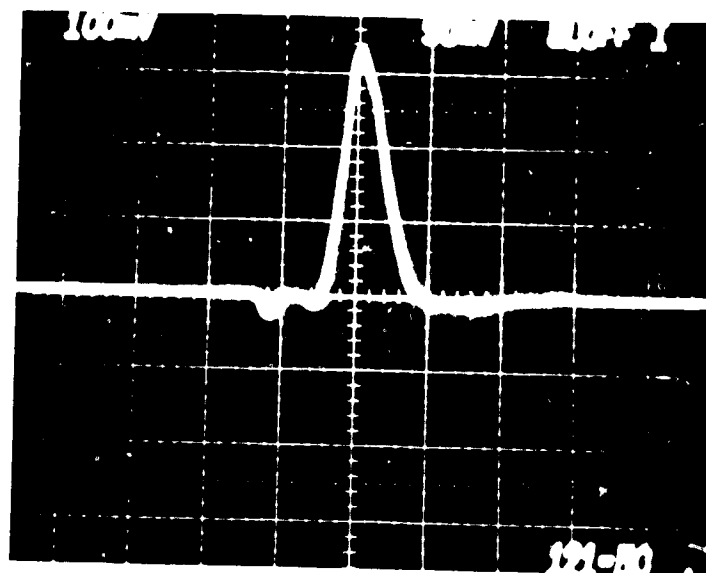
4.4 SOLAR ARRAY MOCKUP

A photograph of the solar panel mockup is shown in Figure 10, while schematics are shown in Figures 11 and 12. The same panel under electron irradiation is shown in Figure 53. Not surprisingly, the most active discharge sites are at the edges of coverslips. There was some question as to the mounting of these slips on the P78-2 array based on a charging analysis performed by NASA. Therefore, the test panel was constructed with half the coverslips glued down so that the MgF_2 antireflection coating faced out (normal-bottom of panel) and half with the SiO_2 face out (reversed-top half).

ORIGINAL PHOTOS
OF POOR QUALITY



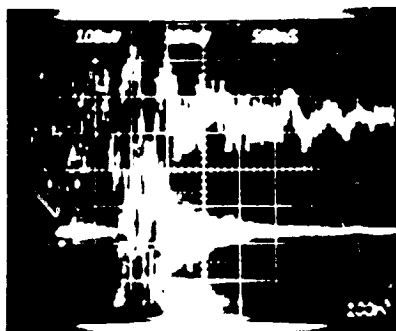
a. Return Vert: 1 A/div; Horiz: 500 ns/div



b. Blowoff Vert: 0.25 A/div; Horiz: 500 ns/div

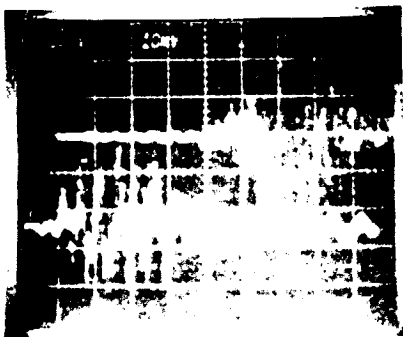
Figure 51. Sensor photos, Teflon, high-impedance configuration
(Sheet 1 of 2)

ORIGINAL PAGE IS
OF POOR QUALITY



c. Sensor 12

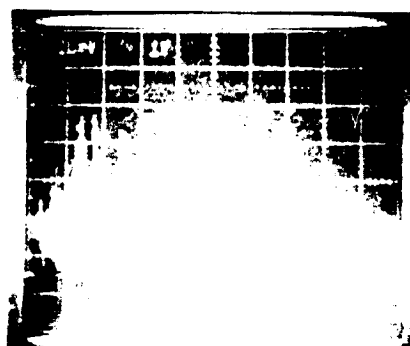
Upper: 1 μ sec delay, Vert: 29.9 T/sec, Horiz: 100 ns/div
Lower: Vert: 29.9 T/sec, Horiz: 500 ns/div



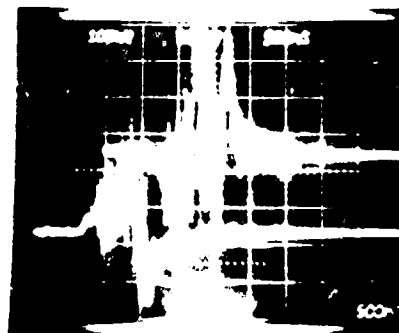
d. Upper: Sensor 13 Vert: 4.3 T/sec/div
Horiz: 200 ns/sec, 1.5 μ sec delay
Lower: Sensor 14 Vert: 17.4 T/sec/div
Horiz: 200 ns/div

Figure 51. Sensor photos, Teflon, high-impedance configuration
(Sheet 2 of 2)

ORIGINAL PAGE IS
OF POOR QUALITY



Channel 1
Sensor 3
24.6 T/s/div
500 ns/div



Channel 3
Sensor 2
30 T/s/div
500 ns/div

Channel 4
Sensor 1
21.4 T/s/div
500 ns/div



Return

2 A/div
500 ns/div

Figure 52. Sensor responses, FEP Teflon, high-impedance configuration

ORIGINAL PAGE
BLACK AND WHITE PHOTOGRAPH



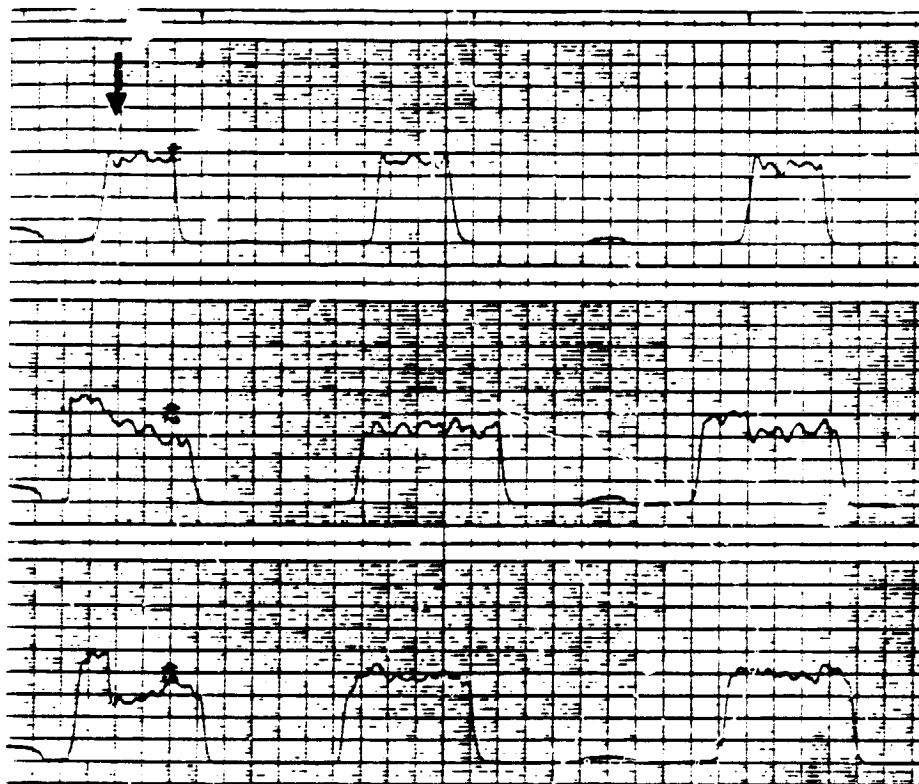
Figure 53. Discharges in the solar array mockup

For the exposure conditions, electrons only, the equilibrium charging potentials for the two panel halves were similar, as was the discharge behavior.

Surface potential scans showing a relatively large discharge for the panel is shown in Figure 54. Figure 55 depicts one showing a more representative series of charging and discharging cycles. One significant difference between the discharge behavior of the solar panel mockup and the other samples is that discharges were typically much smaller for identical charging conditions. A large discharge in the SA panel involved less than 20 percent of the injected charge, while typical discharges removed only a few percent. Discharges in Teflon and Kapton were much larger, involving up to 80 percent or more of the total deposited charge, depending on the charging conditions. There was little difference in the equilibrium charging potentials reached in the grounded and high impedance samples as expected, since charging is a quasi-DC process during which the potential of the CAN is essentially the same as that of the tank.

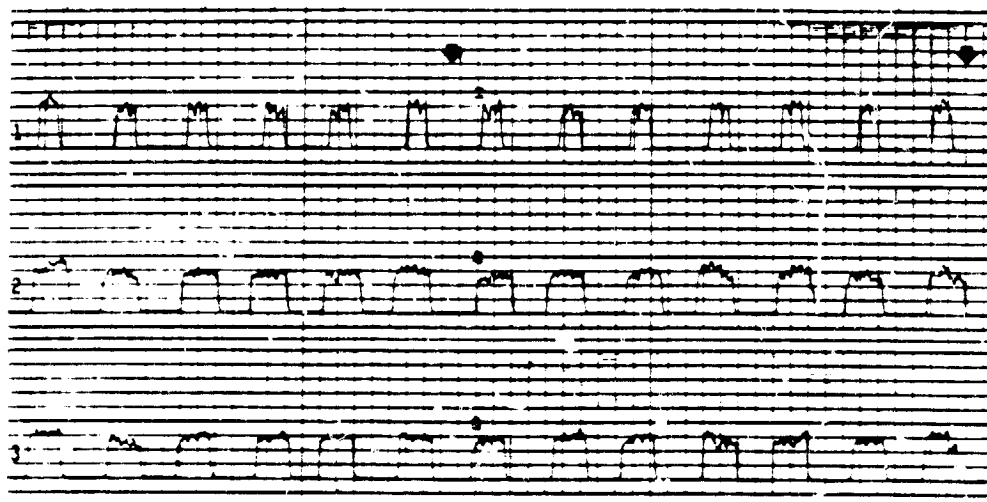
A typical set of discharge data is shown in Figure 56. The observed return current pulses were positive, with 10 to 20 A peaks, relatively symmetric, and with half maximum pulse widths of about 1.2 μ s. A few of the return current signals had amplitudes as large as 50 A. The peak currents and charge contained in the return current

ORIGIN OF OF POSSIBLE



RT-20974

Figure 54. Surface potential scan of the solar array mockup, grounded configuration. The arrow indicates the occurrence of a large discharge. Scale Vertical: 1 div = 2.5 kV.



RT-20762

Figure 55. Surface potential scan of solar array mockup, grounded configuration, $E_i = 20 \text{ keV}$, $J_i = 1.5 - 2.5 \text{ na/cm}^2$. Horizontal: 1 div = 2.5 sec. Vertical: 1 div = 2.5 kV. The arrows show the occurrence of a discharge.

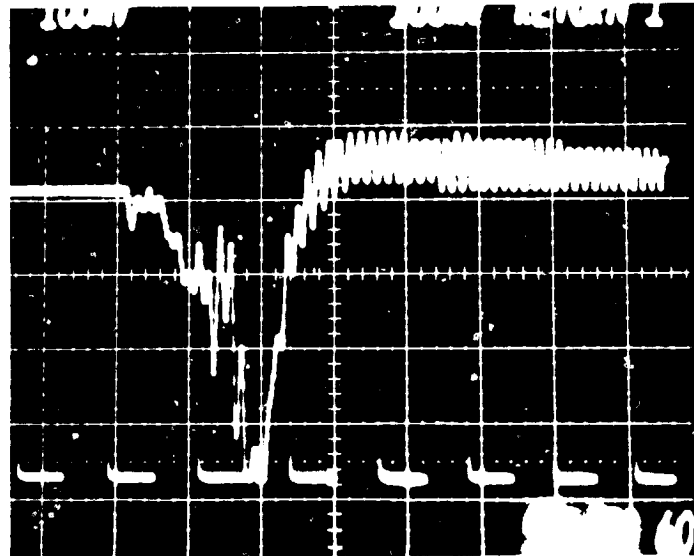
pulse places a lower bound on the magnitude of the blowoff discharge source. Visible in the return current and \dot{B} sensor photographs is a 6 to 7 MHz oscillation. This component was also present in the response of other samples, but was less in evidence because of the larger amplitude of the blowoff discharge which was the principal driver of the CAN replacement currents. We attribute the origin of the 6 to 7 MHz oscillation to the combined response of the CAN, ground strap and tank, primarily the inductance of the ground strap and the capacitance of the CAN to the tank.

Superimposed on the basic \dot{B} pulse shape is a second higher frequency component shown in Figure 56. The lower trace of this photo is the entire \dot{B} signal recorded at a horizontal sweep of $0.5 \mu\text{s}/\text{div}$. The upper trace is an expanded segment recorded at $0.1 \mu\text{s}/\text{div}$. Clearly evident is a high frequency ringing with a period of about 10 ns or 50 MHz. The relative amplitude of this component in the surface current is magnified in the \dot{B} measurement because of its more rapid rate of change of amplitude compared to that of the main signal (q.v., Equation 5). The blowoff and return current waveforms shown in Figure 56 were digitized and plotted in Figure 57 and are typical of large amplitude solar array discharges. The corresponding \dot{B} data for sensor 8 are shown in Figure 58.

A summary of the peak response data for the \dot{B} sensors is plotted in Figure 59. In addition, we have plotted the average rate of rise of the return current pulse $I_{R \text{ peak}}/\tau_p \cdot \pi D$, where τ_p is the peak time, measured from pulse onset divided by the circumference of the CAN, $\pi \times 1.36 \text{ m}$. Also plotted are peak backplane wire currents. It can be seen that there is considerable scatter in the data. However, the H_p data is centered at about $9 \times 10^6 \text{ A/m/s}$, while the return current data is centered on about $3.5 \times 10^6 \text{ A/m/s}$. If the return current and the blowoff current were substantially equivalent, then one would expect that on the average, $I_R/\tau_p \pi D \geq I_s$. Reasons for the failure for this inequality to hold include:

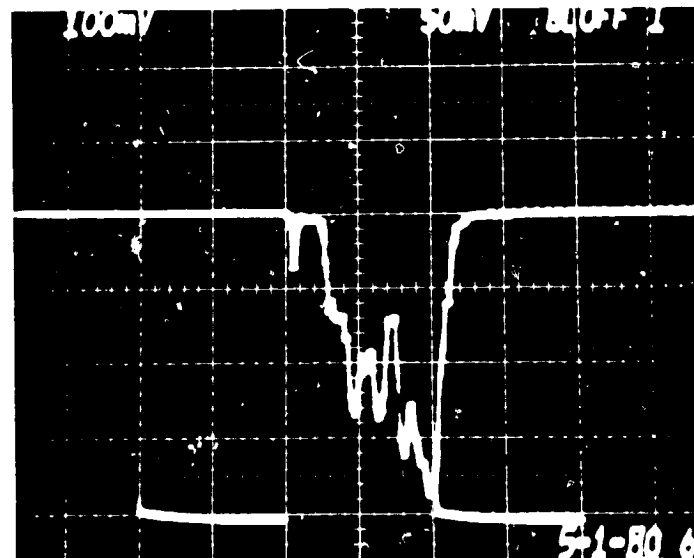
1. \dot{B} data also includes high frequency components which raise the peak amplitude but do not contribute significantly to the average peak return or surface currents.
2. The average rate of rise of the return current is less than its peak value.
3. For surface current pulses of the shape of the integrated \dot{H} signal like that in Figure 58, the peak \dot{B} (or \dot{H}) is about twice the average value. It is more reasonable to compare $H_{av} \cong H_p/2$ to I_p/τ_p . Such a comparison provides more reasonable agreement.

ORIGINAL PAGE
BLACK AND WHITE PHOTOGRAPH



a. Return Current

Horizontal: 1 μ sec/div
Vertical: 12.5 A/div

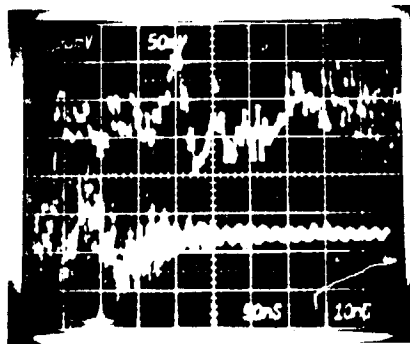


b. Blowoff Sensor

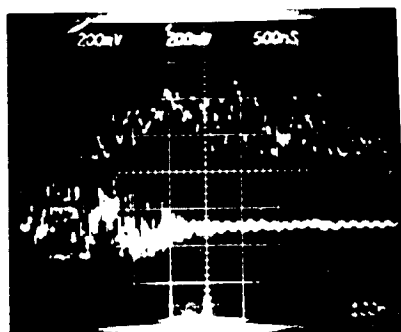
Horizontal: 1 μ sec/div
Vertical: 0.05 A/div

Figure 56. Photographs of response of solar array mockup, grounded configuration
(Sheet 1 of 2)

ORIGINAL PAGE
BLACK AND WHITE PHOTOGRAPH



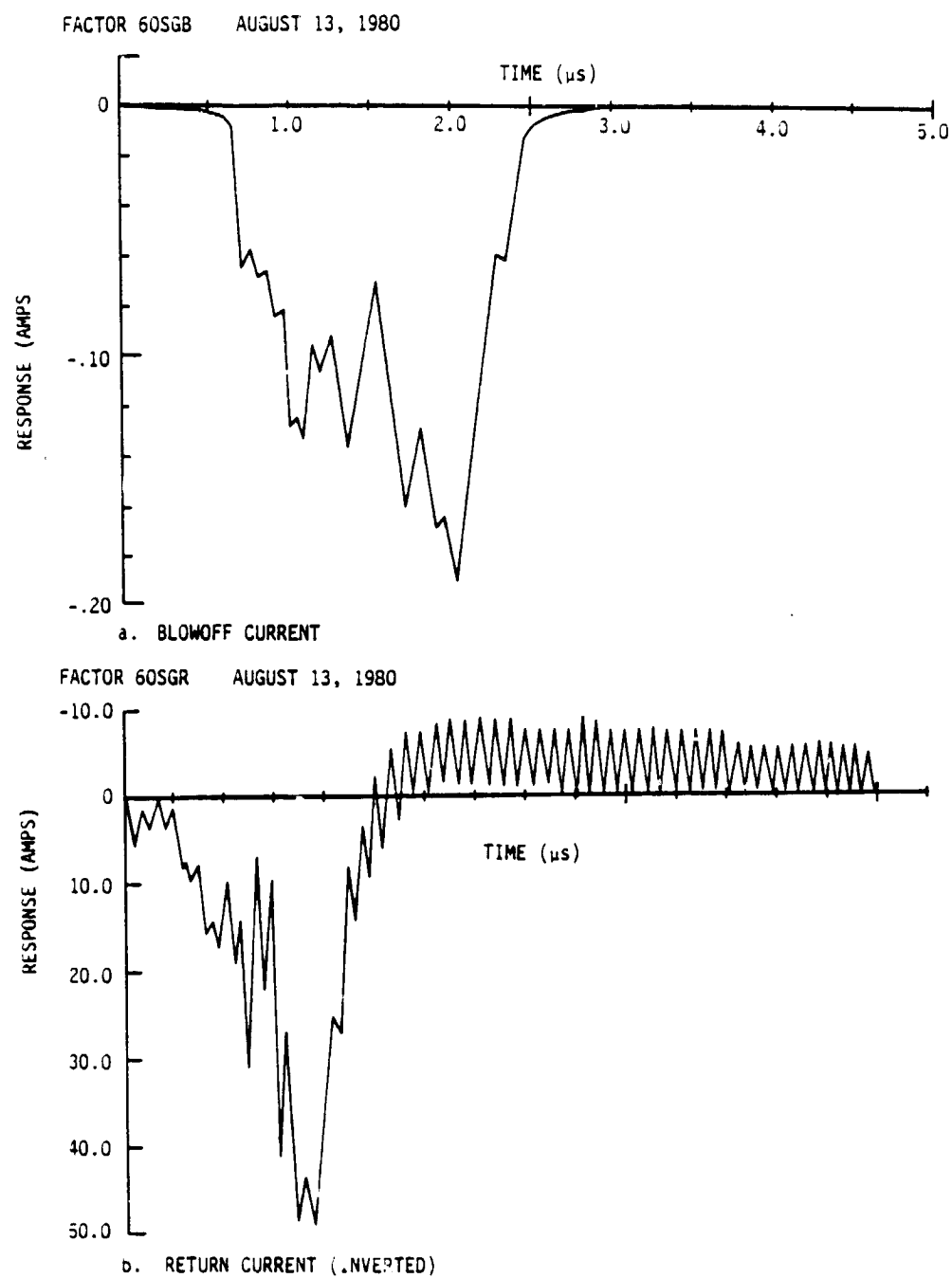
- c. Upper - Sensor 11 Horiz: 100 ns/div Vert: 5.4 T/div
Lower - Sensor 11 Horiz: 500 ns/div Vert: 5.4 T/div



- d. Upper - Sensor 8 Horiz: 100 ns/div Vert: 13.8 T/div
Lower - Sensor 8 Horiz: 500 ns/div Vert: 13.8 T/div

Figure 56. Photographs of response of solar array mockup, grounded configuration
(Sheet 2 of 2 sheets)

ORIGINAL PAGE IS
OF POOR QUALITY



RT-20741

Figure 57. Digitized return and blowoff currents, grounded solar array mockup

ORIGINAL PAGE IS
OF POOR QUALITY

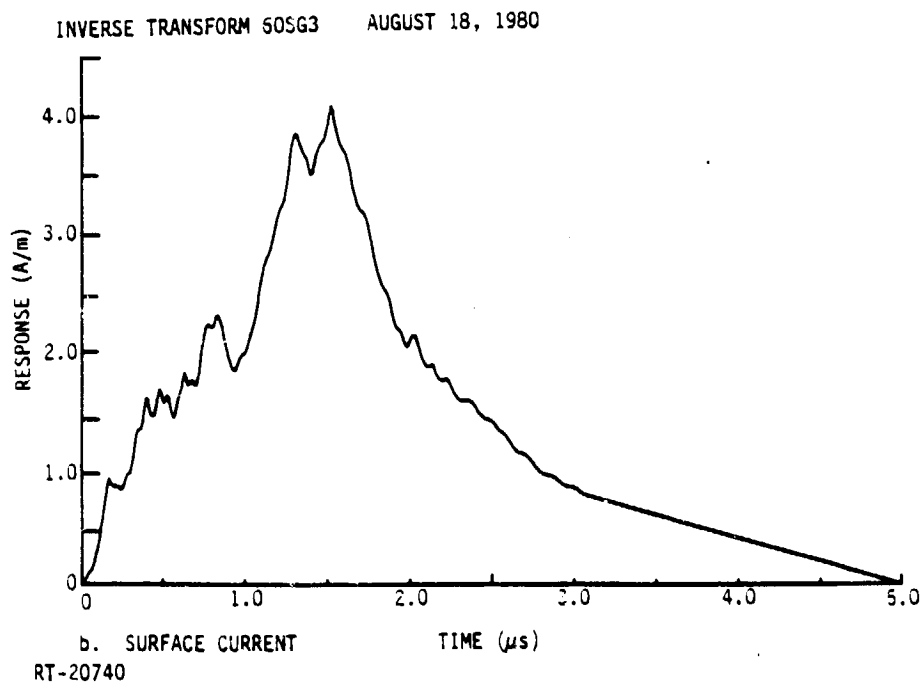
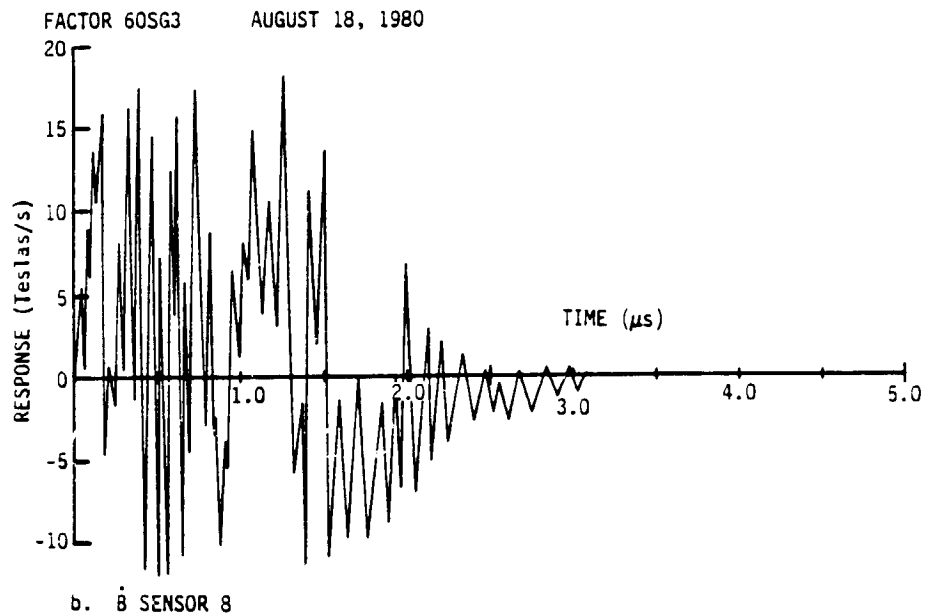


Figure 58. Digitized response of \dot{B} Sensor 8, solar array mockup, grounded configuration

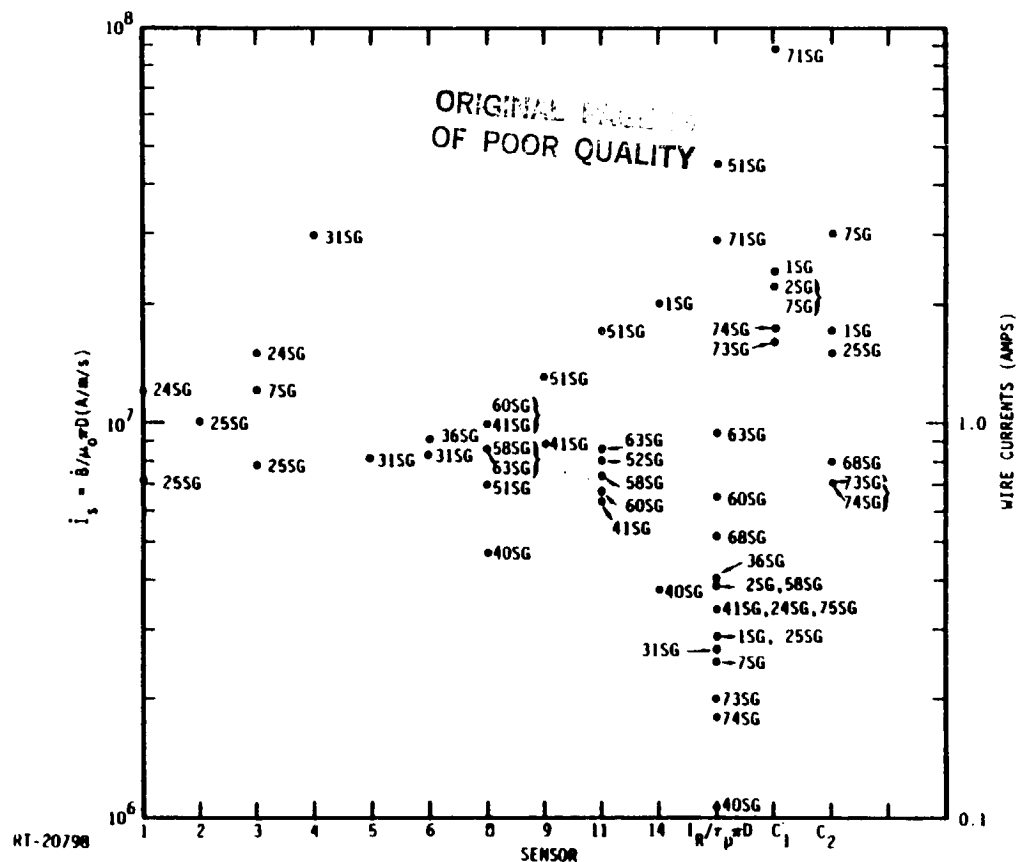


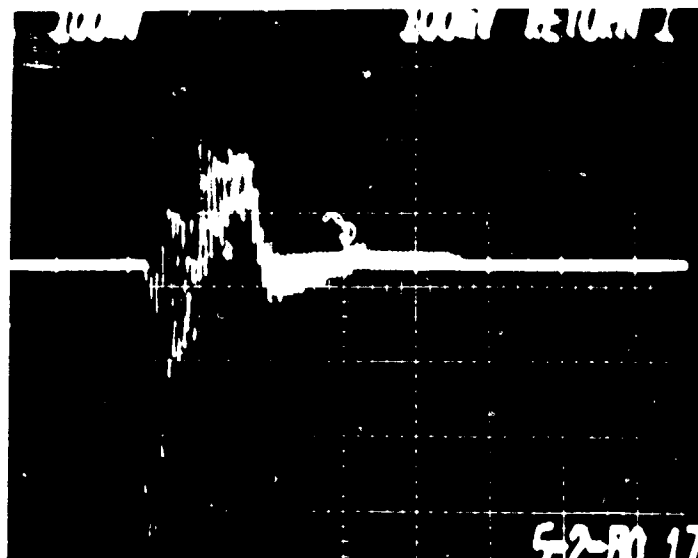
Figure 59. Normalized peak \dot{B} sensor response solar array mockup, grounded configuration

Based on the data presented in Figure 59, one may conclude that representative peak blowoff currents are at least 15 A as measured by the corresponding return currents while corresponding surface currents are about 4.5 A/m. Very large amplitude pulses may be three times larger.

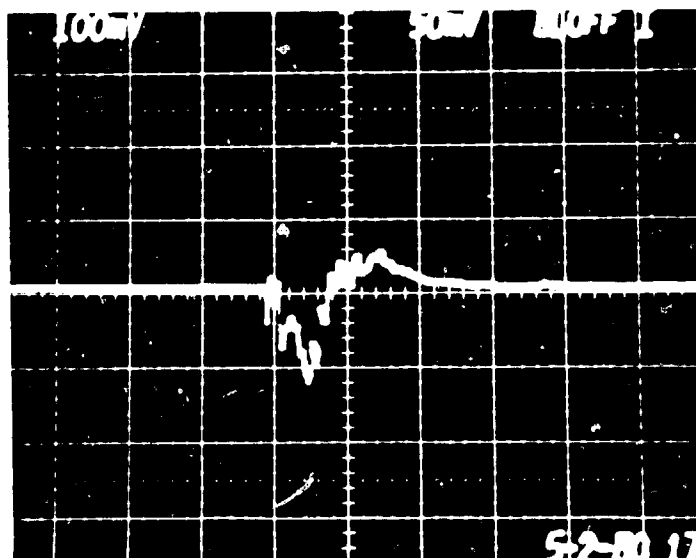
A representative set of sensor data is shown in Figure 60 for the responses produced in the CAN (high impedance configuration) by discharges in the solar array mockup. Figures 61 and 62 show digitized waveforms. Return signals are one to two amps in magnitude, bipolar (+,-) and contain a significant component of higher frequency ringing at 13 to 14 MHz. As the nominal resistor in series with the return line is 1 M Ω , partial, but nondestructive breakdown, of this component must have occurred during discharge. The ringing can be seen in the \dot{B} photo (Figure 60). Also present is a second, higher frequency component with a characteristic frequency of 50 MHz, or greater. Some of the \dot{B} photos also showed evidence of a very small, extremely high frequency component with a period of 170 to 200 MHz.

Peak \dot{B} sensor and backplane wiring data is plotted in Figure 63. The peak \dot{B} data for the sensors on top of the CAN (1-4) are somewhat higher than those for the low impedance configuration. This is due, in part, to the fact there appeared to be more of the high frequency components in the response as reflected in the return current pulses,

BLACK AND WHITE PHOTOGRAPH



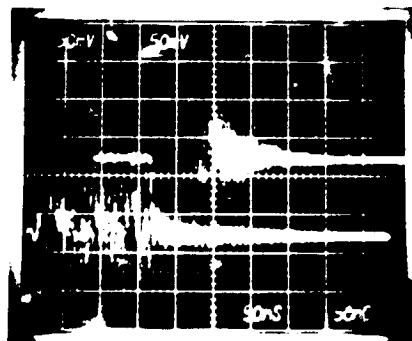
a. Return
Vert: 2.5 A/div
Horiz: 1 μ sec/div



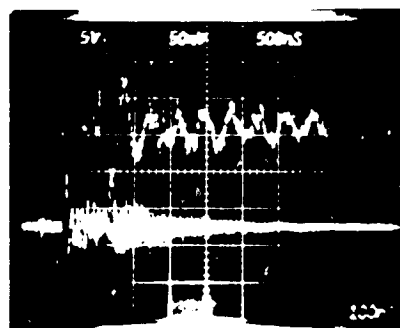
b. Blowoff
Vert: 0.1 A/div
Horiz: 1 μ sec/div

Figure 60. Photographs of sensor responses solar array, high impedance configuration,
(Sheet 1 of 2 sheets)

ORIGINAL PAGE
BLACK AND WHITE PHOTOGRAPH



- c. Upper - Sensor 1 Horiz: 500 ns/div Vert: 24 T/sec/div
Lower - Sensor 3 Horiz: 500 ns/div Vert: 14 T/sec/div

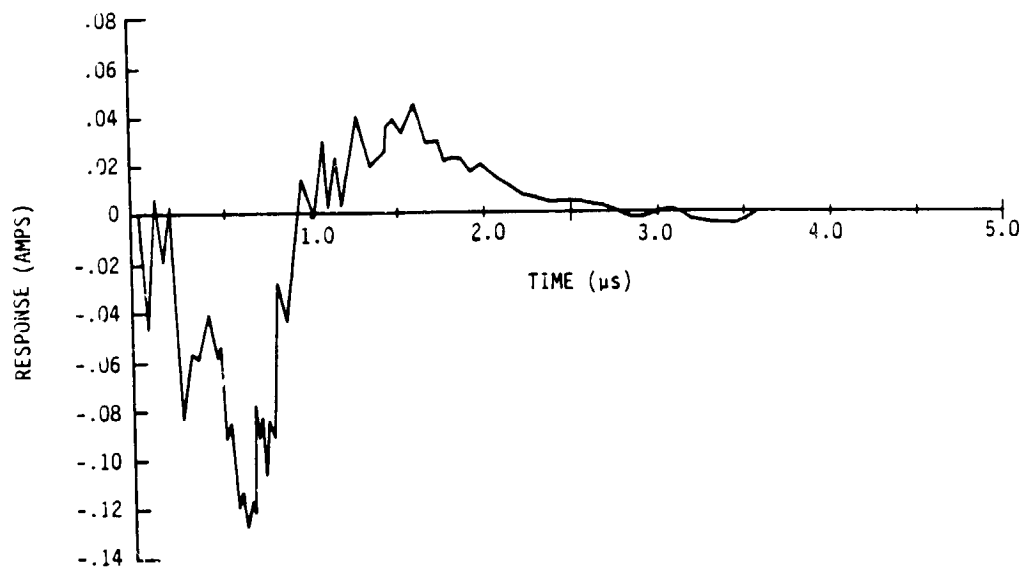


- d. Channel 3 Channel 4
Upper - Sensor 2 Horiz: 100 ns/div Vert: 35 T/sec/div
Lower - Sensor 2 Horiz: 500 ns/div Vert: 35 T/sec/div

Figure 60. Photographs of sensor responses solar array, high impedance configuration,
(Sheet 2 of 2 sheets)

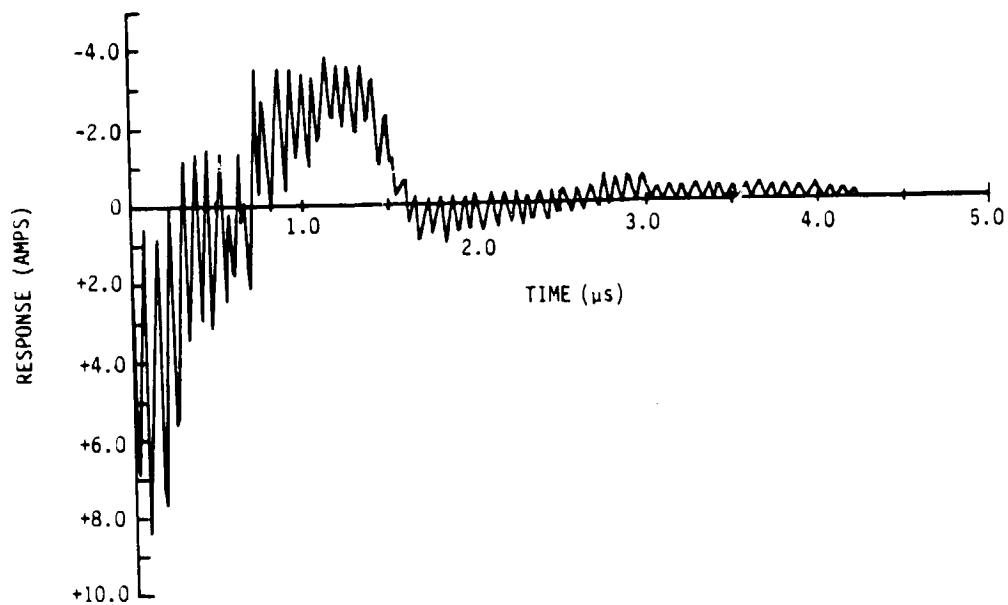
ORIGINAL RECORD
OF PULSE QUALITY

FACTOR 17SHB AUGUST 11, 1980



a. BLOWOFF CURRENT

CHECK 17SHR AUGUST 11, 1980

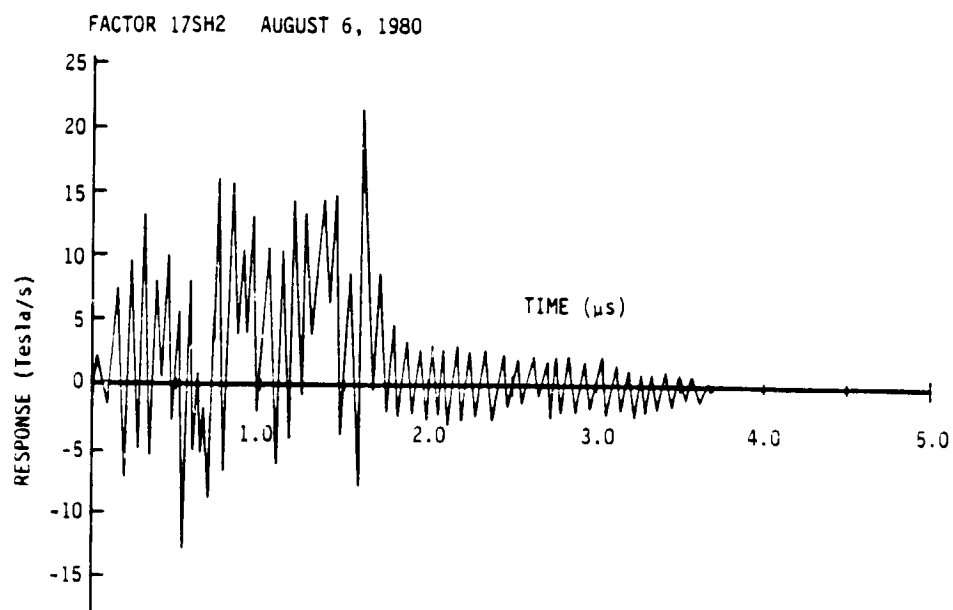


b. RETURN CURRENT

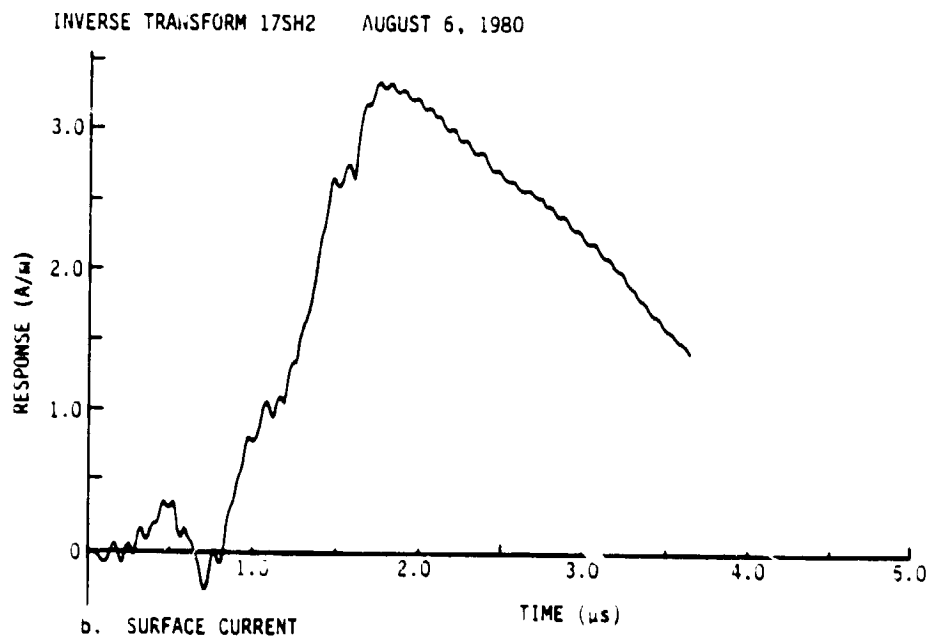
RT-20742

Figure 61. Digitized return and blowoff currents, solar array mockup, high-impedance configuration

ORIGINAL PAGE IS
OF POOR QUALITY



a. \dot{B} SENSOR 1



b. SURFACE CURRENT

RT-20748

Figure 62. Digitized \dot{B} sensor data, solar array mockup, high-impedance configuration

ORIGINAL PAGE IS
OF POOR QUALITY

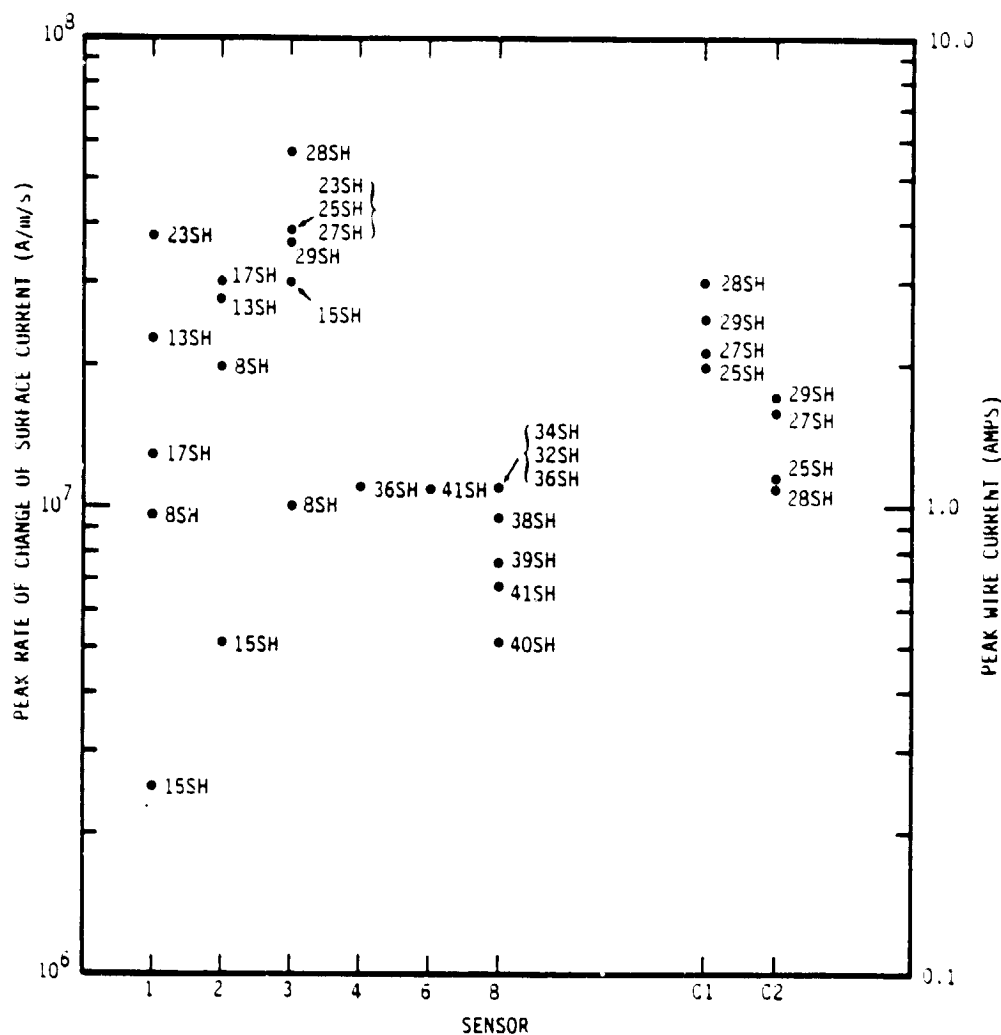


Figure 63. Peak B sensor and backplane wire currents for the solar array mockup, high impedance configuration

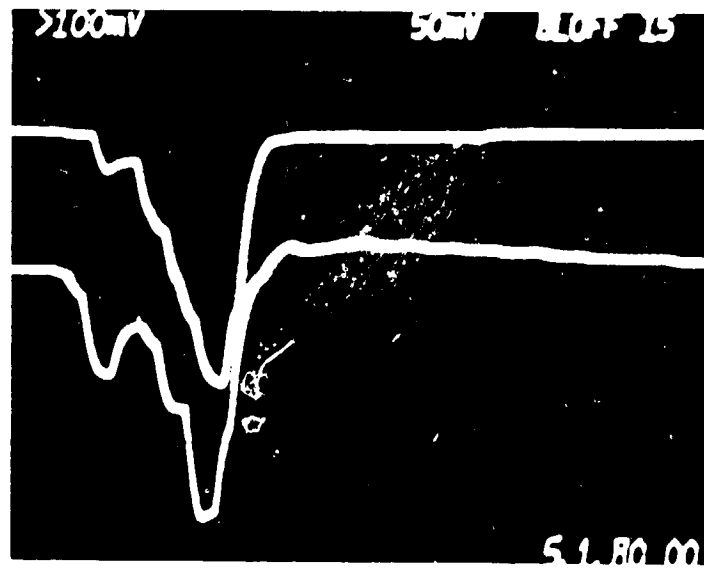
many of which were rapidly rising ($\tau_r < 0.2$ ns) and contained more high frequency ringing.

The backplane wire currents in the high impedance case were comparable to those seen when the CAN was grounded.

The blowoff currents were often bipolar (-,+) with the negative component predominant and about 0.05 to 0.2 A peak.

In order to obtain energy information about the energies of blowoff particles, some simple time-of-flight measurements were made. In these, both the return current and blowoff signals were input to a dual-channel transient digitizer. The blowoff signal was used as a trigger for both sweeps. A representative signal is shown in Figure 64 for a discharge in the mock solar array with the CAN grounded. This photo is typical of

ORIGINAL PAGE
BLACK AND WHITE PHOTOGRAPH



Upper: Blowoff, Vert = 0.05 A/div; Horiz. = 1 μ sec/div
Lower: Return, Vert = 5 A/div; Horiz. = 1 μ sec/div

Figure 64. Relative timing of blowoff and return current signals for solar array mockup

several that were taken for the different materials. It can be seen that the blowoff current is similar in shape to, but follows the return current by about 300 ns. While there was some shot-to-shot variation, both in relative pulse shape and onset time, in almost every pulse pair recorded in this manner, the blowoff signal followed the return pulse by a time which was typically a few hundred nanoseconds. For $\Delta t = 300$ ns, this corresponds to electrons whose average energy is 71 eV, much less than the discharge potential of the CAN both before and after a discharge.

4.5 ELECTRICAL TEST DATA

4.5.1 Introduction

The ultimate objective of the ground test program is to develop electrical excitation procedures which reproduce important features of the response induced in spacecraft as a consequence of space electron induced discharges. The approach being taken is to develop an electrical system qualification test which mimics the replacement currents generated consequent to an EID on the external structure. As part of this overall program electrical excitations of the CAN test object were performed which simulate different canonical discharges. These excitations were of two types:

1. A capacitive direct drive test, whose aim is to stimulate the structural response produced by the blowoff of electrons which is a major driver for the response.

2. An arc discharge which simulates a punchthrough discharge which seems to be part of the discharge process, but not necessarily a dominant driver. To some degree, flashover is also simulated by such a test.

The first set of tests was performed as part of an SGEMP Analysis Verification Program performed under AFWL Contract F29601-74-C-105 (Ref 39). The second set of tests were performed as part of Phase I of the present program (Ref 1) where the intent was to demonstrate the relative effectiveness of simulation of blowoff and flashover/punchthrough in producing structural replacement currents.

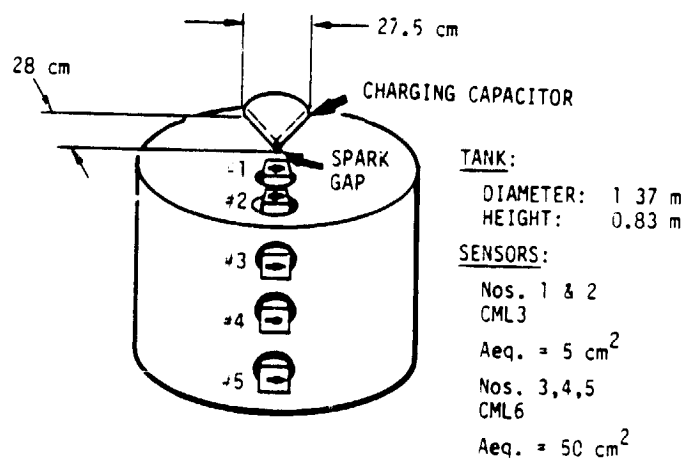
At the time these tests were performed, it was believed that discharge pulses were relatively narrow, i.e., of the order of a few tens of nanoseconds. In addition, the available electrical techniques for producing arc discharge simulations also involved relatively narrow pulses. For example, the FWHM of the recommended MIL-STD-1541 arc is typically less than 10 ns.

A parallel effort was to ascertain the ability of conventional SGEMP coupling codes to predict structural responses if suitable source terms for the discharge were incorporated, and to provide a means of scaling between different driver in order to obtain normalized response comparison and to be able to predict the response of an object to an arbitrary excitation. In this section, we review the pertinent electrical test results. Comparison between the electrical excitations, and the electron spraying discharge data and model calculations is made in Section 5.4.

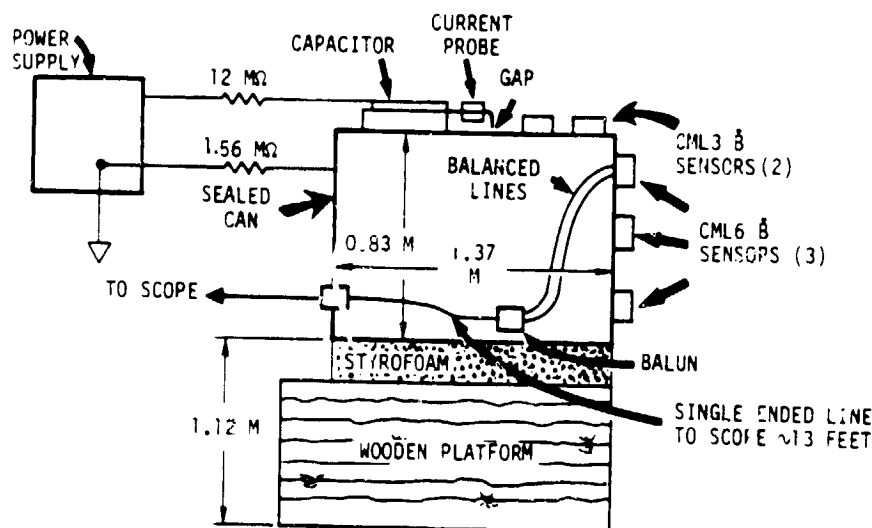
4.5.2 Arc Discharge Experiment

Only a brief summary of the arc discharge experiment will be given here. A more extensive discussion can be found in Section 3.4, Volume I of Reference 1. Basically, the intent of the experiment shown in Figure 65 was to simulate an arc. The source was a tear-drop shaped 60 nF capacitor whose dielectric was made from 1 mil Mylar. The intent in using such a shape was to leave a region near the discharge uncovered, i.e., to minimize the perturbation of external fields in areas where measurements were being taken. The capacitor was charged by a high voltage power supply until the spark gap located at the center of the top of the CAN broke down, typically at about 1.4 kV. The test object was isolated from ground during the discharge by dielectrically isolating it and inserting 13.56 M Ω in series with the power supply charging the dielectric. Measurements were taken with a series of B sensors of the same type as were used in the electron spraying experiment. The discharge current was monitored with a current

ORIGINAL PAGE IS
OF POOR QUALITY



(b) SENSOR PLACEMENT



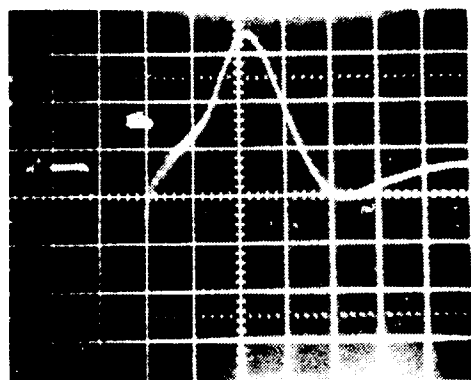
(a) EXPERIMENTAL SETUP. THE THICKNESS OF THE CHARGING CAPACITOR AND GAP SIZE ARE EXAGGERATED TO SHOW DETAIL.

RT-1639;

Figure 65. Arc discharge test configuration

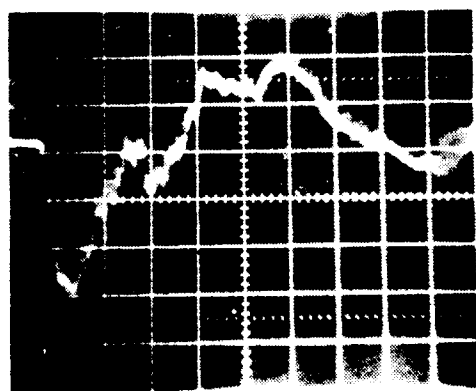
probe across the low inductance spark gap. Sensor data was recorded both with fiber optics to maintain dielectric isolation and with hard wire for comparison.

A typical discharge current waveform is shown in Figure 66. These pulses were 750 to 1000 A peak, with a full width at half maximum of about 40 ns, showing crossover at ~80 ns and 240 ns. Note that this is comparable to the largest amplitude blowoff discharge source terms inferred from the EID experiments on the CAN and similar experiments. Typical \dot{B} data is shown in Figure 67. Data was taken with \dot{B} sensors placed along the line of symmetry of the tear-drop capacitor (180°) and at right angles (90°) to look for asymmetries in the response. An interesting point to note is that the hardwire and fiber optic coupled data were similar but not identical. The fiber optic data showed a 67 MHz oscillation superimposed on the main \dot{B} signal which was



Vertical: 250 A/div
Horizontal: 50 nsec/div
Peaks: -1000A, +750A
O Crossovers: 80 and 240 nsec

Figure 66. Arc discharge current waveform, hardwired configuration



10 mV/div
20 nsec/div
Approximately 70 tesla/sec-div

Figure 67. Response measured by CML3 sensor at position 1

not evident in the hardwire data. The shape of the \dot{B} signals are what would be obtained if the signal in Figure 66 were differentiated.

The results of the \dot{B}_ϕ measurements are contained in Table 5. They have been normalized to a 1000 amp peak drive current. As these are purely electrical data, the response should scale linearly with the magnitude of the current. For comparison the \dot{B}_ϕ data was integrated assuming that the source term and \dot{B} pulses had the same shape as those in Figures 66 and 67. For comparison some of the analytical predictions based on calculations made with the SABER SGEMP code have been included for two scaling approximations, one that the \dot{B} response scales at the peak rate of change of the source term (I_p/τ_p), the other that the response scales as the rate of change of potential across the capacitor ($\dot{V}_p = \dot{Q}_p/C = I_p/C$). These calculations, which are described in detail in Section 6.4 of Reference 1, are discussed in Section 5.4 of this report. For comparison, note that I_p/τ_p for the EID data was typically 10^7 to 10^8 A/s. For the normalized CAN arc discharge data $I_p/\tau_p = 3.5 \times 10^{10}$ A/s.

Table 5. Data Set for Arc Discharge (From Ref. 1)

Data System	Location ^c	Measured Peak Sensor Response (Teslas/sec) ^d				
		1	2	3	4	5
HW ^a	180°	490	140	16	16	17
FO ^b	180°	640 ^d	81	11	6	6.5
HW	90°	954	186	21	22	21
Integrated Peak Response ^e (A/m)						
HW	180°	10.7	3.1	0.35	0.35	0.37
FO	180°	14.0	1.8	0.24	0.13	0.14
HW	90°	20.9	4.1	0.46	0.48	0.46
Calculated Peak Response (Teslas/sec)						
	180° (I _p /C _p) ^f	90	16	2.7	1.2	0.8
	180° (I _p /τ _p) ^g	760	135	23	10	7
	90° (I _p /C _p) ^f	225	45	5	1.4	0.6
	90° (I _p /τ _p) ^g	1902	380	42	12	5

^aH.W. = Hardwire

^bF.O. = Fiber Optic

^cLine of sensors relative to axis of symmetry of tear-drop capacitor.

^dScaled to 1000 A peak current

^eAssuming pulse shapes like those in Figures 66 and 67.

^fScaled to same peak rates of charge capacitor potential as in arc discharge experiments.

^gScaled to same peak rate of change of source current as in arc discharge experiments (3.5 x 10¹⁰ A/s).

4.5.3 CDI Tests

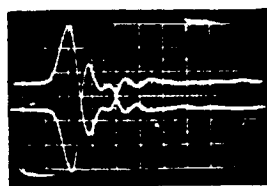
Capacitive direct drive injection excitations of the CAN were made using the setup shown in Figure 68. The CAN was isolated from ground and response data was taken via dielectric data links. The Anvil 160 pulser shown in the figure is battery powered and triggered through a fiber optic line. It produces a fast rising and relatively narrow pulse whose amplitude and shape are dependent on the location, shape and separation from the CAN of the drive plate, but which typically have rise times of a few nanoseconds and a FWHM of less than 10 ns. A damping resistor, inserted in series with the drive wire, was adjusted for each configuration to provide optimum damping of current oscillations. For the 79 cm diameter plate and 30 cm plate spacing 150Ω was used. Note that the pulser was mounted inside the CAN as shown in Figure 68 rather

ORIGINAL PAGE
BLACK AND WHITE PHOTOGRAPH

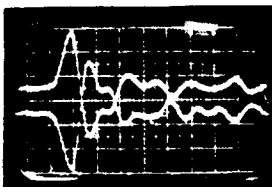
Normal (top)
50 $\text{Wb/m}^2\text{-s/div}$
82.5 $\text{Wb/m}^2\text{-s peak}$
Reverse (bottom)
50 $\text{Wb/m}^2\text{-s/div}$
105 $\text{Wb/m}^2\text{-s peak}$



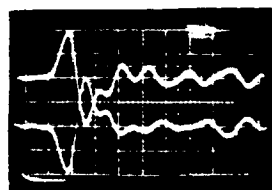
Normal (top)
100 $\text{Wb/m}^2\text{-s/div}$
230 $\text{Wb/m}^2\text{-s peak}$
Reverse (bottom)
100 $\text{Wb/m}^2\text{-s/div}$
250 $\text{Wb/m}^2\text{-s peak}$



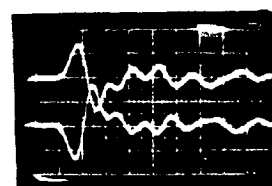
Normal (top)
12.5 $\text{Wb/m}^2\text{-s/div}$
28.8 $\text{Wb/m}^2\text{-s peak}$
Reverse (bottom)
12.5 $\text{Wb/m}^2\text{-s/div}$
28.8 $\text{Wb/m}^2\text{-s peak}$



Normal (top)
12.5 $\text{Wb/m}^2\text{-s/div}$
22.5 $\text{Wb/m}^2\text{-s peak}$
Reverse (bottom)
12.5 $\text{Wb/m}^2\text{-s/div}$
22.5 $\text{Wb/m}^2\text{-s peak}$



Normal (top)
12.5 $\text{Wb/m}^2\text{-s/div}$
16.3 $\text{Wb/m}^2\text{-s peak}$
Reverse (bottom)
12.5 $\text{Wb/m}^2\text{-s/div}$
16.3 $\text{Wb/m}^2\text{-s peak}$

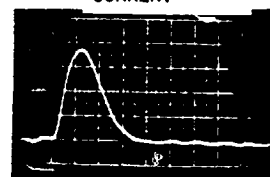


DRIVE PLATE

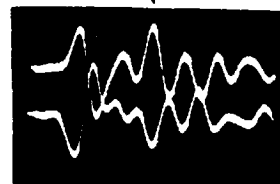
DAMPING
RESISTOR

ANVIL PULSER
FO TRIGGER

D CURRENT



0.2 A/div
0.73 A peak



HORIZONTAL SCALE 5 ns/div
8 FIELDS FOR 0.3 m PLATE HEIGHT
SOLID CYLINDER - CURRENT DRIVE

Normal (top)
5.0 $\text{Wb/m}^2\text{-s/div}$
7.5 $\text{Wb/m}^2\text{-s peak}$
Reverse (bottom)
5.0 $\text{Wb/m}^2\text{-s/div}$
8.0 $\text{Wb/m}^2\text{-s peak}$

Figure 68. Representative \dot{B} data set for CDI excitation of the CAN

than outside as was the case for the SCATSAT tests (q.v., Figure 13b, Reference 2). This is immaterial insofar as the electrical excitation of the structure is concerned as it only affects the polarity of the response.

A typical set of B_ϕ data for a plate spacing of about 0.3 m is shown in Figure 68 as a function of distance from the drive wire. The corresponding surface currents (H_ϕ) are shown in Figure 69. For the most part the surface currents follow the drive pulses. Because of the drive configuration, the response shows azimuthal symmetry in contrast with the arc injection which had an asymmetric drive plate (although the arc discharge was along the axis of symmetry of the CAN). For this case $t_r \sim 5.5$ ns and the FWHM is ~ 9 ns. Table 6 presents a data summary for the CAN as a function of plate spacing. The corresponding sensor locations are shown in Figure 68. The various calculations for response prediction and data comparison are discussed in Section 5.4. For the data of Figure 68, $I_p / \tau_p \approx 0.73 \text{ A} / 5 \text{ ns} = 1.4 \times 10^8 \text{ A/s}$. For comparison, predictions of the corresponding \dot{B} responses made with the ABORC SGEMP code are also given. The calculated \dot{B} pulse shapes are generally what one would expect if the drive pulse is differentiated. The calculated H_ϕ responses generally follow the current source terms.

ORIGINAL PAGE
BLACK AND WHITE PHOTOGRAPH

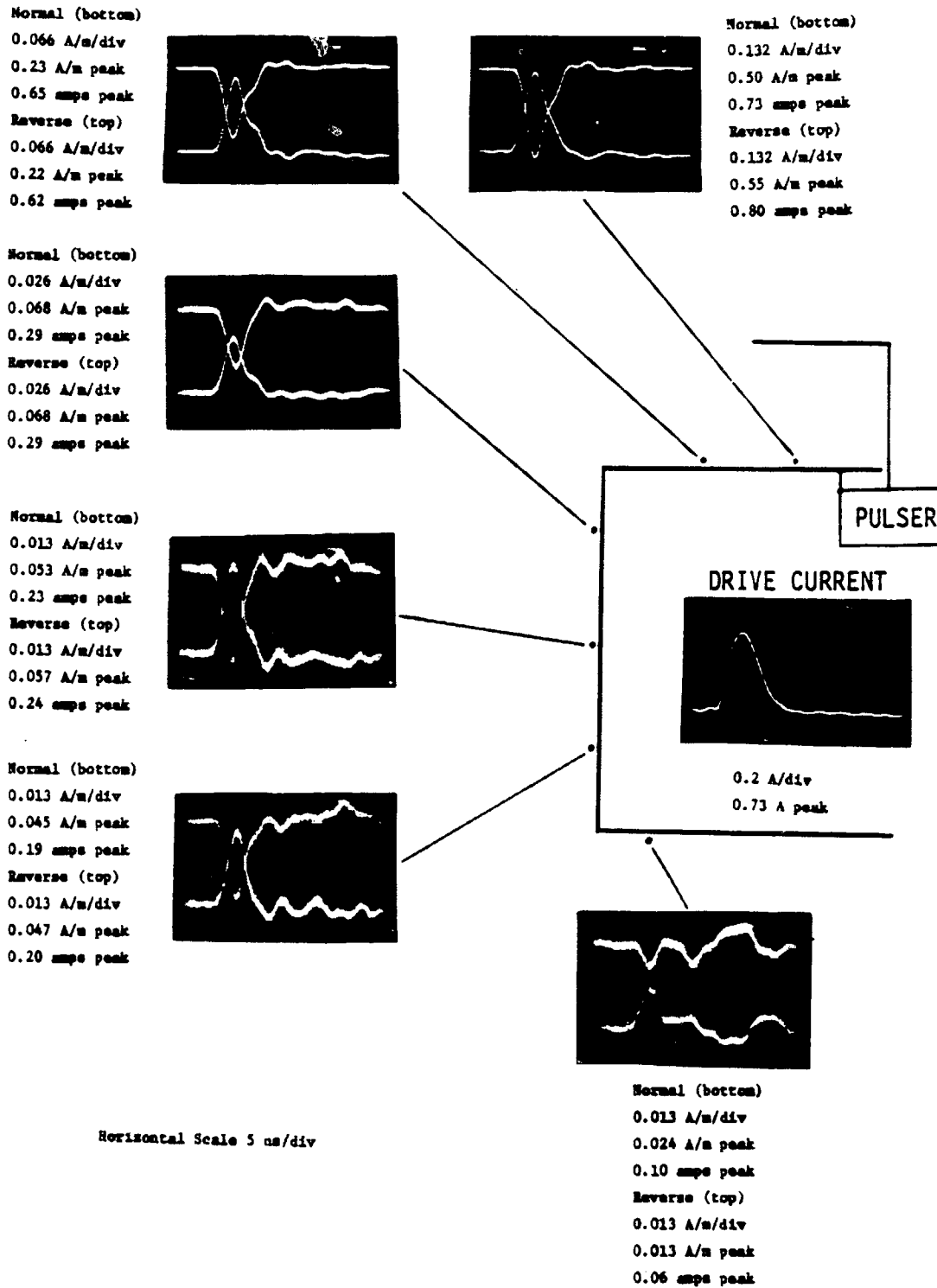


Figure 69. Solid cylinder - current drive H-fields for 0.3 m plate height

Table 6. Data Set for CDI and Blowoff

Plate Sep. (m)	I_p/τ_p (10^7 A/s)	Measured Peak \dot{B} Sensor Response (T/s) ^a					
		1	2	3	4	5	6
0.1	57	762	102	21	18.1	13.8	6.7
0.3	14.6	240	94	29	22.5	16.3	7.8
1.0	3.4	67.5	30	11.6	9.5	7.5	3.0
		Predicted Peak \dot{B} Sensor Response (T/s) ^b					
0.35	14.6	149	62.5	45.2	20.1	18.4	
		Measured Peak H_ϕ Sensor Response (A/m) ^{a,d}					
I_p (A)		1	2	3	4	5	6
0.1	1.7	1.6	0.31	0.056	0.045	0.037	0.013
0.3	0.73	0.53	0.23	0.068	0.055	0.046	0.019
1.0	0.34	0.25	0.13	0.056	0.047	0.035	0.016
		Predicted H_ϕ Sensor Response (A/m) ^{c,d}					
0.35	0.73	0.58	0.20	0.080	0.059	0.041	

^a Average of peak positive and negative polarity injections.

^b ABORC calculation scaled to $I_p/\tau_p = 1.46 \times 10^8$ A/s.

^c ABORC calculation scaled to $I_p = 0.73$ A.

^d To convert the H data to currents in amps multiply the sensor of values by $(\pi)(0.46)=1.44$, those for sensor 2 by $(\pi)(0.92)=2.9$, and those for sensors 3 through 6 by $(\pi)(1.36)=4.27$.

PRECEDING PAGE BLANK NOT FILMED

5. DATA EVALUATION

5.1 INTRODUCTION

The objective of the CAN tests was to develop a data base describing the external response of a simple satellite-like object to electron-induced discharges to provide an experimental basis for the development of an electrical simulation test. In order to have confidence in making this translation, four factors must be considered:

1. Are the simulation conditions realistic in terms of environment and effects produced?
2. What is the magnitude of the responses produced in a worst-case sense--important in developing a qualification procedure?
3. How can one infer the behavior of similar objects under other exposure conditions, containing different materials and configurations; i.e., the question of scaling?
4. How well do proposed or presently utilized electrical test procedures simulate the external response of a spacecraft to EID?

The first question has not been addressed in these tests. The complex environment of electrons, ions, and UV has been abbreviated in choosing a simulation based on monoenergetic electrons of energy ~ 10 to 20 keV, the component which is of primary importance in the charging of surface spacecraft dielectrics. However, data does exist for the effect of some components of the environment on discharges (Refs 34,37) which will be discussed in the next section of this report. Emphasis is focused in this section on items 2 and 4; i.e., relating the response of the test object to EID of specified magnitudes for different dielectrics. These data are compared to a simple response model, first described in Reference 1 and elaborated in Reference 44 in which the primary response of the object is due to the replacement currents generated by the motion of blowoff charge in macroscopic fields whose sources are the charged dielectrics as well as the emitted space charge.

A convenient means of tracking the motion of blowoff charge for particular configurations is to employ an SGEMP code which solves the Maxwell-Lorentz equations to produce a self-consistent description both of charged particle motion and of the resultant fields in the vicinity of and on the surface of the test object. Given adequate source terms and discharge emission characteristics, such codes can be used to predict the structural response for simple generic configurations. While some information about the discharge process has been inferred from the experimental data, the emphasis of this study has been on bounding the effects produced by discharges.

The electron spraying test data and models are compared to the response produced by electrical simulations of canonical discharge processes; i.e., punchthrough-flashover and blowoff. This comparison is based on data taken on the same test object during the earlier program described in References 1 and 39. Because the pulse widths of the electrical excitations were significantly shorter than those observed for EID induced in the same object, it has been necessary to scale these results based on a parallel analysis of the electrical response of the object using the SGEMP codes SABER (Ref 45) and ABORC (Ref 38) in which the measured electrical excitations were inserted as current sources. It is to be emphasized that no new ab initio calculations in which the inferred EID source terms were employed with an SGEMP code to predict the response of the CAN were performed for this analysis. Such calculations should be carried out to provide the most accurate basis for validation of the response model described below, and for the most accurate comparison between electrical test data and EID data.

5.2 DISCHARGE COUPLING

The discharge coupling model employed to interpret the observed response of the CAN was originally developed during the first phase of this program when it was realized that the blowoff of charge produced a much larger response in a satellite structure per amp of discharge current than that evoked by flashover or punchthrough. This has also been discussed in Reference 46. As more experimental evidence became available, the model was refined by Wenaas and Woods (Ref 44) by incorporation of realistic discharge pulse shapes and emission characteristics for discharges in meter-sized dielectrics characteristic of those found on spacecraft.

The model is phenomenological in the sense that it relies on experimentally determined parameters to provide source terms; i.e., the time and spatial history of the emission current which represents the discharge. The model assumptions include:

1. When a differential potential V_B is reached a discharge occurs and charge is released. A fraction f_B of the total trapped charge is blown off, a fraction f_P punches through the dielectric, and fraction f_f flashes over. When the potential difference reaches some lower value V_f the discharge ceases.
2. The effect of the flashover and punchthrough discharges are only to decrease the surface potential during the discharge.
3. The emission pulse width and amplitudes are assumed to scale with the dielectric linear dimensions. This constant of proportionality is supposed to relate to a material-dependent "velocity of propagation" for the discharge process (q.v. Ref 47); however, this assumption is not essential to the model predictions. One can accept such scaling as an experimentally determined fact. The scaling laws are used for guidance. The most accurate response calculations employ the discharge characteristics for the object determined by low impedance measurements.
4. Blowoff charge is emitted with essentially zero initial energy and uniform spatial emission. Based on assumption 3 above, but also on experimental observation, the emission current waveform is assumed to be triangular. A significant finding of EID measurements on large-area, meter-sized dielectrics is that the basic discharge pulse is relatively slow rising and wide (μs), rather than fast rising and narrow (ns). The emission model chosen is one of the more controversial assumptions of the model. Other emission models have been proposed based on space-charge-limited emission enhanced by the steep potential gradients found at the interface between dielectric and conductors (Refs 47-49). Uniform spatial emission, or even symmetric emission is a calculational artifice as the surface potential scans reveal the discharge patterns to be irregular and influenced by edges and seams.
5. The motion of the emitted particles are tracked using an SGEMP code until they reach a conducting boundary, i.e., the tank walls or the sides of the CAN where they are absorbed. It is assumed that any emitted electrons which are returned to the surface of the dielectric because of space-charge limiting are specularly reflected; i.e., the dielectric surface albedo of 1. This permits electrons which would be returned to the dielectric during space-charge-limited emission to be laterally accelerated along the surface of the

dielectric and then off, in a manner similar to the edge potential gradient enhanced emission described in References 47 and 48. Such a postulate is necessary to satisfy exponentially observed emission scaling laws (Ref 33), namely: I_p , the peak amplitude of the blowoff current, is approximately proportional to the square root of the sample area. The pulsewidth or rise time τ_p is similarly proportional to the square root of the sample area. The blowoff charge is proportional to sample area for samples with linear dimensions as large as 1 m and possibly larger.

It is to be noted that these scaling laws have been inferred for the most part from the response of unbroken, circular samples, usually held in place with grounded edge clamps.

6. The material-dependent blowoff source terms, I_p , τ_p , and f_B , V_B can be derived from measurements on grounded samples. The implication is that for samples of the types considered and areas up to 1 m^2 , space-charge limiting of emission is not significant. The emitted charge all escapes to the tank walls. The return current which flows up the ground strap connecting the CAN to the tank is essentially identical to the blowoff current waveform.

The experimental data, primarily in the form of \dot{H}_0 and return current measurements were compared to the responses predicted in two previous calculations based on the emission model. One modeled an isolated CAN in free space excited by a blowoff discharge pulse whose shape was triangular, with a rise time of 10 ns, and a peak emission level of 10^{-5} A/m^2 , kept sufficiently low to avoid space-charge limiting. This calculation, reported in Reference 1, was made during the first phase of this program in order to compare the responses produced by a blowoff discharge, arc discharge and CDI simulations.

The second comparison was made by extrapolating the predicted response of a similar cylindrical object described in Reference 37 under essentially identical exposure conditions to those to which the CAN was subjected. In both cases, comparison was made by scaling the calculated results by the relevant (I_p/τ_p) ratios. The EID data reported in Reference 37, as well as the electrical excitation data reported in Reference 1, support this ansatz, at least over a limited range of extrapolation. In both cases, the two-dimensional ABORC SGEMP code was employed. Both the model calculations reported in Reference 37 also correspond to the isolated case as the JAYCOR test object was connected to ground by a $1 \text{ M}\Omega$ resistor.

The electrical test data was modeled using the measured discharge current terms as the drivers in the calculations made with the fully self-consistent, three-dimensional SGEMP code SABER. A detailed discussion of the models employed and the computational procedure is presented in Section 6 of Reference 1 and briefly reviewed in Section 5.4 of this report in which scaled electrical test data is compared to the EID experimental results.

In comparing the data and predictions some care must be taken. For example, the H_0 , \dot{H}_0 , and I_r data have been reported both here and in Reference 37 as peak values. Response scaling has been made with I_p/τ_p , the average rate of rise of the discharge current pulse. For triangular discharge pulses, and to the extent that the body currents show the same shape as the emission current, such scaling is reasonable. However, the real H_0 pulses look more gaussian (albeit with unsymmetrical rise and fall times) while the \dot{H}_0 pulses tend to look like the derivative of a gaussian rather than the square wave shape, the derivative of a triangle. For a gaussian current pulse, $\dot{I}_{\max} \approx 1.4 I_p/\tau_p \approx 1.4 I_p/W_{1/2}$, where $W_{1/2}$ is the half maximum pulse width. A second factor is that the discharge pulse excites a relatively wide component (ca. few microseconds) on which is superimposed lower amplitude but high frequency oscillations. These oscillations, which on the average add little to the magnitude of $H_0(t)$, can significantly increase the observed amplitude of $\dot{H}_0(t)$. Finally, the amplitude of the discharge pulses and the corresponding body replacement currents show a range of values corresponding to the statistical nature of the discharge process. Therefore, in comparing the experimental data to model predictions, we have used average experimental values based on the ensemble of large amplitude response data.

5.3 DATA COMPARISON

5.3.1 Kapton

The first significant point to be made in evaluation of the Kapton discharge data is that the discharges are nonuniform, being concentrated along the region of overlap of the two sheets of tape. It is evident from the surface potential maps (Figures 28 and 29) that the bulk of the charge removed in discharge is in the region of this seam or adjacent to it. This observation explains why the net fraction of charge removed in large amplitude discharges is less than 0.1 rather than the 0.3 reported in Table 1 of Reference 34 for a uniform circular sample with grounded edges. This is shown clearly in Figure 70.

ORIGINAL PAGE IS
OF POOR QUALITY

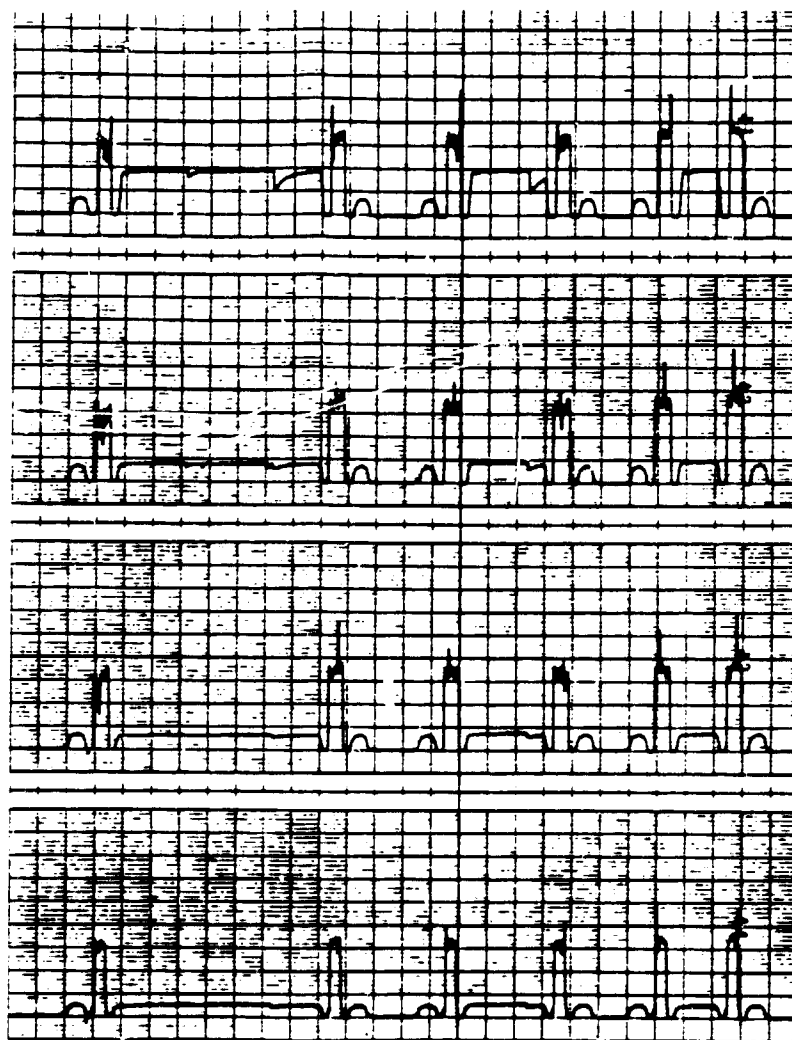


Figure 70. Surface potential scan of Kapton, grounded configuration, $E_i = 20$ keV showing an edge discharge along the seam joining the two pieces of tape

The charge accounting supports this observation. The peak surface potential in the region of the seam is 15 kV as compared to the 9 kV average elsewhere. As the capacitance per unit area of two layers of tape is, to a first approximation, one-half that of the single tape layer, the average charge per unit area is $q(\mu\text{C}/\text{cm}^2) \approx (0.79) \cdot (14/9) \cdot (5) = 2.46 \mu\text{C}/\text{cm}^2$. As the area of the overlapped region is 380 cm^2 , the total stored charge in it is approximately $(380) \times (46) = 935 \mu\text{C}$.

The surface potential scans indicate that for discharges occurring along a seam, the average potential of the rest of the sample does not change significantly. Thus $\Delta Q \approx (934) \cdot 5/14 \mu\text{C}$ or about $333 \mu\text{C}$. If $f_B \sim 1/3$, the net amount of charge blowoff is about $111 \mu\text{C}$. Based on the integrated \dot{B} data, the blowoff charge is between 120 and

ORIGINAL DOCUMENT
OF POOR QUALITY

208 μC in reasonable agreement with the surface potential information, especially if one allows for some loss of charge in the region outside but adjacent to the overlap.

Thus, one must be careful in applying scaling laws to real dielectric structures based on the response of unsegmented, grounded edge samples. Real spacecraft dielectrics are frequently segmented, wrinkled, layered or otherwise irregular.

The dynamic response data and calculations for Kapton are summarized in Table 7. This table and the corresponding tables for the other materials are organized as follows. The sensor locations for which calculations are presented correspond to the original B sensor positions on the CAN during the arc discharge experiment described in Section 4.5.2 and shown in Figure 65. Of course, for the EID tests, there were no sensors at the same radius as #1 which fell inside the boundary of the dielectric samples. Assuming cylindrical symmetry, sensor position 2 in the table was equivalent to sensors 1 through 4 shown in Figure 13. Sensor position 3 was equivalent to sensors 5 and 8, sensor position 4 was equivalent to sensors 6, 9, 11 and 12, while sensor position 6 was equivalent to sensors 7 and 10.

Table 7. Summary of Kapton Surface Current Data

Data	Sensor Position				Units
	2	3	4	5	
<u>Experimental</u>					
\dot{H}_0 (G ^a)	4-8 {5.3}				10^7 A/m/s
\dot{H}_0 (HI ^b)	8 {8}				10^7 A/m/s
Body Currents (G)	22-38				A/m
Body Currents (HI)	~ 47				A/m
<u>Calculated</u>					
\dot{H}_0 (Scaled Phase 1) ^c	0.7				10^7 A/m/s
\dot{H}_0 (Scaled Ref 37)	1.5				10^7 A/m/s
Scaled Body Currents ^d	17	12.5	6.2	1.8	A/m

^aG = grounded

^bHI = High Impedance, $R_L = 10^6$ ohms.

^cScaled for $1/\tau_p = 105 \text{ A}/1.6 \mu\text{s} = 6.6 \times 10^7 \text{ A/s}$.

^d $\dot{H}_0 = \dot{H}_0 \tau_p / 1.4$, $\tau_p = 1.6 \mu\text{s}$.

The experimental data tabulated includes the peak \dot{H}_0 for the grounded and high-impedance configurations for the corresponding \dot{B}_0 sensors. Shown on both the range of \dot{B} values converted from Teslas/second to \dot{H}_0 in amps/meter/second using the relationship $B(\text{T/s}) = \mu_0 H(\text{A/m/sec})$ where $\mu_0 = 4\pi \cdot 10^{-7}$. The median value for each sensor is

enclosed by the brackets $\{ \}$. Also given are peak body currents in A/m obtained by integrating the \dot{H}_ϕ data.

The theoretical response called "Scaled Phase I" was based on the original IRT ABORC calculations scaled by the average (I_p/τ_p) ratio. The predicted peak \dot{H}_ϕ responses based on the JAYCOR calculations described in Reference 37 were extrapolated from the corresponding data in that report based on the relevant ratios of I_p/τ_p . The fact that the two objects have slightly different diameters, 0.91 m for the JAYCOR object versus 1.36 m for the CAN, was taken into account. The predicted axial body currents are similarly scaled. Also shown in the range in values of H_ϕ or axial surface current response obtained by integration of the \dot{B} sensor data. Such integration has the effect of smoothing out the high frequency oscillations. By assumption (6), $H_\phi(t)$ for the CAN grounded to the tank is related to the blowoff current pulse $I_p(t)$ by $I_p(t) = H_{\phi i} 2\pi r_i$ where $H_{\phi i}$ refers to the response at the i^{th} sensor position located at a distance r_i from the axis of symmetry of the CAN. The net I_p/τ_p for Kapton was calculated from the mean of $(\{H_{\phi 2}\} \cdot 2\pi r_2)/\{\tau_p\}$ where $r_2 = 0.54$ m and $\tau_p = 1.6 \mu\text{s}$. It can be seen that the value of $\dot{H}_{\phi 2}(\text{max}) \approx 1.4 \{H_{\phi 2}\}/\{\tau_p\} = 2.6 \times 10^7$ A/m/s, assuming that the basic H_ϕ pulse is approximately like a Gaussian as the experimental data indicates. This is a factor of two less than $\{\dot{H}_{\phi 2}(G)\}$. The difference is a measure of the increase in the peak amplitude of \dot{H}_ϕ because of the contribution of the high frequency data.

The high frequency oscillatory component is assumed to be an undamped sinewave with a period of 50 MHz. (Based on an evaluation of many \dot{B} photos, it is clear that the frequency of this component has between 50 MHz and 70 MHz.) Then its amplitude is

$$8 \times 10^7 \text{ A/m/s} - 2.6 \text{ A/m/s} = H'_{\phi 2} \omega = 5.4 \times 10^7 \text{ A/m/s} ,$$

where $H'_{\phi 2}$ is the amplitude of this component of surface current. As $\omega = 2\pi \cdot 5 \cdot 10^7$, $H'_{\phi 2} = 0.17$ A/m, less than 1 percent of the intensity of the principal component of body current.

From the data in the table, it can be seen that the predicted peak rate of change of surface magnetic fields for the high impedance case is a factor of ten lower for the scaled IRT Phase I calculations and about a factor of five lower for the JAYCOR calculations. Some, but not all, of the observed discrepancy can be attributed to the presence of higher frequency discharge components. The model calculations yield B or H as a function of position. Numerical differentiation of the predictions is performed

to obtain \dot{B} or \dot{H} . In this process much of the fine structure information is lost. Even if the estimated peak high frequency contribution of ca. 3×10^7 A/m is subtracted from the experimental values, the agreement is still poor. As no relative Kapton data was recorded for sensor positions 3 through 5, it cannot be determined whether the predicted falloff of \dot{H}_ϕ as a function of distance from the top of the CAN is observed. There is better agreement between the predicted peak body currents and experiment if one uses the JAYCOR scaled \dot{H}_ϕ data and the observed waveform to obtain τ_p . This question will be discussed in more detail in the next section of the report in which the Teflon data is evaluated. One point may be noted, that is that the values of \dot{H}_ϕ calculated depends sensitively on the detailed source pulse shape chosen. As Figure 16 of Reference 37 indicates, choosing a triangular emission pulse yields consistently low values for \dot{H}_ϕ (by factors of two to four for their data) for sensor positions near the discharging dielectric.

5.3.2 Teflon

It is evident from the discharge photographs (Figure 36) that the Teflon tape edges, whether butted or lapped, serve as discharge foci. However, during a discharge most of the surface loses charge, unlike the behavior of the Kapton sample. This is clear from the surface potential scans for Teflon shown in Figures 38 to 40. The amount of charge lost in large discharges, $Q_{tot} \approx 60$ to 80 percent of the total or ca. $600 \mu\text{C}$ (q.v. Table 4). If one assumes that the replacement current which flows in the ground strap during a discharge with the CAN grounded to the tank monitors the blowoff current, then the data presented in Table 8 indicates that the net blown-off charge for large discharges averages ca. $160 \mu\text{C}$. Thus, the fraction of charge blown off is about 0.2 of the total trapped charge.

The calculated and measured \dot{H}_ϕ , H_ϕ and return current data are summarized in Table 8. For the experimental data both the range of values and the mean for the ensemble of large amplitude pulses are again given. If the blowoff current is truly mimicked by the return current in the grounded configuration, then one expects that $\dot{H}_{\phi(\text{peak})}$ at Sensor 2 should average 3.7×10^7 A/m/sec and $H_{\phi(\text{peak})}$ on the sides will be about 2.9×10^7 A/m/sec.

It can be seen that there is reasonably good agreement between the integrated \dot{H}_ϕ values at sensor Positions 2, 3, and 4 and the return current. The computed values of $\dot{H}_{\phi 2}(G)$ and $\dot{H}_{\phi 3}(G)$ are about a factor of two to four lower than observed, while the

ORIGINAL PAGE IS
OF POOR QUALITY

Table 8. Summary of Teflon Response Data

Data	Sensor Position				Units
	2	3	4	5	
<u>Experimental</u>					
\dot{H}_0 (G ^a)	3.2-12 (8)	2.3-3.1 (2.6)	3.2-4.3 (3.7)		10 ⁷ A/m/s
\dot{H}_0 (H ^b)	1.5-23 (20)	4.1-5.1 (4.6)	4.0-25 (12)		10 ⁷ A/m/s
Body Current (G)	98-250 (173)	58-110 (85)	70-150 (110)		A
Body Current (H)	98-215 (140)				A
Return Current (G)		60-150			A
<u>Calculations</u> ^{c,d}					
\dot{H}_0 - Phase 1 Scaled	1.0	1.0	0.55	0.43	10 ⁷ A/m/s
\dot{H}_0 - Ref (37) Scaled	2.1	1.5	0.77	0.46	10 ⁷ A/m/s
Scaled Body Currents	41 ^c	34	13	7.4	A

^aG = CAN grounded.

^bH = High impedance, CAN connected to ground through 1 M Ω resistor.

^cScaled for $I_p/\tau_p = 115 \text{ A}/1.3 \mu\text{s} = 9 \times 10^7 \text{ A/s}$.

^dCalculations for high impedance case.

^e $I_p = \tau_p \cdot \pi(1.36) \dot{H}_\phi/1.4$, where $\tau_p = 0.56 \mu\text{s}$.

^fAt $d = 1.08 \text{ m}$.

ratio for $\dot{H}_{\phi 2}$ (HI) is more like a factor of ten. The difference between the calculated and observed values of $\dot{H}_{\phi 3}$ (HI) is a factor of 3 and for \dot{H}_ϕ (G) and $\dot{H}_{\phi 4}$ (HI) are more like a factor of 10.

There are several possible reasons for this discrepancy. These include:

1. The model assumes that in the grounded configuration, the replacement currents and return currents mirror the blowoff pulse. If, in fact, the blowoff pulse had a sharper rate of rise than that observed for the return current, then this would be reflected in the \dot{H}_ϕ data. The grounded SSM data shown in Figure 13 of Reference 37 shows a similar trend as our data; i.e., larger than expected peak \dot{H}_ϕ signals as one approaches the top of the CAN.
2. It is clear from the \dot{B} data that there is a significant high frequency component in these pulses which increases the peak amplitude of the grounded CAN \dot{B} data by as much as 50 percent and the high impedance amplitudes by a factor of two or more. The high frequency component is observed in all the \dot{B} data with a period relatively independent of the dielectric in which the discharges are produced. Examination of time-expanded photographs of typical \dot{B} data implies that the frequency of this component is 65 to 70 MHz. Ringing of the CAN at about this frequency was

also observed during the arc discharge testing reported in Reference 1. It is believed that this mode of oscillation is related to the lowest order circumferential mode of response of the CAN, which for this 1.36 m diameter cylinder is about $c/\lambda = 3 \times 10^8 \text{ m/s} \div \pi(1.36)\text{m}$ or 70 MHz. These oscillations are excited by the high-frequency component of the axial replacement currents which flow along the surface of the CAN as a consequence of the blowoff of charge. In order to produce an oscillation where amplitude is 50 percent of the mean of the grounded configuration \dot{B} data and is a factor of two larger than that for the high-impedance data requires a high-frequency component of about 0.1 A/m and 0.22 A/m, respectively. In both cases these are less than 1 percent of the amplitude of the principal component of the discharge current.

In the case of Sensor Position 4 (High Impedance), the response is one of ringing in which two predominant frequencies can be resolved. One is the 65 to 70 MHz oscillations discussed above, while the second has a frequency of 10 to 13 MHz. The latter component was observed in all the high-impedance data, especially on the return current signals and is probably associated with the oscillation of the coupled system comprised of CAN, ground straps and tank. If we assume that the ringing during the discharge is comprised primarily of oscillations of the 70 MHz component, then $H_{\phi 4} \approx 0.1 \text{ A/m}$, a relatively small current compared to the predicted values of 13 A/m. If it were entirely due to the 13 MHz component, then the corresponding $H_{\phi 4} \approx 1 \text{ A/m}$.

3. The model calculations for the high-impedance configuration predict that the measured body currents should be significantly less than the blowoff currents and show a decrease in amplitude as the sensor position falls further toward the bottom of the CAN. This is a consequence of space-charge limiting of the emission current in the high-impedance case. Because the RC time constant is ca. 100 μs , where $R = 1 \text{ megohm}$ and $C \approx 100 \text{ pf}$, the CAN should have been isolated from the tank for a period long compared to the discharge pulse widths of 1 to 5 μs . In this case, space-charge limiting should have occurred relatively quickly. If $I_p/\tau_p = 9 \times 10^7 \text{ A/s}$, then it will take approximately 160 ns for 1.2 μC of charge to be emitted. This will raise the potential of the CAN relative to the tank wall to $\approx 12 \text{ keV}$, after which time charge is returned to the top, edges and sides of CAN, albeit after traveling

distances comparable to a CAN dimension (c.f. Figures 3 and 4 in Reference 47). Both the measured body currents at sensor position 2 and all of the H_{ϕ} data in the high-impedance case are significantly higher than predicted. Some of the discrepancy can be accounted for by the contributions of higher frequency components not accounted for in the model. The H_{ϕ} predictions of the model calculations depend resistively on the assumed characteristics of the discharge, i.e., pulse shape, energy and spatial distribution of the blowoff particles and the configuration and surface albedo of the dielectric and conducting portions of the test object. The emission of blowoff could have significantly different characteristics than those assumed in the model or inferred from the measured return currents. The model calculations are themselves only extrapolations from cases which differ in significant aspects such as emission pulse widths and amplitudes (IRT Phase I) and sample geometry (JAYCOR) from the case at hand.

4. However, the most likely reason for the large divergence between HI predictions and test data lies elsewhere. The maximum potential attainable by the CAN relative to the tank is the average predischARGE potential difference between the electron-charged dielectric and CAN (assuming that blowoff electrons are emitted with essentially zero emission energy). For Teflon, the data of Table 4 indicates that this value is ca. 12 keV. Thus, the maximum current to be observed flowing through the 1 M Ω resistor is $1.2 \times 10^4 / 10^6 = 12$ ma. In fact, return currents observed were bipolar (+,-) and up to 5 A peak. This indicates that there was a breakdown of the resistor during discharge so that its effective resistance was significantly less than $10^6 \Omega$, perhaps as small as $12 \text{ kV} \times 10^4 / 5 \text{ A} = 2400 \Omega$. It is most likely that surface flashover occurred, as subsequent dc testing of the resistor indicated no permanent damage. Under these conditions the CAN would only be isolated from ground until breakdown occurs, after which time further charge could be blown off. Thus, the observed discharge was probably more characteristic of the low impedance than of the isolated case. If this were true, one would expect to see the large body currents typical of the response of a grounded CAN.

However, there were significant differences between the response in the high-impedance configuration and that for the grounded case. These include the observed bipolar rather than positive return current and the consistently

positive blowoff current. The blowoff current collected as a result of discharges for a grounded CAN covered with Teflon were typically +1.2 to +3 A peak, 0.5 to 1 μ s in width, containing about 1.6 μ C of charge. If one assumes isotropic emission of blowoff charge which all reaches the wall, then geometric considerations imply that about 126 μ C of charge is emitted on the average. This compares reasonably well with the return current data which implies emission of about 160 μ C. The amount of charge blown off in the high-impedance case is about 1 μ C on the average (<2 A, 0.5 μ s half maximum width).

5.2.3 Solar Array Mockup

The size of the discharges occurring in the solar array mockup was relatively small, even allowing for the smaller size of this panel compared to those containing Kapton or Teflon. This is not surprising as the panel was built out of 2 cm x 4 cm tiles so that there was a larger perimeter to total surface area than in the other samples. As the discharge photographs indicated, edges play an important role in discharge initiation. The surface potential data indicate that a significant fraction of the coverslips participate in a discharge. However, the net charge fraction involved is only about 0.2 for the largest discharges, rather than the 0.5 to 0.8 for other samples. Most discharges were much smaller, averaging about 0.05. The mean charge released by blowoff is about 20 μ C to 60 μ C, corresponding to an f_B of 0.04 to 0.1 in the largest discharges.

Response data is compared to the scaled model predictions in Table 9. If the return current can be taken to represent the blowoff current in the grounded configuration then one expects to see body surface currents of the order of 4.5 A/m at sensor position 2 and 3.6 A/m at sensor positions 3, 4 and 5. Because of the predominance of high-frequency ringing in the \dot{B} sensor data, it was hard to numerically integrate them. However, integration of a very limited amount of digitized data (q.v. Figure 58) indicates that the measured surface currents are comparable to those predicted.

The corresponding predicted mean values for \dot{H}_0 are up to a factor of ten lower than observed. It can be seen that the measured responses are a factor of 2.5 higher. This difference is largely due to the presence of significant high-frequency components in the CAN response. These components are more predominant in the mock solar array discharge because of their relatively small magnitude if compared to those associated

Table 9. Solar Array Mockup Response Data

Data	Sensor Position				Units
	2	3	4	5	
<u>Experimental</u>					
\dot{H}_ϕ (G ^a)	0.7-3 (1.2)	0.47-1.0 (0.90)	0.64-1.7 (0.89)		10 ⁷ A/m/s
\dot{H}_ϕ (H ^b)	0.25-5.8(2.8)	0.52-1.1 (0.89)			10 ⁷ A/m/s
Body Current (G)	4.0				A/m
Body Current (H)	3.4				A/m
Return Current (G)		7.5-50 (15.4)			A
<u>Calculations</u> ^{c,d}					
\dot{H}_ϕ - Phase 1 Scaled	1.4	1.5	0.79	0.62	10 ⁶ A/m/s
\dot{H}_ϕ - Ref (37) Scaled	2.8	2.0	1.0	0.61	10 ⁶ A/m/s
<u>Measured Wire Currents</u>					
	C1(G) 1.6-8.8 (2.2)		C2(G) 0.7-3 (1.2)		A
	C1(H) 2-3 (2.3)		C2(H) 1.1-1.7 (1.4)		A

^aG = CAN grounded.

^bH = High impedance, CAN connected to ground through 1 M Ω resistor.

^cScaled for $I_p/\tau_p = 15.4 \text{ A}/1.27 \times 10^{-6} = 1.2 \times 10^7 \text{ A/s}$.

^dCalculations for high impedance case.

with Teflon or Kapton. For low-impedance discharges, the predominant hf component has a frequency of 50 to 67 MHz which we have attributed to the excitation of the lowest order circumferential mode of the CAN. In addition, there is also a component with a frequency of 6.7 MHz attributed to the response of the CAN, ground strap and tank and determined primarily by the capacitance of the CAN to the tank and the (unmeasured) inductance of the ground strap which is estimated from $f = 1/2\pi(LC)^{-1/2}$ to be about 6 μHy . If the difference between the measured and predicted \dot{H}_ϕ (which is about $7.5 \times 10^7 \text{ A/m/s}$) is due entirely to high-frequency oscillations, this implies that the intensity of the high-frequency surface current component is about 0.17 A/m, less than five percent of the amplitude of the predominant surface current component. It is to be noted that the return current signal also shows evidence of the 6 to 7 MHz oscillation.

The observed peak amplitude of the \dot{H}_ϕ data for the high-impedance responses are five to ten times larger than predicted by the scaled calculations. Much of this discrepancy can be attributed to the contribution of the high-frequency oscillations. These oscillations dominated the \dot{B} response in that it was difficult to obtain H_ϕ by integration.

Again, it is not clear that it is valid to compare the observed \dot{B}_ϕ or (\dot{H}_ϕ) data and that predicted for the high-impedance configuration. The observed return current pulses were bipolar (+,-) as they were for Teflon, rapidly rising, reaching levels of ca. 2 A in 100 to 200 ns. This implies that the $10^6 \Omega$ resistor again broke down during these measurements. If current were emitted at 1.2×10^7 A/s, then full space-charge limiting (CAN at +10.5 keV) would have occurred within about 400 ns, at which time the effective impedance of the series resistor would be $10 \times 5 \text{ kV} / 2 \text{ A} = 5.5 \text{ k}\Omega$.

5.4 COMPARISON OF ELECTRICAL EXCITATION WITH EID

The primary objective of the CAN experiment was to obtain data on the external response of a simple satellite-like structure to electron-induced discharges produced in dielectric surface materials. These data are to serve as a baseline for developing the proposed electrical simulation procedure to be incorporated in the MIL-STD 1541 draft. It was decided that the response factor which would be used for comparison would be the skin or surface replacement currents generated on the test object excited either by EID or electrically as these are of primary importance in the coupling of discharge energy into the interior of the spacecraft. Other response characteristics such as the normal electric displacement field (D_n) could also have been used, as it is in some cases important to subsequent coupling processes. This quantity is related to the surface charge density through Poisson's equation just as the tangential magnetic field H_t is related to surface current for the conditions of interest here (Ref 50).

During the first phase of the program, data was obtained for the response of the CAN to an arc discharge simulation. These data are presented in Section 4.5.2. Similarly, the response to CDI excitation as a function of plate spacing was also determined. The CDI data are presented in Section 4.5.3. At the time when these tests were performed (1977-1978), little was known about the characteristics of EID in regard to both source terms and the resultant fields generated. The exciting pulse widths of ca. 40 ns for the arc discharge and 10 to 30 ns for CDI were determined largely by pulser characteristics, rather than hard data. This was not felt to be a significant limitation at that time because available data on other kinds of discharges implied comparable pulse widths. Nor was much significance placed on pulse amplitude as the linearity of Maxwell's equation permits scaling between the responses produced by pulses of different amplitudes.

To permit comparison between the responses produced by different exciting sources, a series of model calculation were performed to evaluate the best means of

scaling the experimental data. These calculations are described in detail in Reference 1. Three cases were considered. That for an isolated CAN excited by EID has been discussed in Section 5.2. The second calculation was for a CDI excitation of the CAN with a 69 cm drive plate located on top of the object at a spacing of 35 cm. The drive pulse was triangular, 1 A peak and with rise and fall times (τ_p) of 10 ns. The calculations are in excellent agreement with the experimental data presented in Table 6, largely because the test setup could be accurately modeled, and because the source term is close to that observed experimentally. The third calculation modeled the arc discharge process. The experimentally measured discharge waveform shown in Figure 66 was used as a source term. Because the thin capacitor could not be modeled exactly with a SGEMP code, two scaling laws were examined to relate the model calculations to the experimentally determined \dot{B} data. One was based on I_p/τ_p , the peak rate of rise of the discharge source. The second was based on \dot{V}_p scaling, the peak rate of change of the surface potential on the top of the CAN. As the data of Table 5 indicate, I_p scaling gives closer agreement with experiment. These results, plus an identical finding in regard to the response of a similar object to EID reported in Reference 37, provide a rule for comparing the CAN \dot{B} and H responses produced by the various exciting sources.

The experimental \dot{B} data for the CAN is summarized in Table 10. For comparison between electrical excitation and EID, the data has been normalized to $I_p/\tau_p = 10^8$ A/s, characteristic of the emission rate for the blowoff discharge of meter-sized dielectrics. Also included are the scaled theoretical calculations. Because the experimental data is \dot{B}_ϕ , the calculated responses (H_ϕ) were numerically differentiated for comparison. The calculated B_ϕ or H_ϕ pulse shapes generally followed the exciting source wave form. This was also observed for the experimental electrical and integrated EID \dot{B}_ϕ data.

Table 11 summarizes the normalized H_ϕ data. The electrical and EID surface current data were normalized to a response produced by a 100 A peak source. Such scaling with I_p is reasonable for the electrical test data because of the linearity of Maxwell's equations. Since space-charge limiting of emission must invalidate unrestricted linear response scaling for isolated objects, except for very small emission currents or over relatively narrow ranges of peak current, a normalization value of I_p was taken which is characteristic of the blowoff currents in meter-sized spacecraft dielectrics and also consistent with $I_p/\tau_p = 10^8$ A/s used to normalize the \dot{B} data.

ORIGINAL PAGE IS
OF POOR QUALITY

Table 10. Normalized \dot{B}_ϕ Data

	Sensor Response (Teslas/sec)				
	1	2	3	4	5
<u>Experimental</u>					
CDI (0.1 m)	134	18	3.7	3.2	2.4
CDI (0.3 m)	164	64	20	15	11
CDI (1.0 m)	199	88	34	28	22
Arc Discharge (180°) ^b	1.6	0.31	0.038	0.031	0.034
Kapton (G) ^c		100			
Kapton (HI) ^d		152			
Teflon (G)		111	36	52	
Teflon (HI)		279	64	167	
Mock Solar Array (G)		126	94	93	
Mock Solar Array (HI)		293	93		
<u>Theoretical^e</u>					
CDI (0.35 m)	102	43	31	13	9.0
Arc Discharge	2.2	0.38	0.066	0.029	0.020
IRT Blowoff	8.8	13.3	14	8.3	6.0
JAYCOR Blowoff		22.6	21	10	6.1

^aNormalized to $I_p/\tau_p = 10^8$ A/s

^bAverage of F.O. and hardware data

^cG = Grounded configuration

^dHI = High impedance configuration

^eCalculations scaled by I_p/τ_p

Table 11. Normalized Experimental H_ϕ Data^a

	Sensor Response (A/m)				
	1	2	3	4	5
CDI (0.1 m)	94	18	3.2	2.6	2.2
CDI (0.3 m)	73	32	9.3	7.5	6.3
CDI (1.0 m)	74	38	16	14	10
Arc Discharge (180°)	1.2	0.25	0.03	0.024	0.026
Kapton (G) ^b		28			
Kapton (HI) ^c		44			
Teflon (G)		44	17	22	
Teflon (HI)		36			
Mock Solar Array (G)		26			
Mock Solar Array (HI)		19			

^aScaled to 100 A peak emission current

^bG = Ground

^cHI = High Impedance

The following remarks can be made about the data:

1. It is clear that the CDI excitation provides a fairly good simulation of the observed EID skin currents induced on the CAN if measured by the absolute magnitude and relative amplitude as a function of sensor location. Not unexpectedly, the response produced by the arc discharge is much too small, except possibly very close to the arc. With the peak \dot{B} data scaled to the same rate of rise for both CDI and EID excitation, agreement to within a factor of three or so was obtained. Some of the discrepancy in this case was due to the hi-frequency component present in the EID \dot{B} response, but not in that evoked by CDI. The agreement between the peak H_ϕ responses was at worst a factor of two and typically much better.
2. The blowoff calculation indicates that the predicted magnitude of H_ϕ and \dot{H}_ϕ should diminish as one gets closer to the center of the top of the CAN because H_ϕ is proportional to $(2r_i/d) I_0$, where I_0 is the net emission from the top of the CAN, assumed spatially uniform, r_i the i^{th} sensor radius and $d = 1.36$ m, the CAN diameter. This pattern is not well simulated by a CDI excitation as the induced surface currents increase as the distance between sensor position and drive wire decreases. Thus, the simulation is best at test object locations near and beyond the edge of the drive plate.
3. Alternation of the plate spacing can be used to change the relative amplitude of the evoked body current responses. CDI excitation was initially designed to simulate the space-charge-limited emission of x-ray-induced photoelectrons produced by SGEMP. A comparison between the electrical and EID test data indicate that the best agreement between the two occurs for a plate spacing of 1 m or possibly greater. This is not surprising as the model calculations presented in References 45 and 47 indicate that the blowoff charge can move over distances comparable to the object dimensions, even when returned to an isolated spacecraft under space-charge-limited emission. However, the relative motion of the exciting charge is not identical for CDI and blowoff as the model calculations also indicate that a significant fraction of blown-off charge is returned to the sides and bottom of the object.
4. CDI simulation of a EID as heretofore carried out produces a relatively symmetric excitation of the object. Data based on surface potential scans obtained in this program and elsewhere (Ref 51), show that discharges in real

spacecraft dielectric-containing structures may be asymmetric, concentrated in areas with an irregular surface or at edges or along seams or other dielectric boundaries as the largest transverse potential differences, which are evidently important in producing discharges (Ref 48) or largest at these places. Presumably such irregularly shaped discharges can be simulated by tailored drive plates and/or multiple drive wires, but this has not been investigated theoretically or experimentally.

5. Two low-amplitude, high-frequency components appear in the discharge data. One, with characteristic frequencies of 5 to 6 MHz (CAN grounded) or 12 to 13 MHz (CAN with 1 M Ω resistor in series with the ground strap), is attributed to the resonant response of the CAN, tank and ground strap and would not be seen during an electrical test. The second, with a characteristic frequency of 50 to 70 MHz attributed to the lowest order circumferential mode of oscillation of the CAN. It was also apparent in the \dot{B} signals produced by the arc discharge excitation but not for CDI excitation. The reason for this inconsistency is not known. Even though the CDI drive pulse is significantly narrower than the arc discharge, a Fourier transform of the CDI pulse indicates that a significant fraction of the spectral constant lies in a frequency range overlapping the resonant mode. However, the amplitude of this component is relatively low, if compared to the predominant component. Thus, it contains little of the total electromagnetic energy carried by the replacement currents. Simulation of this component is not deemed significant, although there may be spacecraft elements selectively excited by it.
6. Both the electrical test data reported in Reference 1 and the EID data reported in Reference 37 indicate that the presence of reentrant geometries such as booms or antennae will alter the object's response, especially near such structures, in a manner which is not well understood. The presence of these structures alters both the relative amplitudes and characteristic frequencies of the external surface currents. The limited amount of data available from the ground tests on the P78-2 indicate that such reentrant geometries can either serve as a discharge foci or significantly enhance the peak currents coupled into a structure above those predicted by extrapolation from the observed behavior of highly symmetric structures like the CAN.

Therefore, it is important to complete the EID testing of the SCATSAT to provide parallel data sets for developing adequate simulation procedures and to provide data for understanding the relationship between the observed responses of the P78-2 engineering experiments (SC1-8B, TPM) and the discharges producing them.

7. Both the experimental data and model calculations indicate that the H_0 pulse shapes follow the exciting pulse. Therefore, in the ideal case, it should be possible to obtain reasonably good simulation of the EID H_0 responses, at least away from the exciting wire. This conclusion must be verified by model calculations with realistic CDI source terms and by testing. In addition, the EID response to asymmetric excitations should be obtained for the SCATSAT.
8. There may be practical limitations in adapting the CDI technique as it is presently embodied in real hardware to provide the high-level (100 to 500 A), wide pulses (1 to 5 μ s) characteristic of the blowoff discharge of large satellite dielectric structures. A coupling analysis performed during Phase I of the present program indicates that a critical parameter controlling pulse width is the plate to test object capacitance. During the SCATSAT electrical tests, to increase the pulse width of the CDI excitation from 10 ns to 30 ns, the plate spacing was decreased from 30 cm to 6 cm. This had the consequence of significantly altering the H_0 amplitude distribution in a manner which makes the response less like that created by EID. Moreover, the relatively weak coupling between pulser and CAN will require relatively large voltage sources (tens of kV) to produce the necessary currents. This would require a rather large and cumbersome isolated voltage source. The question of practically implementing one or more current injection techniques is being addressed in the second task of this study.

6. DEVELOPMENT OF AN ELECTRICAL TEST PROCEDURE

6.1 IMPLICATIONS OF THE CAN TESTS FOR THE PRESENT MIL-STD 1541 TEST PROCEDURE

The present version of an arc discharge test is described in Reference 52 in MIL-STD 1541 (Section 6.5.4.2.1). Figure 71 shows the arc discharge pulser. Typically, the pulser is triggered not by an isolated source like the Anvil 160, but by a normal pulse generator connected to external ground. Basically, the exciting source is the arc discharge produced between a carbon electrode and the vehicle (or between two arcs 30 cm from the vehicle) when a high-voltage pulse is impressed across the spark gap. The breakdown voltage, peak current I_p and pulse FWHM ($W_{1/2}$) are functions of the charging capacitor, pulse transformer, electrode configuration, gap width and atmospheric conditions such as humidity and altitude. However, I_p values of 10 A, $W_{1/2} = 10$ ns are typical. The estimated peak current amplitude of the arc source used by Martin in testing the P78-2 at Denver (about 5000 feet above sea level) was 40 ± 10 amps. The arc current pulse employed by IRT in testing the SCATSAT (Ref 2) averaged 17.6 amps. A typical arc pulse is shown in Figure 72. This figure should be compared to the return current pulse shapes shown in Section 4.

The results of the electrical testing reported in Reference 2 and the EID testing reported in Reference 37 and in this report clearly confirm that the present MIL-STD 1541 inadequately simulates the response of satellite-like objects to blowoff discharges in all aspects if this response is measured by the width, amplitude, and relative distribution of the body replacement currents. The data presented in Reference 2 indicate that the internal wire responses are also too small, except possibly for cases where an arc occurs in close proximity to a wire to which discharge energy can be closely coupled.

These findings are clearly evident in the data presented in Tables 10 and 11 of this report. The normalized H_θ and \dot{H}_θ arc discharge responses of the CAN (per amp of drive current, or for the same I_p/τ_p ratio) are two orders of magnitude lower than those induced by EID or CDI excitation of meter-sized surfaces. The pulse widths attainable

ORIGINAL PAGE IS
OF POOR QUALITY

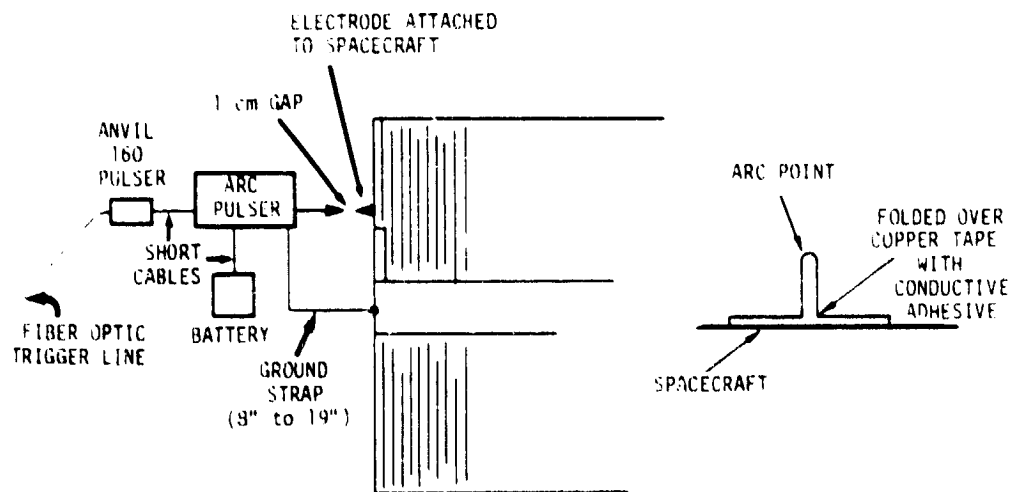
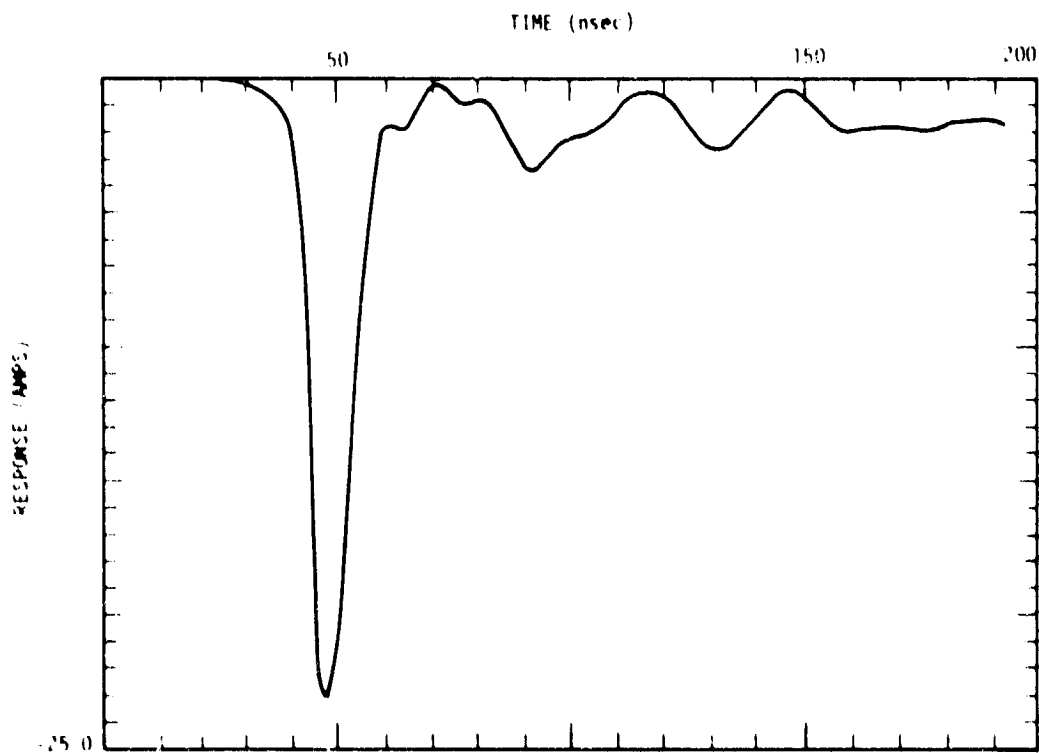


Figure 71. ML-STD 1541 arc injection



RT 17496

Figure 72. Arc current

with the specified MIL-STD 1541 arc are similarly much narrower, although one could conceivably design discharge sources which have a high amplitude and wider pulse. For example, the arc discharge simulation used to excite the CAN had a peak amplitude of 1000 amps and a $W_{1/2}$ of 40 ns. However, as the data of Table 5 indicates, the observed H_ϕ currents at the side of the CAN were typically 0.15 to 0.35 A/m, one to two orders of magnitude smaller than those produced by either EID or CDI for peak drive currents one-tenth as large. Moreover, the observed falloff of the amplitude H_ϕ with distance from the discharge produced by the arc discharge does not well simulate the observed EID skin current patterns. To the degree that the laboratory EID data mirrors the responses of spacecraft in the space environment, the present MIL-STD 1541 arc discharge is a gross undertest. Whether, and to what degree the ground test data is representative of what is occurring in space is a question which has not been resolved. This issue is addressed in Section 6.2.

The reason that the present arc discharge is an inadequate simulation of the observed EID response is that it simulates only one aspect of the discharge, punch-through or flashover. Current models of discharge (Refs 44,46-49,53) assume that the blowoff of electrons is a consequence of a complex process which is initiated by punchthrough or flashover of charge. It is clear from the experimental results and modeling reported here and in Reference 37 that the predominant driver for the replacement currents is the blowoff of electrons which travel distances comparable to a spacecraft dimension before returning to the object or may in some cases escape completely.

One can readily estimate the relative responses produced by blowoff and punchthrough discharges. A detailed treatment is found in Reference 46. For a punchthrough discharge current, I_D , the replacement current, I_r , which flows from external conductors to the substrate is

$$I_r = \left(\frac{C_s}{C_\infty + C_s} \right) I_D \quad , \quad (6)$$

where C_s is the capacitance of the charge layer to the conducting substrate, and C_∞ the capacitance of the charge layer to surrounding conductors. For the conditions which applied in the CAN tests $C_s \approx 5$ nF, while C_∞ is estimated to be ≤ 10 pF. Thus the ratio of $I_r/I_D \leq 0.002$. Similar conditions hold in space. Based on this argument, the anticipated replacement currents are only a few tens of a percent of the punchthrough

current. In fact, the observed values of $I_\phi = (\pi) \cdot (1.36) \cdot H_\phi$ are about 2 amps or less for a 1000 amp discharge, in agreement with this simple calculation.

On the other hand, if \bar{I}_B is a weighted value of the emitted blowoff current, then the return current is given by

$$I_r = \left(\frac{C_s}{C_\infty + C_s} \right) I_B \quad (7)$$

Since $C_\infty / C_s \ll 1$, the return currents are nearly equal to the weighted blowoff current. When the CAN was grounded to the TANK, or when the emission current was sufficiently low so that space-charge limiting did not occur, I_B , the net charge blown off, was nearly equal to \bar{I}_B and also to I_r . For space-charge-limited emission, which applies for an isolated test object, \bar{I}_B will be some fraction of I_B , of the order of 0.1 to 0.3 for the experimental conditions relevant to the CAN test.

The replacement currents created by CDI, when properly scaled, better simulate the observed EID responses because it mimics the principal discharge stimulus, the blowoff discharge, rather than punchthrough or flashover.

6.2 ENVIRONMENT EFFECTS

In developing a qualification test, one would like to provide a reasonable worst-case simulation of the effects of EID. It is therefore necessary to compare the results of the ground test data to the P78-2 data and to other ground test studies in which the environmental parameters were varied in terms of components included and exposure fluxes. One may then determine whether there are important effects not included in typical general test simulation which influence the on-orbit charging and discharge behavior of a spacecraft. Unfortunately, there is little external discharge response data from the P78-2 which could be directly compared to the EID coupling data reported here because the magnitude of the exciting source is unknown. Therefore, we have focused on the relevant ground test data.

Nearly all of the ground test data taken to date has been based on an extremely simple environment simulation, monoenergetic electrons with energies of ca. 1 to 30 keV, and fluxes of 1 to 10 na/cm². It is the electron component of the heated substorm plasma which plays the most important role in the surface charging of spacecraft dielectrics. However, as the discussion in Section 2 indicates, the actual

space radiation environment is much more complex, containing the proton and other ion components of the space plasma, higher energy electrons associated with the trapped electron belts, and solar electromagnetic radiation. For reference, Table 12 summarizes typical environment values. It is to be noted that the provisional specified environment (Ref 54) defines the worst-case substorm as a plasma environment containing electrons and protons with particle temperatures for electrons ($k_B T_e$) up to 10 keV at a density $N_e = N_p$ of 2 cm^{-3} . The proton temperature is assumed to be twice that for electrons. The corresponding electron flux Φ_e for a Maxwell-Boltzmann distribution is

$$\Phi_e = \frac{1}{4} n \bar{v} \quad (8)$$

where \bar{v} for a single Maxwellian is

$$\bar{v} = \sqrt{\frac{8 k T}{\pi m_e}} \quad (9)$$

For $N_e = 2 \text{ cm}^{-3}$ and $k_B T_e = 10 \text{ keV}$, $I_e = 3.3 \times 10^9 \text{ e/cm}^2 \text{ sec}$ or 0.54 na/cm^2 . The corresponding proton fluxes and currents are $1.1 \times 10^8/\text{cm}^2 \text{ sec}$ and 18 pa/cm^2 . Note that this represents a more severe environment than that given in Tables 1 and 12. Most experiments have been conducted with electron fluxes of 1 to 10 na/cm^2 and above. Thus, typical ground-test-to-space-electron-flux ratios are 10 to 100 or more. Typically, naturally trapped high-energy electron fluxes are only a few pa/cm^2 or less.

The potential reached by a dielectric sample is determined by the combined charging effects of each of the radiation components shown in Table 12. The primary effort of the substorm electrons is to produce charge buildup. Neglecting leakage to conducting boundaries, one would expect that the potential attained as a consequence of irradiation with monoenergetic electrons to be the so-called second crossover potential; i.e., that at which the difference between the incident beam energy and the sample potential is such that secondary electron emission from the dielectric is unity. Of course, breakdown may occur first. For polymers, this potential difference is typically a few hundred volts to a kV (Ref 55). The data presented in Table 4 indicates that the potentials reached before discharge occurs are all well below the second crossover potential for $E_i = 20 \text{ keV}$. For Kapton and Teflon exposed to 10 keV electrons

Table 12. Components of Space Radiation Environment

Component	Characteristics	Effects Produced	Comments
1. Net particle density	ca. $0.5-10 \text{ cm}^{-3}$ at geosynchronous altitudes		
2. Solar electromagnetic	0.14 w/cm^2 total flux. Visible, IR like 6000°K blackbody. UV comprised of discrete lines, of which $\text{H(Ly}\alpha\text{)}$ is most important, superimposed on a continuum.	photoemission (UV,x-ray), heating (visible, IR) Photoconductivity (UV, visible)	Photoemission controlled by surface properties
3. Natural trapped electron	Outer zone specified in AEI-7. Energies ca. $0.1-5 \text{ MeV}$. Integral omnidirectional flux ca. $10^8 \text{ e/cm}^2/\text{s}$ at geosynchronous altitudes	Charge and dose deposition, secondary emission, backscatter, semiconductor damage, leakage currents, discharges	Primary effects in spacecraft dielectrics include enhancement of bulk charge leakage, charging of internal dielectrics
4. Magnetic substorm	Correlation with A_p index. Characterized by single or double Maxwellian $J_e < 1 \text{ na/cm}^2, k_B T_e < 15 \text{ keV}$ $J_i < 100 \text{ pa/cm}^2, k_B T_i < 20 \text{ keV}$ where T_e is T_{rms} , based on ATS-6 data.	Charge, dose deposition secondary emission, backscatter, leakage currents, discharges	Typical electron environments $J_e = 0.02-0.12 \text{ na/cm}^2, k_B T_e = 1 \text{ keV}$ $= 0.01-0.2 \quad = 5 \text{ eV}$ $= 0.01-0.07 \quad = 8 \text{ keV}$ Typical ion environments $J_i = 2-7 \text{ pa/cm}^2, k_B T_i = 3 \text{ keV}$ $J_i = 2-8 \text{ pa/cm}^2, k_B T_i = 7 \text{ keV}$ Based on ATS-5 data the observed ATS-6 environments are more severe
5. Nuclear trapped electron	Fission electron spectrum. Integral fluxes ca. $10^9 \text{ e/cm}^2 \cdot \text{s}$ (minutes), ca. $7 \times 10^7 \text{ e/cm}^2 \cdot \text{s}$ (long term)	Charge and dose deposition, secondary emission, backscatter, semiconductor damage, leakage currents, discharges	Same as item 3, but charging rates are faster because of higher fluxes

any discharges which occur are small, and the observed potentials reached are also less than the second crossover voltage. This is due to the leakage of injected charge to edges.

Several of the components of the environment not typically included in the ground testing tend to relax charge buildup. The effect of solar UV is to generate photoelectrons. The intensity of such photoelectron generation is such that only rarely can the hot plasma charge the spacecraft structure to more than a few tens of volts in sunlight. The positive ion component of the plasma also tends to reduce the vehicle potential through the generation of secondary electrons. The high-energy electrons can produce two effects. In thin dielectrics (compared to a typical electron range) the

induced radiation conductivity enhances bulk leakage, lowers the potential buildup and minimizes or eliminates discharges caused by the keV electrons. In thick dielectrics such as inside cables or printed circuit boards, the higher energy components can embed themselves in the dielectric and cause discharges. This phenomenon has been called ECEMP or Electron Caused Electromagnetic Pulse effects. The SCATHA program has largely ignored ECEMP, although work in this area has been supported by the Air Force Weapons Laboratory. A limited amount of evidence indicates that charging processes are rate dependent at fluences which span the range of those relevant for the space environment. We briefly review some of these effects and assess their impact on the development of realistic test procedures.

The available experimental evidence clearly indicates that the presence of a significant flux of high-energy electrons with ranges great enough to penetrate thin dielectrics will reduce or eliminate the discharges produced by low-energy electrons (10 to 20 keV). The mechanism for this process is the radiation-induced conductivity. Normally dielectric breakdown occurs in these materials because the low-energy, nonpenetrating injected electrons are trapped and retained so that the fields created reach the electric breakdown strengths in these materials which are typically 10^6 to 10^7 V/cm. Typical dark conductivities (σ_0) in these materials are 10^{-20} to 10^{-16} (Ωcm) $^{-1}$ (Ref 56). The relaxation time t_r for charge buildup in this case is

$$t_r \approx \frac{\epsilon}{\sigma_0} < (3.8 \times 8.5 \times 10^{-14}) / 10^{-16} = 2.6 \times 10^7 \text{ seconds} \quad (10)$$

or about ten months.

The time to reach dielectric breakdown can be estimated from the relationship

$$q_B \approx \epsilon / E_B \quad (11)$$

where q_B is the surface charge density, ϵ is the dielectric constant and E_B the dielectric breakdown strength assuming no charge leakage out of the sample or from secondary electron emission. Table 13 shows the estimated breakdown times for $J_e = 1 \text{ na/cm}^2$ incident electron flux for various materials. Breakdown will occur if the breakdown time $t_B = q_B / J_e$ is less than t_r . It can be seen from the table that breakdown occurs in times of the order of one to a few minutes. In fact, the surface potential scans shown in Section 4 indicate that discharges occur at about this rate.

Table 13. Estimated Discharge Voltages and Discharge Times

Material	ϵ/ϵ_0	Thickness (10 ⁻³ cm)	Dielectric Strength (10 ⁶ V/cm)	Breakdown		Observed Peak Breakdown Voltage for $E_j=20$ keV (kV)	Minimum Time to Discharge (seconds) ($J_e=1$ nA/cm ²)
				Estimated Surface Charge Breakdown (10 ⁻⁷ C/cm ²)	Observed Surface Charge for $E_j=20$ keV (10 ⁻⁷ C/cm ²)		
1. Silvered FEP Teflon	2.1	13	1.6	2.9	1.9	16	290
2. MgF ₂ covered fused silica coverslips	3.8	15	0.25	0.84	3.6	12	84
3. Nonconductive white paint	TBD	5-10			Leakage prevents breakdown		
4. Nonconductive black paint	TBD	5-10			Leakage prevents breakdown		
5. Kapton tape	3.4	2.5	2.8	8.4	7.9	15	840
6. Conducting solar cell coverslips		15			Leakage prevents breakdown		
7. Fiberglass substrate	4.5	15	0.25	1.0	3.8		100

This time is much shorter than the predicted relaxation times given by ϵ/σ_0 . If the intrinsic dark conductivity is sufficiently high, as it is in dielectric pigment thermal control paints, then the injected charge can relax at a sufficiently high rate to prevent dielectric breakdown.

The surface charge densities at breakdown given in Table 13 for Kapton and Teflon were reasonably close to those predicted, while that for the coverslips was about three times higher than predicted. This is probably because a low value for the dielectric strength was used in the calculation.

Charge buildup in real dielectric structures is mitigated by leakage to dielectric edges and to the rear conducting substrate. This leakage is enhanced by the radiation-induced conductivity created in the bulk of surface dielectric both by the substorm electron population which is embedded in the material and by that component of the trapped radiation population which penetrates thin surface dielectrics. Radiation conductivity σ_R is typically given by an expression of the type

$$\sigma_R = K_R \dot{D}^\Delta \quad (12)$$

where \dot{D} is the material dose rate, proportional to the incident flux, Δ an exponent which is less than, but close to 1, and K_R is a material constant. Table 14 gives values for the dark conductivity, K_R and Δ for common spacecraft taken from Reference 56.

For a 1 na/cm^2 flux of 20 keV electrons the deposited dose rate is about $2.5 \times 10^3 \text{ rads/s}$ in these materials. The corresponding radiation-enhanced conductivities are shown in Table 14. It can be seen that the radiation conductivities completely dominate the dark conductivities.

Because $\sigma_R \gg \sigma_0$ charge, relaxation times are considerably shortened near the front surface of the material in which the nonpenetrating charge is stopped. The occurrence of breakdown depends on whether charging equilibrium is reached at an electric field less than E_B . At charging equilibrium, the net injected flux ϕ_0 is balanced by an ohmic leakage current which flows primarily out of the front surface of the dielectric to conducting edges such that

$$J_{\text{in}} = e\phi_0 = J_{\text{out}} = \sigma_R E_0 = K_R \dot{D}^\Delta E_0, \quad (13)$$

where E_0 is the average equilibrium internal field.

Table 14. Conductivity of Representative Spacecraft Insulators

Material	Dark Conductivity	K_R		σ_R	ϵ/σ_R
	$10^{-18} (\Omega \text{ cm})^{-1}$	$(\text{ohm cm})^{-1}$		$[(2.5 \times 10^3 \text{ rads(mat)/s}) (\text{sec})]$	
Teflon	0.4	3.5×10^{-17}	0.7	8.4×10^{-15}	22
Kapton	5.6	3.2×10^{-17}	0.9	3.6×10^{-14}	8.3
Mylar	6.3	7.2×10^{-18}	0.8	3.8×10^{-15}	76
Fused Silica	1	2.5×10^{-16}	1	6.3×10^{-13}	0.5

The average dose rate is proportional to the incident flux so that

$$E_o \propto \frac{e\Phi^{(1-\Delta)}}{K_R} \quad (14)$$

According to this simple argument the equilibrium field reached should depend only weakly on flux. Whether breakdown occurs at all depends on the values of K_R and E_B for the given material. This is a desirable situation as it would make test results relatively insensitive to incident electron flux. The data reviewed below indicates that this is approximately so, for irradiation with monoenergetic, nonpenetrating electrons of simple planar samples with grounded edges. Unfortunately, the available data also indicates that the observed discharge behavior is sensitive to the flux and energy spectrum of the incident electrons for more complicated, and hence more realistic, simulations.

Although the dose rates of the penetrating electron component are relatively small (typically ca. 1 rad/s) for thin dielectrics exposed to the geosynchronous environment, such radiation can have a significant effect on the observed discharge behavior.

We have reproduced in Table 15 data taken from References 34 and 57 describing the discharge characteristics of a 200 cm^2 array of 8.5 mil thick quartz second-surface mirrors mounted on an aluminum plate. The substrate return current was monitored, as was the equilibrium surface potential for this sample which was connected to ground by a 1Ω resistor. The 25 keV electron component was chosen to simulate those electrons which stop in the sample and the 350 keV component represented those penetrating. The 200 keV electrons do not penetrate the 8.5 mil thick sample.

From the table it is evident that addition of the penetrating electron component alters the charging and discharge behavior of those samples. As the ratio of the penetrating to nonpenetrating component is raised to about 1:70, the discharges

Table 15. Second Surface Mirror Discharge Characteristics for
Simultaneous Low and High Energy Electron Exposures^a

Beam Energies (keV)	Currents (na/cm ²)	Discharge Frequencies (min ⁻¹)	Substrate Peak Current (A)	Substrate Return Charge (μC)	Pulse Width (μs)	Comments
25	0.19	0.08	28	16	0.57	
25	0.77	0.5		11		
25	1-5	0.5-2.5	35	28-24	0.68-0.8	
25	0.77	0		0		No discharges
350	0.17					
25	5.8	0.1-0.5		-		Small charge release
350	0.17					
25	13.1	0.5-1		0.99		
350	0.17					
25	0.29			0.2		
350	0.003					
25	13.1	10		12		Same appearance as low energy discharges
200	0.1					
25	0.77	0.5		10		Same appearance as low energy discharges
200	0.1					

^aFrom References 34 and 57.

diminish and cease. With the high-energy electrons present the discharge magnitudes were considerably reduced for all ratios examined below the threshold. For higher ratios, the radiation-induced conductivity is sufficient to keep charge leakage high enough so that the sample potential does not build up to the point where breakdown occurs. Note that the presence of the nonpenetrating 200 keV beam does not stop or significantly diminish the discharge frequency, supporting the proposed mechanism. The authors of Reference 57 point out that the ratio of low-energy to high-energy current for SCATHA is about 200, so that the presence of the penetrating high-energy electrons is not expected to inhibit discharging in the solar array coverslips. However, as the P78-2 coverslips are somewhat thinner than those studied (6 mil versus 8.5 mil), the ratio is apt to be somewhat lower so that this conclusion may not be valid.

Other materials such as Kapton and fiberglass also show diminished rates and amplitudes of discharge when a penetrating electron component is added to the simulation. In the case of Kapton, all discharging ceased.

These results have implication for the magnitude and response of the signals coupled into spacecraft structure. Namely, if the magnitude of the charge blown off from a thin-surface dielectric diminishes because of the presence of the high-energy penetrating electron component, the induced replacement currents will also diminish.

The authors of Reference 37 report that when their cylindrical test object covered at one end with 8.5 cm thick fused silica, second-surface mirrors, was exposed to a combined environment comprised of 6.4 na/cm^2 of 25 keV electrons and 0.5 na/cm^2 of 350 keV electrons, the magnitude of the discharge current, as measured by the return current signal in the grounded configuration, decreased from 100 to 180 A to 35 A. The amount of charge blown off also decreased from 170 to 180 μC to 40 to 60 μC . The peak currents observed near the top of the CAN were about a factor of two lower than those observed for low-energy electrons alone. The magnitude of these skin currents were difficult to resolve by hand integration of the \dot{B} data because of the strength of the high-frequency components which were much more prominent in this case.

Other evidence has been adduced from ground testing that the charging behavior of materials such as quartz fabric changes significantly as the incident flux goes from those typical of laboratory experiments to space electron fluxes (Ref 58).

The charging behavior of Kapton is even more complex. Laboratory studies have indicated that the bulk resistivity of Kapton decreases by several orders of magnitude on exposure of the sample to the visible and near UV components of the solar spectrum. This effect is long lasting, and will persist in vacuum even after the illumination is removed. Such a large increase in bulk conductivity can keep this material from discharging (Ref 59).

Balmain (Ref 60) has examined rate effects on the discharge behavior of small-area (1.7 cm^2) samples of Kapton H, Mylar and FEP Teflon exposed to 20 keV electrons at fluxes of 0.5 to 100 na/cm^2 . He found that the discharge characteristics measured by the peak edge and substrate currents and charge and pulse widths were essentially unchanged for Teflon FEP and Mylar. The peak replacement currents and charge increased by about a factor of four for Kapton over the range of incident electron current densities employed. A similar, but less rapid, increase in I_p and Q_p with incident flux is evident in OSR data presented in Reference 34.

From this brief discussion, it is clear that several of the components of the natural environment, namely solar radiation and high-energy electrons capable of penetrating thin dielectrics, can significantly alter the charging and discharge characteristics of spacecraft surface dielectrics, often in the sense of preventing or minimizing EID. This may be an explanation of why EID effects in space systems do not appear to be as severe as one might predict from monoenergetic high flux tests. This can best be investigated by trying to infer from the P78-2 environment, surface potential and transient response data the magnitude of the exciting discharge. Such an

exercise requires completion of the P78-2 coupling model. However, there exists no adequate physical models which tie together the effects of charge deposition, energy deposition, bulk material properties such as radiation and optical photoconductivity so that believable extrapolations from the ground test data to space conditions can be made. The models presented in References 56 and 61 are a step in that direction.

6.3 SCALING

The objective of the CAN test was to develop a data base on the external response of a simple, highly symmetric object excited by EID in well-defined axisymmetric dielectrics. There were no external penetrations such as booms, antennae, or solar array panels which would modify the anticipated highly symmetric and easy to analyze response of this object, and to facilitate comparison with existing electrical test data for the same object. Data was taken for a limited range of energies (10 to 20 keV) and electron fluxes (1 to 5 na/cm²).

A simple model was developed by IRT during Phase I which attributes the EID response of the CAN to a uniform emission of electrons blown off the dielectric surface during discharge. This model was later elaborated by Wenaas and Woods (Ref 44) on the basis of a much larger body of experimental evidence available to them. The controversial features of the model described in Section 5.2 are the assumptions about electron emission; i.e., uniformity, essentially zero electron emission energy and dielectric albedo of unity. The noncontroversial parts of the model are its emphasis on the emitted blowoff charge as the primary driver for the replacement currents generated and the use of an SGEMP code to track this particle motion in the electromagnetic fields due to the charges embedded in the dielectric, induced charges on adjacent conductors and the self-fields of the emitted charge itself.

The model gives reasonably good agreement with the H_{θ} measurements on the simple symmetric cylinders studied by both IRT and JAYCOR. However, in the latter series of tests more complicated geometries were investigated. One was a mesh antenna situated on the end of a conducting boom. Here, the observed currents were a factor of ten higher than predicted. In order to reconcile the observed large antenna mast currents with prediction, various ad hoc modifications to the emission model were tried by the authors of Reference 37. These modifications include increasing the energy of the emitted electrons, varying the pattern of emission and including a neutral plasma to shield the emitted electrons from the space charge field. Only when the emitted electrons were given initial energies of ca. 4 to 5 keV in the presence of the

plasma could the calculations be made to agree with experiment. On the other hand, the JAYCOR group was able to predict the correct magnitude of currents flowing on a mock solar array boom excited by discharge on a solar panel situated at the end of the boom. Thus, key elements of the physics of the discharge process are evidently missing from the emission model.

Until these results for reentrant geometries were uncovered, the lack of such a model was not felt to be a significant handicap for practical calculations. The JAYCOR calculations were based in part on emission waveforms and amplitudes derived from laboratory measurements on the discharge behavior of the materials of interest mounted on grounded conducting substrates. Implicit in this is the assumption, utilized by the authors of Reference 37 and IRT in analyzing the behavior of the CAN, that the emission of charge in the grounded configuration is mimicked by the replacement current flowing through the ground strap.

On the basis of small sample studies it was found that experimental scaling laws could be derived from common dielectrics. Their relationships were first noted by Balmain (Ref 33) for areas up to 100 cm^2 and extended to larger area samples (ca. 1 m^2) by others. The experimental data implied that the peak discharge current scales approximately like the square root of the sample area, the discharge pulse width similarly and the total charge like the sample area. A plot of the discharge currents observed in Kapton as a function of sample area is shown in Figure 73. This figure is originally due to Inouye (Ref 49). In the figure we have shown both Inouye's best fit to the data as well as Balmain's best fit for his small area samples. Note that there is significant fluctuation about the "best fit" which can be over an order of magnitude. One can derive similar scaling laws for other substrates. A plot for fused quartz is shown in Figure 74.

The fact that such scaling laws exist have led to the creation of various emission models to explain them. The model described in Section 5.2 is one of these. Other models have been proposed which depend on the observed large edge potential gradients (which are evident on the surface potential scans presented in Section 4) to enhance emission and overcome the effects of space-charge limiting of the emission currents necessary to account for the magnitude of the observed discharge currents (Refs 47-49). A key feature of these models is that the strong lateral electric fields present near the edge permit the acceleration of electrons so that they can travel relatively large distances before being collected. The model described in Reference 44 avoids the problem of space-charge limiting by assuming a dielectric surface albedo of

ORIGINAL PAGE IS
OF POOR QUALITY

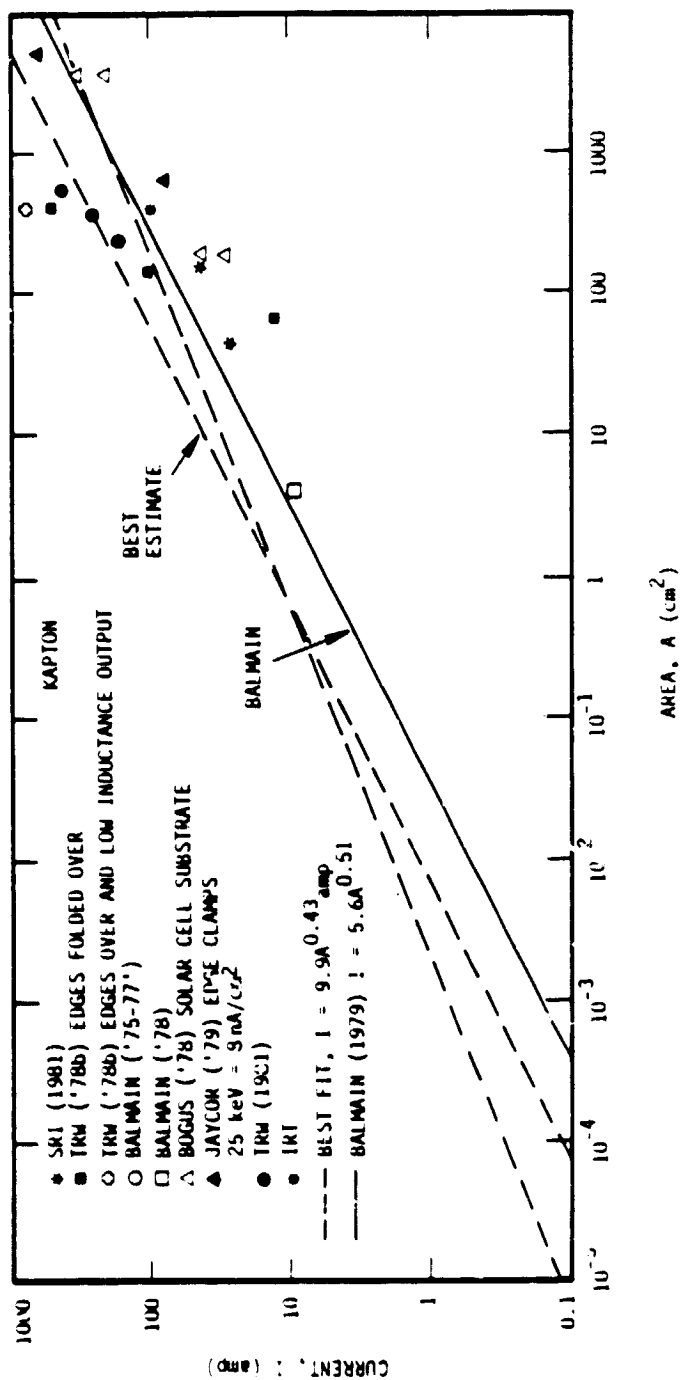


Figure 73. Discharge peak current versus area for Kapton (after Inouye, Ref 49)

ORIGINAL PAGE IS
OF POOR QUALITY

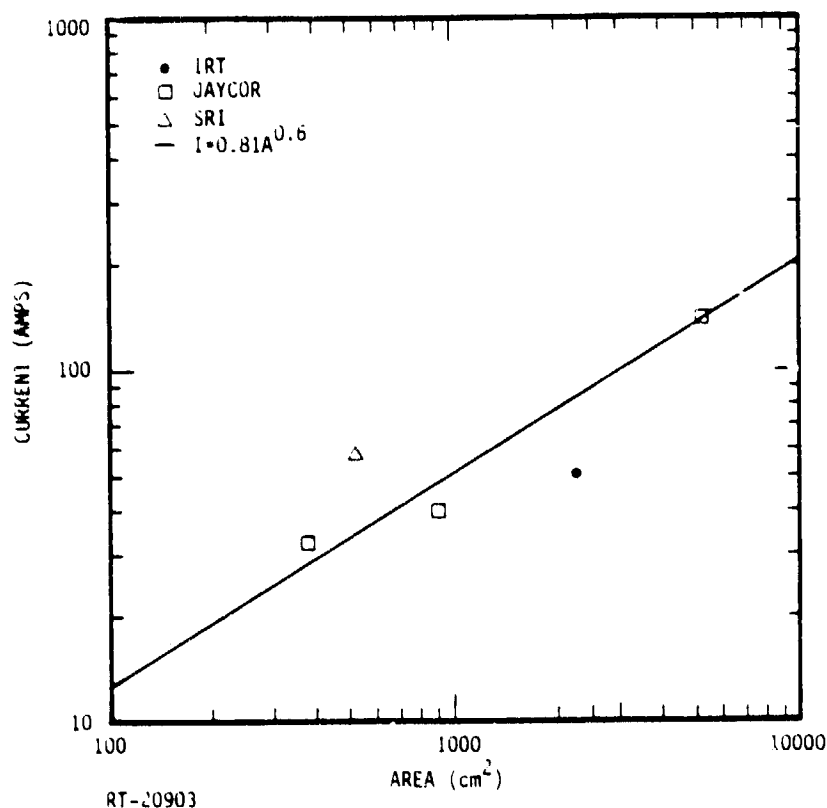


Figure 74. Peak discharge current versus area for fused quartz

one so that electronics which fall back on the dielectric surface because of space-charge limiting can be reaccelerated and ultimately escape.

While the models are capable of predicting in a general way emission which satisfies the scaling laws, it is not clear that they are more successful in predicting the response of complicated objects to a blowoff discharge without further additions to the physics of the basic discharge process embodied in the discharge models in terms of the nature of, energy and spatial distributions of the emitted particles.

Not taken into account in a consistent manner in any of these models is the observation by Hazelton et al. (Ref 62) that there are several components in the blowoff of charge consequent to an EID. For Teflon samples irradiated with electrons of 16 to 26 keV two distinct fluxes of particles were observed. The first (0 to 600 ns) consists of high-energy (ca. 7 keV) electrons. The second arrives later (ca. 1 to 5 μ s) and consists of low-energy electrons (~ 1 eV) and ions (70 eV) leaving the discharge site as a quasi-plasma. The origin of plasma may be due to ejection during the discharge of

material vaporized during the formation of discharge channels which contain the plane of high specific ionization in which most of the nonpenetrating charge and dose is deposited. These discharge channels are shown in photographs reproduced in Reference 33. The formation of gaseous ionized, conducting discharge channels is an essential feature of one theory of dielectric breakdown of solids (Ref 63). These channels are analogous to the familiar Lichtenberg figures produced as a consequence of the irradiation of thicker dielectrics such as poly (methyl methacrylate) by nonpenetrating electrons.

Some evidence for the emission of this plasma may have been seen during our experiments. Crude time-of-flight measurements, reported in Section 4.4.3, were made in which the arrival of the peak of the blowoff currents was timed against the peak of the return current pulse with the CAN grounded. In many measurements the time difference was of the order of 300 ns. Given the distance from the CAN to blowoff collector, this would correspond to electrons with an energy of about 71 eV. This is close to the energy of emitted ions (70 eV) collected after blowoff discharges in Teflon (Ref 62).

The blowoff currents seen consequent to the discharge of the Teflon sample in the high-impedance configuration were clearly positive (q.v. Figure 51). One explanation for this observation is that space-charge limiting will cause the return to the CAN of emitted electrons while the positive ion component of the plasma is repelled by those forces and can reach the blowoff collector. It would clearly be useful to perform further experiments of the type described in Reference 62 for samples isolated from ground during the discharge to see whether these findings can be duplicated or are an artifact of the observed breakdown of our isolation resistor during the discharge.

There is another point to be made about the scaling laws. They are reasonably accurate in describing the discharge behavior of uniform, smooth circular samples, usually with grounded edge clamps for a limited range of irradiation energies (20 to 25 keV) and beam currents. Whenever one includes data from a wider range of sample thickness, shapes and edge configurations, the scatter in the data increases significantly. As we have pointed out, the presence of lapped or butted seams, or of materials with high-perimeter-to-surface ratios, can significantly alter the amount of charge involved in a discharge if compared to that for smooth samples. The IRT data point shown in Figure 73 is placed at an area corresponding to the overlap of the two layers of tape as the surface potential scans indicate that this is where discharges occurred. Moreover discharge behavior can be affected by the presence of edge clamps. The

authors of Reference 35 reported that discharges could not be induced in a 2 mil Kapton sheet irradiated with 25 keV electrons and currents of up to 13 na/cm^2 unless the edges were grounded.

In addition, the nature of the discharges induced in these materials can change markedly if other components of the space radiation environment, such as penetrating high-energy electrons or UV, are added to the simulation. As the effect of these additional components is typically to relieve charge buildup in these thin dielectrics, the scaling laws should probably be taken as a worst-case guide to the discharge behavior of these materials.

Without better physical insight into the nature of the discharge process it will be difficult to predict with confidence the response of realistic spacecraft structures containing booms, antennae, solar panels, etc., to EID. This in turn makes it difficult to derive general electrical simulation procedures without performing additional electron spraying tests on a variety of satellite-like geometries and dielectric structures. However, it is clear that the CDI simulation of blowoff is a better approximation to the EID coupling process than the present MIL-STD 1541 arc.

REFERENCES

1. R. C. Keyser, R. E. Leadon, A. Weiman and J. M. Wilkenfeld, "Electron-Induced Discharge Modeling, Testing and Analysis for SCATHA, Volume I - Phenomenology Study and Model Testing," DNA Contract 001-77-C-0180, DNA Report 4820F-1, IRT Report 8161-015, 31 December 1978.
2. R. Keyser and J. M. Wilkenfeld, "Electron-Induced Discharge Modeling, Testing and Analysis for SCATHA, Volume II - Internal Coupling for Two EID Simulation Techniques," DNA Contract 001-77-C-0180, DNA Report 4820F-2, IRT Report 8161-018, 31 December 1978.
3. S. E. DeForest and C. E. McIlwain, "Plasma Clouds in the Magnetosphere," *J. Geophys. Res.* 76, 3587 (1971).
4. R. L. McPherron, "Magnetospheric Substorms," *Rev. Geophys. Space Phys.* 17, 657 (1979).
5. C. Rostaker, S.-I. Akasofu, J. Foster, R. A. Greenwald, Y. Kamide, K. Kawasaki, A. T. Y. Lui, R. L. McPherron and C. T. Russell, "Magnetospheric Substorms--Definitions and Signatures," *J. Geophys. Res.* 85, 1663 (1980).
6. S. E. DeForest and R. J. R. Judge, "Plasma Clouds and Auroral Arcs," *ESRO Spec. Pub.* 107, 103 (1975).
7. R. H. Eather, S. B. Mende and R. J. R. Judge, "Plasma Injection at Synchronous Orbit and Spatial and Temporal Auroral Morphology," *J. Geophys. Res.* 81, 2805 (1976).
8. H. B. Garrett, "The Current Status of Predictions of Low-Energy Plasma Interactions with Space Systems," AFGL-TR-79-0089, 4 April 1979.
9. H. B. Garrett, "Review of Qualitative Models of the 0 to 100 Near-Earth Plasma," *Rev. Geophys. Space Phys.* 17, 397 (1979).
10. R. J. R. Judge, "Electron Excitation and Auroral Emission Parameters," *Planet. Space Sci.* 20, 2081 (1972).
11. H. B. Garrett and S. E. DeForest, "An Analytical Simulation of the Geosynchronous Plasma Environment," *Planet. Space Sci.* 27, 1101 (1979).
12. S. E. DeForest, "Spacecraft Charging at Synchronous Orbit," *J. Geophys. Res.* 77, 651 (1972).
13. E. C. Whipple, "The Equilibrium Electric Potential of a Body in the Upper Atmosphere," NASA X-615-65-296 (1965).
14. U. Samir and A. P. Willmore, "The Equilibrium Potential of a Spacecraft in the Ionosphere," *Planet. Space Sci.* 14, 1131 (1966).

15. C. L. Brundin, "Effects of Charged Particles on the Motion on Earth Satellite," AIAA.
16. E. C. Whipple and L. W. Parker, "Theory of an Electron Trap on a Charged Spacecraft," J. Geophys. Res. 74, 2962 (1969).
17. E. C. Whipple and L. W. Parker, "Effects of Secondary Electron Emission on Electron Trap Measurements in the Magnetosphere and Solar Wind," J. Geophys. Res. 74, 5763 (1969).
18. D. A. McPherson and W. R. Schober, "Spacecraft Charging at High Altitudes: The SCATHA Satellite Program," AIAA Progress in Astronautics and Aeronautics 47, 15 (1976).
19. R. R. Shaw, J. E. Nanewicz, and R. C. Adamo, "Observations of Electrical Discharges Caused by Differential Satellite Charging," *ibid.* 47, 61 (1976).
20. M. A. Grajek and D. A. McPherson, "Geosynchronous Satellite Operating Anomalies Caused by Interaction with the Local Spacecraft Environment," Spacecraft Charging Technology Conference 1978, AFGL-TR-79-0082, p. 769 (1979).
21. J. J. Mandell, I. Katz, G. W. Schnuelle and J. C. Roche, "Photoelectron Charge Density and Transport Near Differentially Charged Spacecraft," IEEE Trans. Nucl. Sci. NS-26, 5107 (1979).
22. N. J. Stevens and R. C. Roche, "NASCAP Modeling of Environmental Charging Induced Discharges in Satellites," *ibid.* NS-26, 5112 (1979).
23. B. Feuerbach and B. Fitton, "Experimental Investigation of Photoemission from Satellite Surface Materials," J. Appl. Phys. 43, 1563 (1972).
24. E. H. Darlington and V. E. Cosslett, "Backscattering of 0.5-10 keV Electrons from Solid Targets," J. Phys. D. 5, 1969 (1972).
25. M. S. Chung and T. E. Everhart, "Simple Calculation of Energy Distribution of Low-Energy Secondary Electrons Emitted from Metals Under Electron Bombardment," J. Appl. Phys. 45, 707 (1974).
26. R. A. Baragiola, E. V. Alonso and A. O. Flonio, "Electron Emission from Clean Metal Surfaces Induced by Low-Energy Light Ions," Phys. Rev. B19, 121 (1979).
27. R. F. Willis and D. K. Skinner, "Secondary Electron Emission Yield Behavior of Polymers," Solid State Commun. 13, 685 (1973).
28. P. K. Suh and M. G. Stauber, "Parameter Dependence of Equilibrium Charging Potentials," Spacecraft Charging Technology Conference 1978, AFGL-TR-79-0082, 711 (1979).
29. J. W. Robinson, "Stable Dielectric Charge Distributions from Field Enhancement of Secondary Emission," *ibid.* 734 (1979).

30. N. L. Sanders and G. T. Inouye, "Secondary Emission Effects on Spacecraft Charging: Energy Distribution Considerations," *ibid.* 747 (1979).
31. J. W. Haffner, "Secondary Electron Effects on Spacecraft Charging," *ibid.* 756 (1979).
32. S. M. L. Prokopenko and J. G. Laframboise, "High Voltage Differential Charging of Geostationary Spacecraft," *J. Geophys. Res.* 85, 4125 (1980).
33. K. G. Balmain and G. R. Dubois, "Surface Discharges on Teflon, Mylar and Kapton," *IEEE Trans. Nucl. Sci.* NS-26, 5146 (1979).
34. M. J. Treadaway, C. E. Mallon, T. M. Flanagan, R. Denson and E. P. Wenaas, "The Effects of High Energy Electrons on the Charging of Spacecraft Dielectrics," *ibid.* 5102 (1979).
35. T. M. Flanagan, R. Denson, C. E. Mallon, M. J. Treadaway and E. P. Wenaas, "Effect of Laboratory Simulation Parameters of Spacecraft Dielectric Discharges," *ibid.* 5141 (1979).
36. R. C. Keyser and J. M. Wilkenfeld, "Internal Responses of a Complex Satellite Model to Two Electron-Induced Discharge Simulation Techniques," *ibid.* 5121 (1979).
37. M. J. Treadaway, A. J. Woods, T. M. Flanagan, R. Grismore, R. Denson and E. P. Wenaas, "Experimental Verification of an ECEMP Spacecraft Discharge Coupling Model," AFWL SGEMP-J-5083 (25 July 1980).
38. A. J. Woods and T. N. Delmer, "The Arbitrary Body of Revolution Code (ABORC) for SGEMP/IEEMP," DNA-4348T (July 1976).
39. W. D. Swift, R. C. Keyser, B. H. Harlacher and M. A. Chipman, "Current Injection Testing for SGEMP Analysis Verification," AFWL-TR-76-317, May 1977.
40. B. Feuerbach and B. Fitton, "Experimental Investigation of Photoemission from Satellite Surface Materials," *J. Appl. Phys.* 43, 1563 (1972).
41. H. S. W. Massey, Negative Ions (Cambridge University Press, 3rd Edition, 1976).
42. C. Baum, E. L. Breen, J. C. Giles, J. O'Niell and G. D. Sower, "Sensors for Electromagnetic Pulse Measurements Both Inside and Away from Nuclear Source Regions," *IEEE Trans. on Ant. Prop.* AP-26, 22 (1978).
43. EG&G Standard EMP Instrumentation, Data Sheet 1109, December 1976.
44. E. P. Wenaas and A. J. Woods, "ECEMP Discharge Modeling," AFWL/CSC C⁴-J-4186, August 1979.
45. D. Hovey, "SABER 3-D SGEMP Code," IRT Report 0031-071, 31 July 1977.

46. B. Mulligan, R. C. Adamo, J. E. Nanevicz, B. L. Beers and T. N. Delmer, "Spacecraft Discharge Characterization--Test Setup, 'Quick Look' Experiments and Preliminary Model Development," Final Report - Phase I (Draft), December 1979.
47. R. Stettner, R. Marks and J. Dancz, "Physical Modeling of Spacecraft Discharge Processes and Associated Electron Blowoff," IEEE Trans. Nucl. Sci. NS-27, 1786 (1980).
48. I. Katz, M. J. Mandell, D. E. Parks and G. W. Schnuelle, "A Theory of Dielectric Surface Discharges," IEEE Trans. Nucl. Sci. NS-27, 1786 (1980).
49. G. T. Inouye, "Implications of Arcing Due to Spacecraft Charging on Spacecraft EMI Margins of Immunity," TRW Report 36186-6016-NE-00, March 1981.
50. D. F. Higgins, "A Description of the Basic Mechanisms of Electrical Excitation Techniques for Simulating SGEMP," MRC-R-261, February 1976 (also Appendix A in AFWL-TR-76-278).
51. B. C. Passenheim and V. A. J. van Lint, "Charging and Discharging of Teflon," Presented at the Spacecraft Charging Technology Conference, WAF Academy, October 1980.
52. Electromagnetic Compatibility Requirements for Space Systems, MIL-STD-1541 (USAF), 15 October 1973.
53. R. Leadon and J. M. Wilkenfeld, "Model for the Breakdown Processes in Dielectric Discharges," Proc. Spacecraft Charging Technology Conf. AFGL TR-79-0082, November 1978.
54. A. Holman, "Military Standard for Spacecraft Charging - Status Report," Presented at the Spacecraft Charging Technology Conference, USAF Academy, November 1980.
55. E. A. Burke, "Secondary Emission from Polymers," IEEE Trans. Nucl. Sci. NS-27, 1760 (1980).
56. J. M. Wilkenfeld, C. Mallon and J. Horne "Conduction and Charge Storage in Electron Irradiated Spacecraft Insulators," Final Report under RADC Contract F19628-77-C-0245, September 1980.
57. M. J. Treadaway, R. Denson, T. M. Flanagan and R. C. Leadon, "ECEMP Phase III Low Flux Tests," CSC/AFWL 200-80-235/2176, 31 July 1980.
58. P. F. Mizera, M. S. Leung and H. K. A. Kan, "Laboratory and Space Results from the SSPM Experiment," Aerospace TOR-0081(6505-02)-3.
59. H. T. Coffey, J. E. Nanevicz and R. C. Adamo, "Photoconductivity of High Voltage Space Insulating Materials," Final Report under NASA Contract NAS3-18912, October 1978.

60. K. G. Balmain and W. Hirt, "Dielectric Surface Discharges: Dependence on Incident Electron Flux," IEEE Trans. Nucl. Sci. NS-27, 1770 (1980).
61. B. L. Beers, H. C. Hwang, D. L. Lin and V. W. Pine, Electron Transport Model of Dielectric Charging, Spacecraft Charging Technology, 1978, NASA Conference Publication 2071, pp. 209-238 (1979).
62. R. C. Hazelton, R. J. Churchill and E. J. Yadlowsky, "Measurement of the Particle Emission from Discharge Sites in Teflon Irradiated by High Energy Electron Beams," IEEE Trans. Nucl. Sci. NS-26, 5146 (1979).
63. P. P. Budenstein, "Dielectric Breakdown in Solids," Report AD-A012177, U. S. Army Missile Command, December 1974.